Titre: Title:	Detailed EMT-Type Load Modeling for Power System Dynamic and Harmonic Studies
Auteur: Author:	Maryam Torabi Milani
Date:	2022
Type:	Mémoire ou thèse / Dissertation or Thesis
Référence: Citation:	Torabi Milani, M. (2022). Detailed EMT-Type Load Modeling for Power System Dynamic and Harmonic Studies [Ph.D. thesis, Polytechnique Montréal]. PolyPublie. https://publications.polymtl.ca/10266/

POLYTECHNIQUE MONTRÉAL

affiliée à l'Université de Montréal

Detailed EMT-type load modeling for power system dynamic and harmonic studies

MARYAM TORABI MILANI

Département de génie électrique

Thèse présentée en vue de l'obtention du diplôme de *Philosophiæ Doctor*

Génie électrique

Mars 2022

POLYTECHNIQUE MONTRÉAL

affiliée à l'Université de Montréal

Cette thèse intitulée:

Detailed EMT-type load modeling for power system dynamic and harmonic studies

présentée par **Maryam TORABI MILANI**

en vue de l'obtention du diplôme de *Philosophiæ Doctor*

a été dûment acceptée par le jury d'examen constitué de :

Houshang KARIMI, président
Jean MAHSEREDJIAN, membre et directeur de recherche
Bahram KHODABAKHCHIAN, membre et codirecteur de recherche
Keyhan SHESHYEKANI, membre et codirecteur de recherche
Antoine LESAGE-LANDRY, membre
Parag MITRA, membre externe

DEDICATION

To my husband, parents, and sister

ACKNOWLEDGEMENTS

First, I would like to express my sincere gratitude to my PhD supervisor Prof. Jean Mahseredjian for the opportunity to pursue this PhD project, his continuous support, patience, and encouragement during my research.

I would like to express my enormous gratitude to my co-supervisor, Mr. Bahram Khodabakhchian whose immense knowledge and experience, and invaluable guidance have made this an inspiring experience for me. It was a great privilege and honor to work under his supervision.

My appreciation is also extended to my co-supervisor Prof. Keyhan Sheshyekani for the valuable advice he offered me.

I would like to thank the distribution and transmission divisions of Hydro-Quebec, Mr. Francois Noiseux for providing field recordings, Mr. Bruno Fazio for providing access to CYMDIST software, Mr. Dave Beaudoin and Mr. Pascal Prud'homme for their technical support.

I would also like to thank my friends and colleagues at Polytechnique Montreal, whose valuable discussions and support helped me throughout my research.

Finally, I wish to express my deepest gratitude to my husband for his endless love, patience, and support during my studies. Also, I am extremely grateful to my parents and my sister for all the love, encouragement and support.

RÉSUMÉ

Le fonctionnement en régime permanent et dynamique des systèmes électriques est fortement influencé par les caractéristiques des charges alimentées. Par conséquent, une analyse précise des systèmes électriques nécessite des modèles de charge appropriés. Comme la majorité des modèles de charge existants ne permettent pas une représentation complète ou précise des charges réelles agrégées, il est essentiel de développer de nouveaux modèles de charge afin de capter plus précisément le comportement de la charge.

Dans cette thèse, un nouveau modèle de charge détaillé basé sur des composants de type EMT (transitoire électromagnétique) est développé dans le logiciel Electromagnetic Transient Program (EMTP®). Des modèles individuels de type EMT de composants de diverses catégories de charge sont d'abord développés et ensuite agrégés à un niveau supérieur pour former un modèle de charge détaillé agrégé. Le modèle proposé permet de capter la diversité des dispositifs des charges réelles agrégées et est également capable de prendre en compte les non-linéarités (l'électronique de puissance), les charges monophasées et les conditions déséquilibrées. Il offre une plus grande précision et peut fournir une description plus réaliste du comportement de la charge par rapport aux modèles existants.

Le modèle développé est utilisé pour simuler le comportement de la charge lors d'événements de baisse de tension dans différents secteurs de charge et est validé par rapport à des mesures. La validation du modèle dans des cas réels est une étape importante du développement du modèle de charge qui est nécessaire pour garantir la capacité du modèle proposé à reproduire le comportement dynamique des charges pendant et après les perturbations.

La modélisation détaillée de la charge n'est généralement pas l'approche préférée, principalement en raison des exigences de données excessives, des efforts et du temps de calcul. Cependant, l'importance du modèle détaillé pour capter le comportement de la charge dans les simulations dynamiques est étudiée et son avantage par rapport aux modèles traditionnels est illustré.

Pour explorer un autre aspect de la modélisation de charge, la réponse en fréquence de la charge est étudiée à travers la simulation d'un réseau de distribution souterrain existant. L'importance du modèle détaillé pour capter le comportement de la charge dans les simulations harmoniques est étudiée et les erreurs causées par les modèles conventionnels sont analysées. Dans le prolongement

de cette partie, de nouvelles directives concernant la modélisation des réseaux de distribution souterrains pour les simulations harmoniques des réseaux électriques, sont fournies.

ABSTRACT

Steady-state and dynamic performance of power systems are strongly influenced by the characteristics of the supplied loads. Therefore, correct analysis of power systems requires appropriate load models. As the majority of existing load models do not allow for a full or precise representation of the real aggregated loads, it is essential to develop accurate load models in order to capture load behavior more accurately.

In this thesis a new detailed EMT-type (electromagnetic transient) component-based load model is developed in the time-domain simulation tool, EMTP® (Electromagnetic Transients Program). Individual EMT-type models of components from various load categories are first developed and next aggregated to form an aggregated detailed load model. The proposed model captures the diversity in end-use devices of real aggregated loads and is also capable of accounting for nonlinearities (i.e., power electronics), single-phase loads and unbalanced conditions (e.g., asymmetrical faults). It offers higher accuracy and can provide a more realistic description of the load behaviour compared to the existing models.

The developed model is used to simulate load behavior in voltage sag events in different load sectors and is validated against field data. Validation of the model in real cases is an important stage of load model development which is required to ensure the capability of the proposed model to reproduce the dynamic behavior of loads during and following disturbances.

Detailed load modeling is not usually the preferred approach mainly due to excessive data requirements, modeling efforts and computational burden. However, the importance of the detailed model for capturing load behaviour in dynamic simulations is investigated and its advantage over traditional models is highlighted.

To explore a different aspect of load modeling, the frequency response of the load is studied through the simulation of an existing underground distribution network. The importance of the detailed model for capturing load behaviour in harmonic simulations is investigated and errors caused by conventional models are introduced. As an extension to this part, some new guidelines regarding modeling underground distribution systems for harmonic simulations of power systems is provided.

TABLE OF CONTENTS

DEDICATION III

ACKNOWLEDGEMENTS IV

RÉSUMÉ V

ABSTRACT VII

TABLE OF CONTENTS VIII

LIST OF TABLES XII

LIST OF FIGURES XIII

LIST OF SYMBOLS AND ABBREVIATIONS XVIII

CHAPTER 1 INTRODUCTION 1

1.1 Motivation 1

1.2 Thesis objectives 3

1.3 Contributions 3

1.4 Methodology 6

1.5 Thesis structure 8

CHAPTER 2 LOAD MODELING REVIEW 10

2.1 Static load models 10

2.2 Dynamic load models 12

2.2.1 Exponential dynamic load model 13

2.2.2 Dynamic model of induction motor 14

2.3 Composite load models 15

2.4 Harmonic load models 16

2.4.1 Linear loads 16

2.4.2 Nonlinear loads 20

2.5 Methodologies for aggregated load model development 22
2.5.1 Measurement-based approach 22
2.5.2 Component-based approach 23
2.6 Summary 24
CHAPTER 3 LOAD COMPONENTS 25
3.1 Resistive load category 25
3.2 Switch-mode power supply 25
3.2.1 SMPS topology 26
3.2.2 SMPS circuit-based model 27
3.2.3 EMTP model of SMPS 28
3.3 Lighting sources 31
3.3.1 Incandescent lamps 33
3.3.2 Compact fluorescent lamps 35
3.3.3 Light emitting diodes 39
3.4 Induction motor 43
3.4.1 Single-phase induction motors 43
3.4.2 Three-phase induction motors 46
3.5 Variable frequency drives of three-phase induction motors 48
3.5.1 VFD topology 48
3.5.2 Scalar-based control 49
3.5.3 Vector control 50
3.5.4 EMTP model of VFD 55
3.6 Summary 58
CHAPTER 4 AGGREGATED DETAILED LOAD MODEL 59

4.1 Component-based aggregation procedure 59
4.2 Implementation of the new aggregated load model 61
4.2.1 Subcircuit contents 62
4.2.2 Subcircuit masking 64
4.3 Static characteristics 74
4.3.1 Forming the DM of the residential-commercial load 75
4.3.2 Voltage ramp tests 76
4.4 Importance of the detailed load model 79
4.5 Dynamic characteristics 84
4.5.1 Event at hospital-A 85
4.5.2 Event at Hospital-B 97
4.5.3 Event at a commercial center 102
4.5.4 Event at a residential area 107
4.6 Summary 119
CHAPTER 5 LOAD MODELING IN HARMONIC STUDIES 121
5.1 Description of the test network 121
5.2 EMTP model of the test network 123
5.3 Frequency response 126
5.3.1 Frequency scan from 12.47 kV bus 127
5.3.2 Frequency Scan from 120 kV bus 129
5.4 Effect of cables on the frequency response 131
5.5 Summary 135
CHAPTER 6 CONCLUSION 136
6.1 Summary of thesis 136

6.2 List of publications 139

6.3 Future works 140

REFERENCES 142

LIST OF TABLES

Table 3.1 Existing load models for SMPS load category 26

Table 3.2 Existing load models of lighting load category 32

Table 3.3 Existing fluorescent tube models 33

Table 3.4 Single-phase IM motor parameters 45

Table 3.5 Three-phase IM motor parameters 48

Table 3.6 Motor parameter related to comparison of VFD models in EMTP and Simulink 56

Table 4.1 Classification of load components in different load sectors 62

Table 4.2 Initial parameter-values of the DM subcircuit mask 66

Table 4.3 Residential load composition 76

Table 4.4 Commercial load composition 76

Table 4.5 Load composition of Hospital-A 87

Table 4.6 Load composition of Hospital-B 99

Table 4.7 Load composition of the commercial center 104

Table 4.8 Load composition of the residential load, event 1 110

Table 4.9 Load composition of the residential load, event 2 116

Table 4.10 Small industrial motor parameters 117

LIST OF FIGURES

Figure 2.1 Typical response of the exponential dynamic load model adopted from [25].....14

Figure 2.2 WECC composite load model adopted from [32] 15

Figure 2.3 Harmonic load model-3 17

Figure 2.4 Harmonic load model-9 19

Figure 2.5 Harmonic load model-10 20

Figure 2.6 CCS model of nonlinear loads 21

Figure 2.7 Norton equivalent of nonlinear loads.....21

Figure 2.8 Measurement-based approach.....23

Figure 2.9 Component-based approach.....24

Figure 3.1 General block diagram of SMPS circuit topology adopted from [54].....27

Figure 3.2 Equivalent circuit of SMPS model 27

Figure 3.3 EMTP equivalent circuit of SMPS model 29

Figure 3.4 Structure of the ramping voltage source 30

Figure 3.5 Table function employed in the structure of the ramping voltage source 30

Figure 3.6 P-V and Q-V characteristics measured at the terminals of SMPS equivalent circuit..31

Figure 3.7 EMTP equivalent circuit of incandescent lamp model.....34

Figure 3.8 General block diagram of CFL circuit topology [53].....35

Figure 3.9 Equivalent circuit of CFL model 36

Figure 3.10 EMTP equivalent circuit of CFL model 38

Figure 3.11 P-V and Q-V characteristics measured at the terminals of CFL equivalent circuit...39

Figure 3.12 Piecewise linear model of LED 40

Figure 3.13 Equivalent circuit of LED model.....41

Figure 3.14 EMTP equivalent circuit of LED model.....42

Figure 3.15 P-V and Q-V characteristics measured at the terminals of LED equivalent circuit ..43

Figure 3.16 Equivalent circuit of double-phase induction machine.....44

Figure 3.17 Equivalent circuit of three-phase induction machine 46

Figure 3.18 IM torque-speed characteristics modeled with single-cage and double cage rotor structure.....47

Figure 3.19 VFD circuit topology.....49

Figure 3.20 Types of VFD control.....49

Figure 3.21 Block diagram of IFOC control.....52

Figure 3.22 EMTP equivalent circuit of VFD model.....56

Figure 3.23 Stator currents of developed VFD model in EMTP 57

Figure 3.24 Stator currents of Simulink VFD model.....57

Figure 3.25 Rotor speed comparison between EMTP and Simulink models of VFD 57

Figure 3.26 Rotor speed comparison between EMTP and Simulink models for VFD, reference speed change from 120 rad/s to 160 rad/s at t=2s 58

Figure 4.1 Implementation of the detailed model (DM) in EMTP, subcircuit mask and contents 63

Figure 4.2 Transformer model Electra No.167 [18].....64

Figure 4.3 System set-up for comparison of the DM and static load model.....75

Figure 4.4 Static characteristics of the DM: (a) winter, (b) summer 78

Figure 4.5 P-V characteristics of winter and summer load, modeled by DM.....78

Figure 4.6 Q-V characteristics of winter and summer load, modeled by DM 79

Figure 4.7 Subcircuit mask for voltage swing block in Figure 4.3 81

Figure 4.8 Subcircuit contents for voltage swing block in Figure 4.3 81

Figure 4.9 Voltage swing dynamic characteristics: positive sequence voltage, active and reactive power.....82

Figure 4.10 Post-fault dynamic characteristics: positive sequence voltage, active and reactive power 83

Figure 4.11 Three-phase voltages, simulation (red dotted) vs measurement (blue solid), Hospital-A case study 86

Figure 4.12 Simulated vs. recorded harmonic currents, Hospital-A case study 88

Figure 4.13 Current waveform of compressor motor, Hospital-A case study 88

Figure 4.14 Three-phase currents, simulation (dotted) vs measurement (solid), Hospital-A case study 90

Figure 4.15 Simulated active and reactive powers vs. measurement, Hospital-A case study 91

Figure 4.16 Simulated active and reactive powers vs. measurement, effect of percentage contribution of three-phase IM, Hospital-A case study 93

Figure 4.17 Simulated active and reactive powers vs. measurement, effect of percentage contribution of lighting and SMPS, Hospital-A case study 94

Figure 4.18 Three-phase IM electric power during voltage sag, Hospital-A case study 95

Figure 4.19 Simulated active and reactive powers vs. measurement, effect of percentage contribution of different types of three-phase IM, Hospital-A case study 96

Figure 4.20 Simulated active and reactive powers vs. measurement, effect of motor inertia constant, Hospital-A case study 97

Figure 4.21 Three-phase voltages, simulation (red dotted) vs. measurement (blue solid), Hospital-B case study 98

Figure 4.22 Simulated vs. recorded harmonic currents, Hospital-B case study 100

Figure 4.23 Three-phase currents, simulation (dotted) vs. measurement (solid), Hospital-B case study 101

Figure 4.24 Simulated active and reactive powers vs. measurement, Hospital-B case study 102

Figure 4.25 Three-phase voltages, simulation (dotted) vs. measurement (solid), commercial center case study 103

Figure 4.26 Simulated vs. recorded harmonic currents, the commercial center case study.....105

Figure 4.27 Three-phase currents, simulation (dotted) vs. measurement (solid), commercial center case study 106

Figure 4.28 Simulated active and reactive powers vs. measurement, commercial center case study 107

Figure 4.29 Single-line diagram of the residential case study 108

Figure 4.30 Three-phase voltages; simulation (dotted) vs. measurement (solid), residential load case study, event 1.....109

Figure 4.31 Comparison of simulated active and reactive powers, single-phase IM adjusted to QT and CT mechanical load types, residential load case study, event 1.....112

Figure 4.32 Single-phase IM slip comparison, QT and CT mechanical load types, residential load case study, event 1.....112

Figure 4.33 Three-phase currents; simulation (dotted) vs. measurement (solid), residential load case study, event 1.....113

Figure 4.34 Simulated active and reactive powers (red) vs. measurement (blue), residential load case study, event 1.....114

Figure 4.35 Three-phase voltages; simulation (dotted) vs. measurement (solid), residential load case study, event 2.....115

Figure 4.36 Simulated active and reactive powers (red) vs. measurement (blue), residential load case study, event 2.....117

Figure 4.37 Three-phase currents, simulation (dotted) vs. measurement (solid), residential load case study, event 2.....118

Figure 5.1 Schematic of the test network, one feeder of Dorchester distribution network.....122

Figure 5.2 Low voltage part of the test network of Figure 5.1, modeled in detail.....122

Figure 5.3 Test network model in CYMDIST 123

Figure 5.4 Cable parameters for Wideband model 124

Figure 5.5 Cross section of a single core cable for Wideband model 125

Figure 5.6 Cable parameters for PI model 125

Figure 5.7 Comparison of magnitude and phase angle of the harmonic impedance of Wideband and PI model 126

Figure 5.8 Magnitude and phase angle of harmonic impedance seen from the 12.47 kV bus 128

Figure 5.9 Magnitude and phase angle of harmonic impedance seen from the 12.47 kV bus, load model comparison 129

Figure 5.10 Magnitude and phase angle of harmonic impedance seen from the 120 kV bus 130

Figure 5.11 Magnitude and phase angle of harmonic impedance seen from the 120 kV bus, load model comparison 131

Figure 5.12 Effect of cables on magnitude and phase angle of harmonic impedance seen from the 12.47 kV bus, no compensation 132

Figure 5.13 Effect of cables on magnitude and phase angle of harmonic impedance seen from the 12.47 kV bus, 30% compensation 133

Figure 5.14 Effect of cables on magnitude and phase angle of harmonic impedance seen from the 120 kV bus 134

LIST OF SYMBOLS AND ABBREVIATIONS

AC	Air conditioner
CCS	Constant current source
CFL	Compact fluorescent lamp
CP	Constant mechanical power
CT	Constant torque
DC	Direct current
DFR	Digital fault recorder
DM	Detailed model
DTC	Direct torque control
EDF	Électricité de France
EMI	Electromagnetic interface
EMT	Electromagnetic transient
EMTP	Electromagnetic transient programs
EPRI	Electric Power Research Institute

FOC	Field-oriented control
GIL	General incandescent lamp
HVDC	High voltage direct current
IFOC	Indirect field-oriented control
IGBT	Insulated-gate bipolar transistor
IM	Induction motor
LED	Light emitting diode
LFL	Linear fluorescent lamp
LT	Linear torque
LV	Low voltage
MV	Medium voltage
NE	Northeast
NTC	Negative temperature coefficient
OLTC	Onload tap changer
P	Active power

PC	Personal computer
PFC	Power factor correction
PLC	Programmable logic controller
PQM	Power quality meter
pu	Per-unit
PV	Photovoltaic
PWM	Pulse-width modulation
Q	Reactive power
QT	Quadratic torque
SMPS	Switch-model power supply
TV	Television
VFD	Variable frequency drive
VSI	Voltage source inverter
VT	Variable torque
WB	Wide band

WECC	Western electricity coordinating council
WSCC	Western systems coordinating council
ZIP	Polynomial load model

CHAPTER 1 INTRODUCTION

1.1 Motivation

Load modelling is one of the most important areas in power system modelling. Steady-state and dynamic performance of power systems are strongly influenced by the characteristics of the supplied loads. Accordingly, correct analysis of power systems requires appropriate load models. Different load models can affect simulation results and, therefore, corresponding design decisions. Although the importance of correct load representation is well recognized, certain assumptions are often made about load models. This is due to the lack of available load modelling data or to avoid longer simulation times. Such assumptions may lead to model inadequacies. Examples of load modelling inadequacies in power system analysis are briefly discussed below. In the following text, static load model refers to a model in which active and reactive power demands of load are represented as algebraic functions of voltage and frequency, independent of time. Exponential load model is one type of static model in which active and reactive powers of the load are defined as exponential equations with respect to voltage magnitude and frequency. Constant impedance load model is a variant of exponential model in which active and reactive powers of the load vary proportionally to the square of the voltage magnitude. In the constant current load model, which is another variant of exponential model, active and reactive powers of the load vary linearly with the voltage magnitude. Finally, for constant power load model, the active and reactive powers of the load are constant, irrespective of the changes in voltage magnitude.

A power failure with loss of about 30 MW occurred in 1996 in the Western Systems Coordinating Council (WSCC) [1]. The system lost its stability with increased oscillations. In the simulation attempts carried out after the event to analyze it, loads were represented primarily by static models (constant current real power and constant impedance reactive power load model). The simulated system showed more damping than the actual one. By changing the load model to a combination of static and induction motor models, the simulated and measured responses showed close agreement. Therefore, the results indicated that changes to the load model can significantly change the system response.

In another study carried out on the Taiwan Power System [2], the effect of different load models on the simulation results was assessed during the investigation of an unstable low frequency

oscillation in the system. When the static load model (exponential model) was used, the undamped oscillations in the system could not be reproduced. When composite load models, i.e., combination of static and dynamic models were used, the results were in close agreement with field measurements.

To study the dynamics following three-phase short circuit disturbances in the NE (Northeast) power grid in China [3], three different load models were applied. A static model (constant power), a composite load model including an induction motor in parallel with a static load model and a third load model built upon measured data. Different simulation results were observed and compared to measurements. The composite model and the measurement-based model reflected system dynamics much better than the static load model.

In summary, different load models may lead to different simulation results. Since the computer simulation of the power system is a fundamental tool to understand system behavior and provide guidelines on its planning and control, developing appropriate load models is essential for ensuring secure operation of power system.

In addition to the examples discussed above, the interest in load modelling also arises from the recent technological changes. The types of loads commonly found in the distribution system have changed significantly in the last few decades. Different types of modern nonlinear power electronic loads are now responsible for a significant part of the total demand. Examples are the increasing penetration of energy saving light sources and adjustable speed drives. This highlights the fact that previously developed models are not sufficient to represent modern loads. Therefore, there is a need to develop models which are able to satisfy the requirements for analysis of modern power systems. Representative and appropriate load models are thus becoming increasingly important.

From another aspect, loads have a considerable influence on the harmonic characteristics of the network. Harmonics have been part of the electric power network since the introduction of nonlinear devices that absorb currents with a non-sinusoidal waveform. The disturbing effects of harmonics, as discussed in literature (e.g., [4],[5],[6]), include additional losses and heating in the system, faulty operation of control equipment and measuring devices. Therefore, standards exist to control and limit the amount of harmonic distortion present in the system. To keep the harmonic distortion levels within limits, studies and assessments are performed at different stages of network.

The need for such harmonic assessments is becoming even more pronounced as the connection of nonlinear devices increases, examples are integration of renewable energy sources and connection of new HVDC converters. In those studies, proper and adequate modelling of the power system is required, as it impacts the subsequent design of harmonic filters with associated costs and risks. The need for up-to-date information on the topic of harmonic load modelling is constantly increasing due to the increasing number of HVDC interconnectors, wind power plants, PV-based technologies and distributed generation.

1.2 Thesis objectives

The main purpose of this thesis is to develop a new load model to reproduce the real aggregated load behavior both in dynamic and harmonic simulations. A detailed aggregated EMT-type component-based load model is developed to provide a more accurate representation of the reality of aggregated loads compared to existing load models.

This thesis has two more objectives by making use of the developed detailed model:

- Firstly, to investigate the importance of the detailed model for capturing real load behaviour in dynamic simulations. The developed model is compared against a conventional model through different dynamic simulations.
- Secondly, to investigate the importance of the detailed model for capturing real load behaviour in harmonic simulations and the adequacy of existing models. This is achieved by modeling an existing underground distribution system in detail and studying the frequency response of the load using the detailed and a conventional load model. In the context of harmonic simulations, the ultimate aim of this thesis is to contribute to guidelines regarding modeling underground distribution systems for harmonic studies in terms of the impact of cables and different values of reactive power compensations.

1.3 Contributions

The main contributions of this thesis are summarized here. Contributions are presented along with a literature review to clearly position this thesis with respect to previous work.

- A new detailed EMT-type component-based load model for dynamic simulations

Although the importance of load modeling is generally recognized as discussed in Section 1.1, loads are often represented by typical static models even for dynamic simulations of power systems [7]. Some works, however, have used a simple composite load model, which is a combination of a static model and an induction motor model, in order to better capture the dynamics [3], [8]. Nevertheless, to approach the load behavior more precisely, more detailed composite models are essential as they provide a realistic representation of aggregated loads. Limited efforts have been devoted to developing such load models [9], [10]. The latest development in this field belongs to the composite load model (CMLD) in PSSE [11]. This model is an aggregation of three-phase and single-phase induction motors, power electronics and static loads. Although this model acknowledges variety in load components, it is not sufficiently accurate in terms of modeling power electronics and single-phase motors; power electronics are grouped as constant power loads which is a simplistic assumption. The single-phase motor is represented by a "performance model" using algebraic equations to represent the motor power consumption in terms of terminal voltage, which is known to be an approximation. This model is a positive sequence model with an assumption that all three phases are balanced. In reality, the loads are connected to individual phases, and load responses are different between the phases during unbalanced disturbances. In positive sequence models not only the dynamic model of single-phase motors can not be accurately incorporated, but also unbalanced faults can not be correctly represented.

To fill in the existing gaps and overcome the existing limitations, this thesis contributes a new EMT-type (electromagnetic transient) component-based load model. In this model, individual EMT-type models of load components from various load categories are first developed and next aggregated to a top level to form an aggregated detailed load model. This new model has two main advantages over the existing ones.

First, unlike existing models, the proposed model is an EMT-type model. An EMT-type model is based on the representation of the actual electrical circuit equivalent of the load components. It is implemented in the time-domain simulation tool EMTP® (Electromagnetic Transients Program) where network equation formulation is accomplished using nodal analysis, and numerical integration technique is applied to solve them. Therefore, this model is capable of accounting for nonlinearities (i.e., power electronics), single-phase loads (e.g., single-phase motors) and unbalanced conditions (i.e., asymmetrical faults). Therefore, it offers higher accuracy and can

provide a more realistic description of load behavior compared to the existing models. It should also be noted that, most of the existing load model forms are able to represent load characteristics for only one type of power system analysis (e.g. steady-state or harmonic studies). The proposed model on the other hand, will allow the electrical characteristics of the modelled load to be converted into any required load model form. This is because the circuit-based EMT-type load model offers the possibility of reproducing the instantaneous input current and active and reactive power waveforms. By analyzing the waveforms, any required information on load characteristic can be extracted.

Second, in the proposed detailed component-based model, individual components are selected from wide range of load categories e.g., lighting sources, power electronics, motors, etc. Therefore, the proposed model provides a more realistic description of load behavior by capturing the diversity in composition and characteristics of real end-use applications.

- Application of field data

Another important contribution of this thesis is the fact that the developed model is validated against measurement data coming from the field. This issue is not sufficiently addressed in the identified literature due to general lack of suitable measurement data. This is because a large number of measurements must be performed on specific points of the power system where the network and load configurations are relatively well known. This thesis benefits from several voltage sag events recorded by Hydro-Quebec at representative feeders on the network. The developed model is used to simulate load behavior in those events and its efficacy in reproducing the real dynamic behavior of loads during and following the disturbances is validated against the provided field data.

Available field data not only is used for model validation, but also is exploited to identify load compositions of different load sectors more accurately and also find some additional features of load characteristics (e.g., connection or reconnection pattern of motor loads during and following voltage sags). This is one of the practical aspects of load modeling which is not widely reported in existing literature due to limited availability of measurement data and recorded disturbances that are suitable for the derivation of such information. The presented information is added to the

developed model and allows for a more comprehensive and realistic representation and offers some insight into general considerations when modeling power system loads.

Since the proposed load model, the identified load compositions in different load sectors, and the characteristics of different load components are obtained and validated through real case studies, they can be referred to in studies involving similar types of loads.

- Importance of the detailed load model in harmonic simulations and new guidelines for modeling underground distribution networks

Recent work in load modeling area is mainly related to representing nonlinear loads in the frequency domain [12], [13], [14]. However, the frequency domain methods have important limitations when considering nonlinear devices and their control functions. The proposed EMT-type model provides detailed modelling of power electronics and therefore is a powerful means to model the nonlinear behaviour of those devices and their controllers. Furthermore, the current practice in most harmonic simulations of power systems is linear load models [15], [16], [17], [18], [19]. Another contribution of this work is to examine the adequacy of such models to realistically capture the behaviour of loads in harmonic simulations. The developed detailed model identifies the conditions in which extra efforts are justified for detailed modeling of loads in harmonic simulations. Generally, availability of practical information and guidance for modeling power systems in harmonic simulations are very limited. This thesis contributes to guidelines regarding harmonic modeling of underground distribution systems through simulation of a real test case.

1.4 Methodology

To provide a flexible load model which is applicable to a wide range of power system analysis, a flexible modelling approach is selected. As introduced in the previous sections, it involves EMT-type models within a component-based aggregation framework. EMT-type models are based on the representation of the actual electrical circuit equivalent of the load. Therefore, the electrical elements within the circuits of load components are identified and corresponding models based on the circuit topology are developed. The individual component models are subsequently aggregated in a component-based scheme to form the aggregated load.

Developing the aggregated load model begins by modeling its individual load components. The types of load components that can be found in different end-use applications are divided into the five general load categories according to similarities in application and comparable electrical characteristics. In this thesis, load categories are resistive loads, switch-mode power supplies, lighting sources, single-phase and three-phase directly connected induction motors and three-phase drive-controlled induction motors. In this thesis, some load component models are adopted from existing literature, and some are new models which are developed based on the circuit topology and principles of operation of load components. Load component models are implemented in the time-domain simulation tool, EMTP® (Electromagnetic Transients Program) [20]. EMTP® has been widely accepted and used as a standard and powerful simulation tool for power system studies. The models of individual components are established in per-unit form that are able to represent the characteristics of an aggregated same type of load and further aggregation with other components to form the desired aggregate load. The full electric circuits of loads are normally very complex, and often contain large numbers of elements. They require long simulation times and also are not straightforward for load aggregation. Therefore, equivalent circuits of some full models are used.

After the EMT component model of each abovementioned load category is developed, they are used in a component-based procedure to form a detailed aggregate mixed-type load of different load sectors, namely residential, commercial, and small industrial. Each load sector is characterized by categories that account for the majority of the power consumed by end users within that sector.

The developed model is used to simulate load behavior in several voltage sag events of different load sectors and its efficacy in reproducing the real dynamic behavior of loads during and following the disturbances is validated against the field data provided by Hydro-Quebec.

Available field data not only is used for model validation, but also is exploited to identify some additional features on load behavior e.g., connection or reconnection pattern of motor loads during and following voltage sags. Obtaining such information allows for a more comprehensive representation of the load and offers some insight into general considerations when modeling power system loads.

The performance of the developed model is compared against a conventional model and the importance of the detailed model to capture real load behaviour in dynamic simulations is highlighted.

Finally in a different step of load modeling, frequency response of the load is studied by making use of the developed model while simulating an existing underground distribution network. The frequency scan is performed in time-domain due to the presence of nonlinearities (power electronics, controls…). The scanning method is available in EMTP® and uses a perturbation approach by injecting a current for each frequency on the bus of interest and extracting the corresponding harmonic voltage for calculating harmonic impedance [21]. The importance of the detailed model to capture real load behaviour in harmonic simulations and the inadequacy of the conventional model is investigated. By identifying the effect of the presence of cables on the harmonic impedance, some new guidelines for modeling underground distribution systems in harmonic studies is provided. As corresponding measurements are not currently available, validation at this level is not possible within the timeframe of this thesis. However, validation of the proposed model itself ensures a good level of accuracy and thus provides confidence in results of the harmonic simulations.

1.5 Thesis structure

This thesis is divided into six chapters:

Chapter 2

This is an introductory chapter, reviewing previous work in the area of load modelling. It provides an overview of the load models and load modelling approaches commonly used today. This includes static, dynamic, and composite models, as well as harmonic load models. Measurement-based and component-based modeling approaches are also described.

Chapter 3

This chapter presents modeling of individual load components grouped into five main load categories; resistive loads, switch-mode power supplies, lighting sources, single-phase and three-phase directly connected induction motors and drive-controlled three-phase induction motors.

Chapter 4

This chapter uses the developed individual models to form an aggregated load model in a component-based aggregation procedure. The importance of the detailed model to capture the dynamic response of the load is presented. The majority of this chapter is focused on the application of the developed model in different load sectors. The model is used in a range of case studies to simulate dynamic load behavior in voltage variation events. Its performance is validated against field data recorded during those events.

Chapter 5

This chapter contains information on the frequency response of load. Simulations are performed on the detailed model of one feeder of an existing underground distribution network to investigate the effect of detailed load modeling on the harmonic impedance and to introduce errors caused by load model simplifications. Moreover, investigation on the impact of cables and different values of reactive power compensation on the harmonic impedance provides some new guidelines for modeling underground distribution systems in harmonic studies.

Chapter 6

This chapter reviews the main findings of the research and presents the conclusions from this work in the load modelling research area. Suggestions for future work are also discussed.

CHAPTER 2 LOAD MODELING REVIEW

This chapter is an overview of the load models and modeling approaches commonly used. Existing load models can be divided into two basic groups, static and dynamic. When static and dynamic models are used together, this is known as a composite load model. Two existing most widely used methodologies for load model development are the measurement-based and the component-based approaches. Harmonic load models are also introduced as they are of particular interest to the research presented in this thesis.

2.1 Static load models

Static models represent the active and reactive power demand of the load as an algebraic function of voltage and frequency, independent of time. These models are appropriate for representing loads which respond instantaneously to a change in voltage and/or frequency. Several commonly used static load models are presented in this section [22]. In the following text, *V*, *f*, *P* and *Q* are the actual voltage magnitude, frequency, active and reactive powers of the load at the connecting bus, respectively. V_0, f_0, P_0 and Q_0, denote nominal system voltage, frequency, active and reactive powers of the load.

Exponential load model: the active and reactive power demand of the load are defined as exponential equations with respect to voltage magnitude and frequency:

$$P = P_0 \left(\frac{V}{V_0}\right)^{n_p} \left(\frac{f}{f_0}\right)^{k_p} \tag{2.1}$$

$$Q = Q_0 \left(\frac{V}{V_0}\right)^{n_q} \left(\frac{f}{f_0}\right)^{k_q} \tag{2.2}$$

where exponents n_p, n_q and k_p, k_q define the relationship between active and reactive power demands and supply voltage and frequency. Constant power, constant current and constant impedance load characteristics can be represented by setting the exponents to 0, 1, and 2, respectively. The exponents can be set to other values to represent a desired load characteristic. Load dependency on frequency is often neglected as frequency variations during the steady-state

operating conditions are usually very small. So, the frequency dependency terms in the two previous equations can be replaced by Taylor series expansion. The alternate form of the model is:

$$P = P_0 \left(\frac{V}{V_0}\right)^{n_p} \left[1 + k_p(f - f_0)\right] \tag{2.3}$$

$$Q = Q_0 \left(\frac{V}{V_0}\right)^{n_q} \left[1 + k_q(f - f_0)\right] \tag{2.4}$$

It has been shown in [23] that the parameters n_p and n_q represent active and reactive power sensitivities to voltage. It means for a small change in voltage about the operating point, n_p and n_q correspond to the partial derivatives of active and reactive power with respect to voltage.

Constant impedance load model: active and reactive powers of the load vary proportionally to the square of the voltage magnitude.

Constant current load model: active and reactive powers of the load vary linearly to the voltage magnitude.

Constant power load model: active and reactive powers of the load are constant, irrespective of the changes in voltage magnitude.

Polynomial load model: this model which is also referred to as the ZIP model, consists of constant impedance, constant current and constant power terms:

$$P = P_0 \left[Z_p \left(\frac{V}{V_0}\right)^2 + I_p \left(\frac{V}{V_0}\right) + P_p\right] \tag{2.5}$$

$$Q = Q_0 \left[Z_q \left(\frac{V}{V_0}\right)^2 + I_q \left(\frac{V}{V_0}\right) + P_q\right] \tag{2.6}$$

where parameters Z_p and Z_q represent the percentage contribution of constant impedance load, I_p and I_q are the percentage contribution of constant current load, P_p and P_q are percentage contribution of constant power load. The polynomial load model with frequency dependency taken into account is given by [24]:

$$P = P_0 \left[Z_p \left(\frac{V}{V_0} \right)^2 + I_p \left(\frac{V}{V_0} \right) + P_p \right] \left[1 + k_p (f - f_0) \right] \quad (2.7)$$

$$Q = Q_0 \left[Z_q \left(\frac{V}{V_0} \right)^2 + I_q \left(\frac{V}{V_0} \right) + P_q \right] \left[1 + k_q (f - f_0) \right] \quad (2.8)$$

Comprehensive static load model: the comprehensive static load model offers the flexibility of having several forms of load representation. It consists of one polynomial and two exponential models, each having different parameters [7], [24]:

$$P_{zip} = Z_p \left(\frac{V}{V_0} \right)^2 + I_p \left(\frac{V}{V_0} \right) + P_p \quad (2.9)$$

$$P_{ex1} = P_0 \left(\frac{V}{V_0} \right)^{a_1} \left[1 + k_{p1} (f - f_0) \right] \quad (2.10)$$

$$P_{ex2} = P_0 \left(\frac{V}{V_0} \right)^{a_2} \left[1 + k_{p2} (f - f_0) \right] \quad (2.11)$$

$$P = P_{zip} + P_{ex1} + P_{ex2} \quad (2.12)$$

Reactive power is modelled using a similar structure.

All the presented static models may lead to computational problems at low voltages. When voltage drops below a certain voltage threshold, in most commercial software tools, the constant power and constant current load components in ZIP are switched to a constant impedance representation to ensure numerical stability of the network solution in the simulation.

2.2 Dynamic load models

Dynamic load models represent the active and reactive power of the load as a function of voltage, frequency, and time. They are usually described in differential equation form relating active and reactive powers with voltage and frequency. These models are used for representing loads with time-dependent responses to a change in voltage and/or frequency (e.g., induction motors). The most common forms of dynamic load models are introduced in this section.

2.2.1 Exponential dynamic load model

The exponential dynamic load model represents the observed response of the load to voltage variations. Laboratory tests and measurements performed on real system buses have shown that the typical load response subjected to a step change in voltage has the form shown in Figure 2.1 [25]. This graph is shown for the active power, the response of reactive power can be represented using the same form. As the result of a step change in voltage, a step change in power demand happens, followed by a recovery to a new steady-state value. It has been shown in [26] that by assuming an exponential mode of recovery, as well as exponential functions for $P_s(V)$ and $P_t(V)$ (steady-state and transient load responses), the active power response can be modelled as a first order differential equation:

$$T_p \frac{dP_r}{dt} + P_r = P_s(V) - P_t(V) = P_0 \left(\frac{V}{V_0}\right)^{\alpha_s} - P_0 \left(\frac{V}{V_0}\right)^{\alpha_t} \tag{2.13}$$

$$P_d = P_r + P_0 \left(\frac{V}{V_0}\right)^{\alpha_t} \tag{2.14}$$

where:

P_r: active power recovery

P_d: active power consumption of load

P_s and P_t: steady-state and transient load responses

T_p: active power recovery time constant

α_s: steady-state active power voltage exponent

α_t: transient power voltage exponent

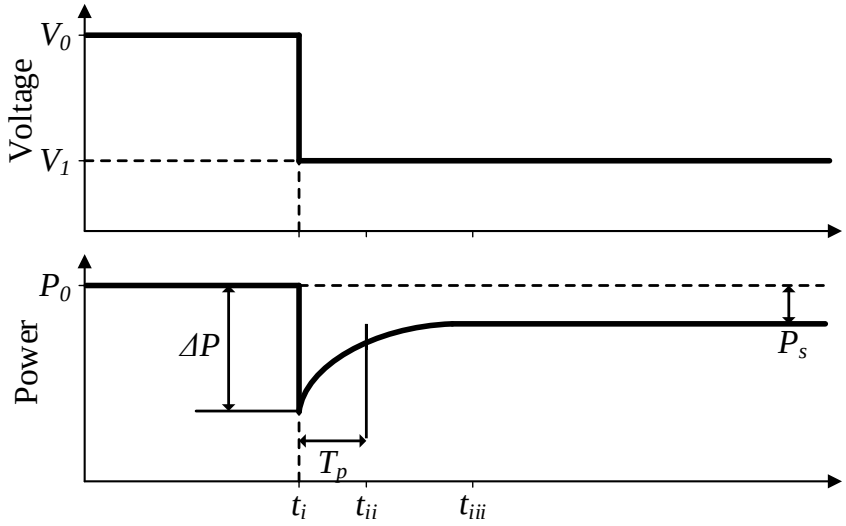

Figure 2.1 Typical response of the exponential dynamic load model adopted from [25]

Similar expressions exist for the reactive power response:

$$T_q \frac{dQ_r}{dt} + Q_r = Q_s(V) - Q_t(V) = Q_0 \left(\frac{V}{V_0}\right)^{\beta_s} - Q_0 \left(\frac{V}{V_0}\right)^{\beta_t} \tag{2.15}$$

$$Q_d = Q_r + Q_0 \left(\frac{V}{V_0}\right)^{\beta_t} \tag{2.16}$$

where all the parameters are as explained for the active power response.

The exponential dynamic load model is suitable for modeling loads with limited percentage of induction motors. This is because the model employs separate equations for active and reactive powers, without considering the inherent coupling between them [27]. Therefore, this model cannot accurately reproduce induction motor dynamics.

2.2.2 Dynamic model of induction motor

When the participation of induction motors in the total demand is significant, an appropriate induction motor model should be used. Dynamic behavior of induction motors is normally represented using the "*dq*" reference frame transformation. Modeling a symmetrical three-phase induction motor using a fifth-order model is discussed in detail in [28], and is used in software

platforms such as Siemens PTI PSS®E and GE PSLF™ [11]. A third-order model of induction motors has been traditionally used as presented in [29].

2.3 Composite load models

Composite load models include both static and dynamic components. The most common form of a composite load model consists of an induction motor model in parallel with a static model. In [7], the static part of the composite model has been represented with a conductance and susceptance in parallel. A ZIP model for the static part has been presented in [30], [31]. WECC composite load model (Figure 2.2) described in [32], [33], enables the representation of power electronics, static load, three-phase induction motors (Motor-A, B and C), single-phase induction motors (Motor-D), and the distribution equivalent network. Static and electronic loads are represented by polynomial models. Drive-controlled motors are classified as electronic loads. Motor-D is the single-phase air conditioner model. It is a "performance model" derived from laboratory testing of air conditioners. The actual measured response of a single-phase compressor motor to a gradual voltage ramp tests has been fitted to two polynomial (quadratic) equations. One for the response while running normally and the other when the unit has stalled. Moreover, transient voltage dips have been applied to the model to determine the depth and duration of dips that would cause the motor to stall.

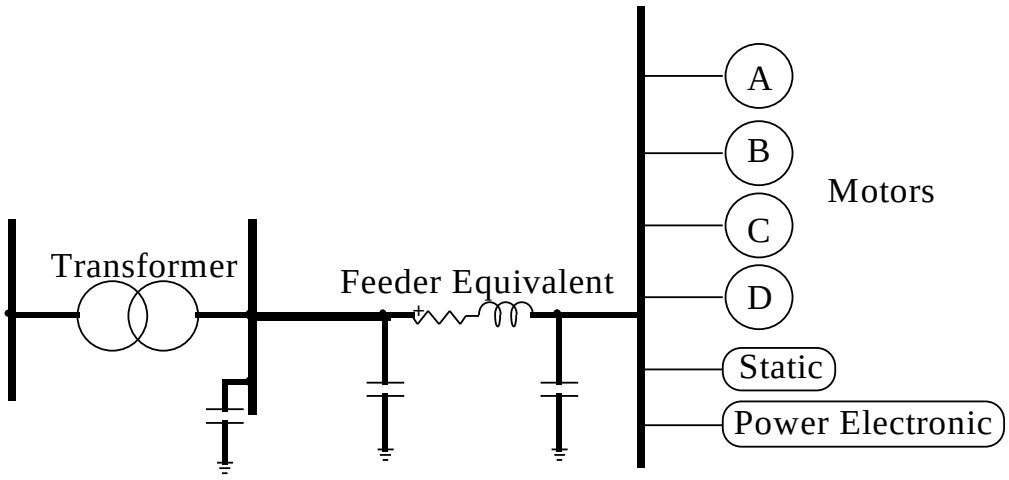

Figure 2.2 WECC composite load model adopted from [32]

2.4 Harmonic load models

The previously discussed load models are able to retain information on the active and reactive power demands of the load, but the harmonic characteristics are not captured. In the topic of harmonic load modeling, load behavior is usually classified as either linear or nonlinear. Linear loads include static components such as resistive lighting and heating devices, as well as rotating loads which are induction and synchronous motors. Nonlinear loads draw current in a non-sinusoidal manner and therefore appear as sources of harmonics. They include power electronic loads, compact fluorescent lighting, adjustable speed drives, etc.

2.4.1 Linear loads

While static loads can be represented in harmonic simulations using their active and reactive powers at fundamental frequency, rotating loads require more sophisticated models. This is because their equivalent impedance cannot be calculated using the active and reactive powers [34]. Several common linear models are presented in this section. In the following text, P and Q are the active and reactive powers of the load, V_0 is the nominal voltage magnitude at fundamental frequency and h is the harmonic order.

Model-1: in this model, the load is assumed to be purely resistive by neglecting the equivalent reactance. This is the case when contribution of motors to the total demand is relatively low. The equivalent resistance is calculated using (2.17) [16].

$$R = \frac{{V_0}^2}{P} \tag{2.17}$$

This model can capture frequency dependency by using larger values of R for higher harmonics i.e., 1.3R for the 5th harmonic and 2R for the 10th harmonic [16].

Model-2: the load is represented as a parallel combination of a resistance R and a reactance X. The reactance captures the motor contribution using the estimated equation (2.18) [34].

$$R = \frac{{V_0}^2}{(1-K)P} \tag{2.18}$$

$$X = X_M \frac{{V_0}^2}{K_m K P}$$

where K is the motor fraction of the total load, K_m is the install factor that can be estimated from the rated motor power factor ($cos\varphi$), i.e., $K_m = \frac{1}{cos\varphi}$. Typically, the install factor equals 1.2 [34]. X_M is the per-unit value of motor locked rotor reactance (typically in the range of 0.15-0.25) [34].

Model-3: this model is based on experimental results at a MV distribution network in France (EDF). It represents the load by a static branch (X_s in series with R) connected in parallel to a rotating branch (X_p), as shown in Figure 2.3. The model parameters are obtained from [16]:

$$R = \frac{{V_0}^2}{(1-K)P} \tag{2.19}$$

$$X_s = 0.073hR$$

$$X_p = \frac{hR}{6.7Ktan\varphi - 0.74}$$

where K is the motor fraction of the total load and $tan\varphi = \frac{Q}{P}$.

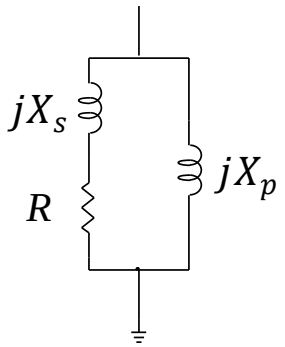

Figure 2.3 Harmonic load model-3

Model-4: this model is a parallel combination of a resistance R and an inductance X. It should be noted that this model neglects the motor loads and should only be used when their fraction is very small. The equivalent parameters are obtained based on (2.20) [18].

$$R = \frac{{V_0}^2}{P} \qquad (2.20)$$

$$X = \frac{{V_0}^2}{Q}$$

Model-5: in this model, a series combination of a resistance *R* and an inductance *X* is used. Similar to Model-4, this model is suitable for cases where the predominant components of the load are not motors. The equivalent parameters are obtained based on (2.21) [34].

$$R = P\frac{{V_0}^2}{P^2 + Q^2} \qquad (2.21)$$

$$X = Q\frac{{V_0}^2}{P^2 + Q^2}$$

Model-6: this model is a representation of motor loads which includes a series combination of a resistance *R* and an inductance *X* . The parameters are calculated in [18]:

$$X = \frac{{V_0}^2}{S_{locked\ rotor}}$$

$$R_1 = \frac{X}{cos\varphi_{start}} \qquad (2.22)$$

$$R = R_1\sqrt{h}\ ;\ \text{Skin effect}$$

where $S_{locked\ rotor}$ is locked rotor slip of motor and $cos\varphi_{start}$ is motor starting power factor which is typically about 0.32 [18].

Model-7: this model is similar to Model-4, but it also captures the frequency dependency of the resistive part [15]:

$$R(h) = R\sqrt{h} \qquad (2.23)$$

Model-8: this model is similar to Model-6, but also uses correction factors for skin effect in stator and rotor [15]:

$$X_{mh} = hX_B \tag{2.24}$$

$$R_{mh} = R_B\left(aK_a + \frac{b}{S_h}K_b\right)$$

$$S_h = \frac{(\pm h - 1)}{\pm h}$$

where R_B and X_B are the motor locked rotor resistance and reactance. K_a and K_b are the correction factors for the skin effect in the stator and rotor circuits. Typically, a= 0.45 and b= 0.55 [15].

Model-9: This model is similar to Model-2, but also includes load transformer and motor damping as illustrated in Figure 2.4. X_1 and R_2 are calculated as (2.20), X_2 and R_1 are obtained from [34]:

$$X_2 = 0.1R_2 \tag{2.25}$$

$$R_1 = \frac{X_1}{K_3}$$

where $K_3 = \frac{X_1}{R_1}$ is quality factor of rotor circuit and typically equals to 8 [34].

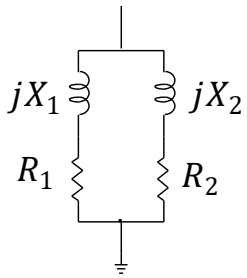

Figure 2.4 Harmonic load model-9

Model-10: this model developed by National Grid TSO in England is shown in Figure 2.5 [35]. The load is represented by a parallel combination of a resistance R_{LV} and a capacitance B_{LV}. The capacitance accounts for power factor correction as well as the capacitance of low voltage cables. B_{HV} represents the total cable capacitance at the high voltage supply bus. X_T is the equivalent reactance of the step-down transformers. A motor component is added in parallel to the load in a similar model used in Scottish Power TSO in Scotland [35].

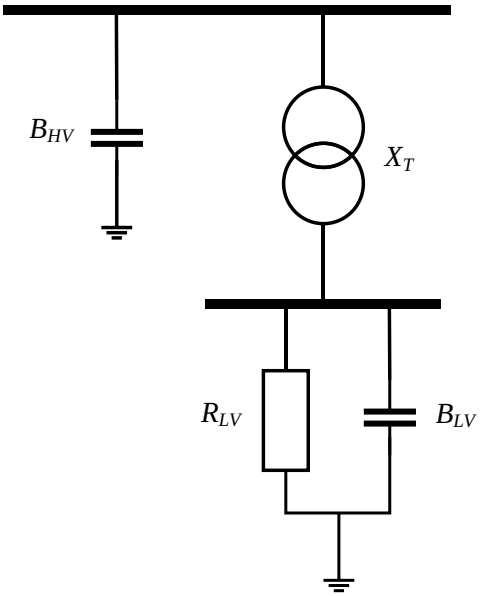

Figure 2.5 Harmonic load model-10

2.4.2 Nonlinear loads

Nonlinear loads draw current in a non-sinusoidal manner and therefore appear as sources of harmonics. They include power electronic loads, compact fluorescent lighting, adjustable speed drives, etc. The proliferation of such loads in power networks accentuates the need to understand their behavior and to capture their characteristics in modeling. Modeling nonlinear loads is usually a complicated task, not only they are harmonic sources, but also, cannot be represented by constant impedances. The type and topology of the nonlinear loads, the interaction with the system impedance, the variation in the harmonic spectra and the effect of controllers on load behavior should be addressed when considering nonlinear loads.

Traditionally, harmonic loads were represented in frequency-domain as ideal constant current sources. In this method, several current sources with specified magnitude, phase angle and frequency are set to replicate the characteristics of the modelled load up to the frequency of consideration [36], [37], [38]. This model structure, known as constant current source (CCS), is depicted in Figure 2.6 and formulated in (2.26).

$$I = \sum_{h=1}^{H} |I|_h \angle\theta_h \tag{2.26}$$

where $|I|_h$ and θ_h are the magnitude and phase angle of the h^{th} harmonic current component, respectively, and *H* is the maximum harmonic order.

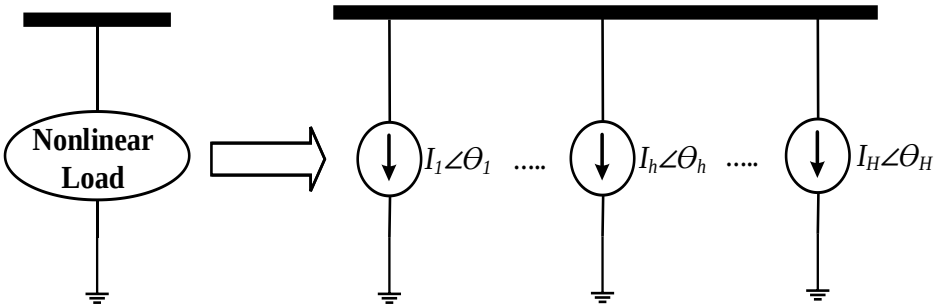

Figure 2.6 CCS model of nonlinear loads

The CCS method has a simple structure and is a reasonable assumption when the application of nonlinear loads is limited to load-commutated converters and diode rectifiers. However, due to the increased penetration of more sophisticated converter-based devices, more accurate representations are required to consider not only the harmonic emissions but also the harmonic impedance of the device, which can affect system resonances [39]. For this purpose, an equivalent Norton circuit shown in Figure 2.7 has been proposed [38], [40].This circuit consists of an ideal current source and equivalent admittance for each frequency of interest.

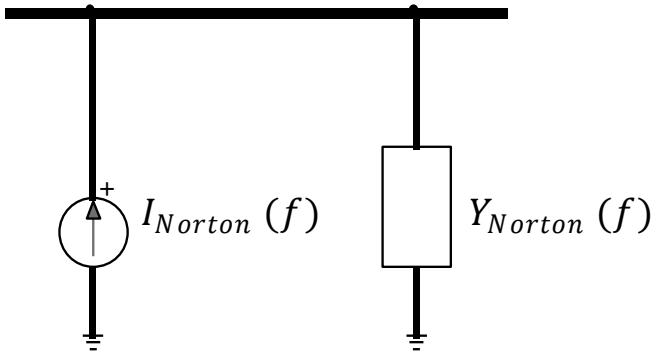

Figure 2.7 Norton equivalent of nonlinear loads

There are cases in which the dependence of the nonlinear load on the operating point needs to be considered. One example is in studies involving controlled power electronics. The operating point of a power converter varies in a complex manner according to its control commands as well as the parameters of its physical components [39]. The harmonic impedance of the device varies correspondingly. As a result, the converter model must be modified for different operating conditions. This can be implemented by means of several look-up tables that presents the harmonic behavior at different operating points. However, if the harmonic impedance and/or emission of the converter is highly dependent on operating point, this approach will raise the need to deal with many look-up tables. In case of nonlinear network components, the time-domain method is often preferred [35]. The time-domain formulation consists of differential equations representing the dynamic behaviour of the power system components. The resulting system of equations is normally solved using numerical integration. Time-domain method can provide detailed modelling of power electronics and therefore is a powerful means to model the nonlinear time-varying behaviour of those devices and their controllers.

2.5 Methodologies for aggregated load model development

After presenting different types of load models, this section describes two commonly used methodologies for developing an aggregated load model.

2.5.1 Measurement-based approach

The measurement-based approach is referred to as “top-down” methodology in which events and disturbances recorded at representative buses are used for matching an assumed load model for the aggregated connected load to the measured data [41], see the diagrammatic representation of Figure 2.8. Data acquisition devices such as Power Quality Meters (PQM) and Digital Fault Recorders (DFR), will record voltage and/or frequency variations as well as the response of the load to the natural disturbances or staged tests. Signal processing techniques [42] are applied in order to calculate fundamental components of voltage, current, active power and reactive power. Next, a suitable load model is selected, and the corresponding load model parameters are identified. The values of the parameters are estimated through an optimisation process such that the error between the measured response and model response is minimised. Different optimisation

techniques have been used in the past to estimate the parameters, e.g., a genetic algorithm in [43]. Finally, the derived model is validated using simulation tools. The simulated power responses coming from the proposed model are compared with the actual recorded active and reactive power responses. If the responses are not satisfactory, the procedure should be repeated by changing the assumed load model. This approach has been implemented for fitting parameters to an exponential load model in [44]. Other examples of this modelling technique are available in [8],[45].

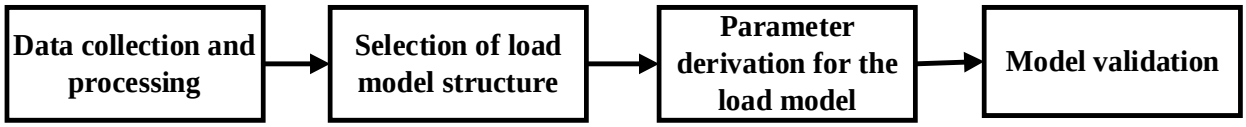

Figure 2.8 Measurement-based approach

The main advantage of the measurement-based approach is the use of recorded data from the actual system and no required knowledge on the actual load composition. Nevertheless, optimisation techniques rely on the initial estimate of variables. Therefore, a baseline model using the component-based approach where some estimates of the underlying components have been computed is beneficial to begin a practical measurement-based parameterization. The main disadvantage is that this approach relies almost entirely on the availability of measurement data coming from the field. Usually there is lack of appropriate measurement data required for load model derivation and parameter estimation processes.

2.5.2 Component-based approach

The component-based approach can be described as “bottom-up” approach, as an aggregated load model is derived from the models of its individual load components, see the diagrammatic representation of Figure 2.9. The description of this method has been provided in [41]. The supplied load at each bus is grouped into different sectors. Each sector consists of different load categories. Load categories of each sector represent the typical structure of electrical devices and equipment found in its end-use application. Each load category includes several types of load components with similar electrical characteristics. Each component contributes some fraction to the total load demand and is represented by its specific model. Therefore, three datasets are required to implement the component-based load modelling approach:

1. percentage contribution of each load sector to the total active power demand of the total load;

2. percentage contribution of each of load component to the active power demand of a particular load sector, which is known as load composition;

3. individual load models which represent the electrical characteristics of load components.

Component-based approach has been reported in [9], [46], [47] to develop aggregated household, industrial and residential-commercial loads, respectively. The main advantage of this approach is that the load model can be developed based on the knowledge on participating load components, as well as customer survey data and available literature on the load composition. The main disadvantage is the difficulty of obtaining accurate data related to composition at the desired load bus.

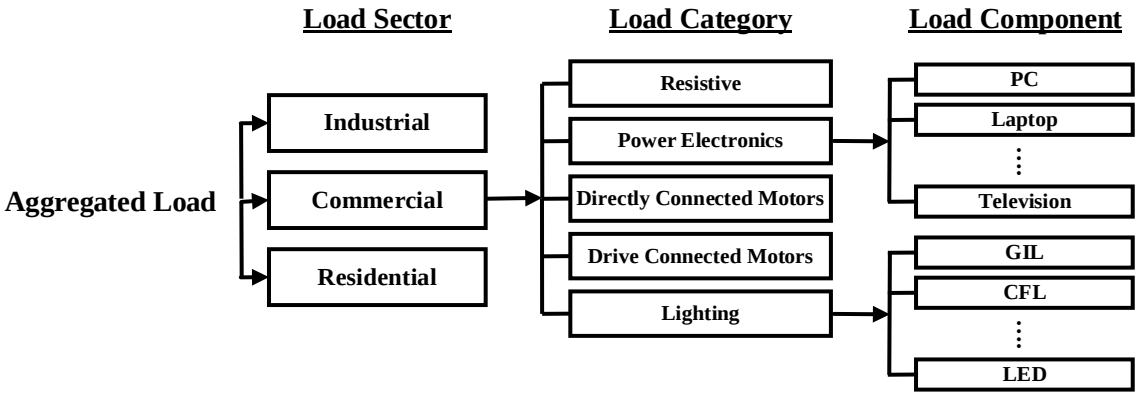

Figure 2.9 Component-based approach

The main source of component-based modelling technique is the Western Electricity Coordinating Council (WECC) as described in Section 2.3. The last major review of this model has been published in [11]. The model has been implemented under different names i.e., CMLD and CMPLDW, in different software (Siemens PTI PSS®E [48] and GE PSLF™ [49]). Implementation of the model may be slightly different, but the principles and parameters are generally the same.

2.6 Summary

This chapter was a general overview of the load modelling research area. Existing load models including static, dynamic and composite models as well as harmonic models were introduced. Measurement-based and component-based approaches were presented as current load modelling methodologies.

CHAPTER 3 LOAD COMPONENTS

To develop the new aggregated load model, the component-based aggregation approach is adopted in this thesis as described in Chapter 2. In this approach, the aggregated load model is derived from the models of its individual load components. This chapter covers modeling of individual load components as the first step toward developing the desired aggregated model.

In this thesis, the majority of components found in different load sectors are divided into five general load categories; resistive loads, switch-mode power supplies, lighting sources, single-phase and three-phase directly connected motors and three-phase drive-controlled motors. As was mentioned in Chapter 1, the proposed load model is an EMT-type model. Therefore, individual load component models are implemented as EMT-type equivalent circuits in the time-domain simulation tool EMTP®. In such models, the electrical elements within the circuits of loads are identified and corresponding models are developed based on the circuit topology. The component models presented in this chapter are implemented in per-unit form (pu). Such models allow the representation of aggregated components according to their participation level in the complete load model. Component-based aggregation of the developed component models will be explained in the next chapter.

3.1 Resistive load category

Operation of cooking devices as well as electrical space/water heaters is based on a resistive heating element which heats the surrounding air or water. This load category is represented by a constant resistance.

3.2 Switch-mode power supply

This section focuses on modeling dc power supplies. The most common examples of this load category include computers, monitors, televisions, DVD/CD players/recorders, etc. Dc power supply loads are often referred to as switch-mode power supplies (SMPS). The existing models for this load category are in the exponential or polynomial forms as previously presented in (2.1) and (2.5), shown in Table 3.1. Models for two sets of office equipment (computers, monitors, printers and fax machines) have been derived in [50] using laboratory measurements. A model for

television set has been provided in [51]. Reference [23] has presented a model for televisions and computers. References [10] and [52] have generally referred to electronic load as constant power. Constant power characteristics can also be observed in the results presented in [53].

Table 3.1 Existing load models for SMPS load category

Load Component	**Exponential Model**		**Polynomial Model**					
	n_p	n_q	Z_p	I_p	P_p	Z_q	I_q	P_q
Office Equipment 1 [50]	0.24	0	0.34	-0.32	0.98	0	0	0
Office Equipment 2 [50]	0.2	0	0.08	0.07	0.85	0	0	0
Television [51]	2	5.1	-	-	-	-	-	-
Television and Computer [23]	2	5.2	-	-	-	-	-	-
Electronic Load [10], [52]	0	0	-	-	-	-	-	-
SMPS [53]	0	-0.5	0	0	1	0.45	-1.44	1.99

3.2.1 SMPS topology

Although the existing static load models offer some insight into the general characteristics of the switch-mode power supplies (SMPS), EMT circuit-based models are employed throughout this thesis. This approach considers the components within the circuits of electrical loads and develops models based on the circuit topology. Although it is not the purpose of this thesis to model the full SMPS circuit, some general knowledge on the circuit topology provides some understating on its characteristics. Therefore, a brief overview of SMPS topology and its components is first addressed.

SMPS load category contains a single-phase diode bridge rectifier for the conversion of ac to dc voltage. Electronic circuits are sensitive to voltage variations in the applied dc voltage and therefore a regulated dc voltage supply is required. For this reason, a dc-dc converter is included to stabilize the rectifier output voltage. A typical SMPS load includes some other components which are shown

in the block diagram of Figure 3.1: electromagnetic interference (EMI) filter, power factor correction (PFC) circuit and inrush current protector [54].

Figure 3.1 General block diagram of SMPS circuit topology adopted from [54]

3.2.2 SMPS circuit-based model

The full circuit model of SMPS shown in Figure 3.1 have been developed in the previous research [53]. However, it is not the purpose of this thesis to model the full SMPS circuit. Due to the complexity and long simulation times, this model is not straightforward for aggregation. Instead, previous research [53], [55], [56] have shown that the full circuit model can be accurately represented by a simplified equivalent circuit. In Figure 3.1, if the dc-dc converter and the components downstream be represented by an equivalent resistance, the equivalent circuit takes the form of Figure 3.2. This circuit consists of a diode bridge rectifier, the equivalent resistance and a passive PFC element which is an inductance added to the rectifier circuit to reduces harmonic content of the current drawn by the device. The values of the filter components and inrush current protection circuit in the circuit of Figure 3.1 are very small such that their effect on the electrical characteristics of the load can be neglected.

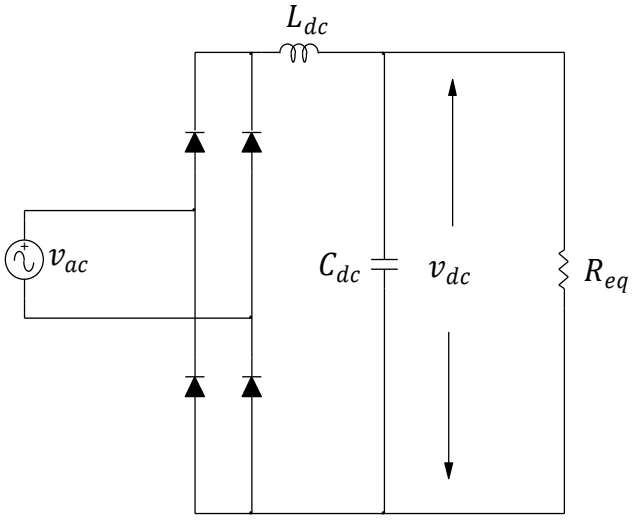

Figure 3.2 Equivalent circuit of SMPS model

In Figure 3.2, R_{eq} is the equivalent resistance, v_{dc} is the instantaneous rectifier dc-link voltage, C_{dc} is dc-link capacitor and L_{dc} is passive PFC inductor. The equivalent resistance can be determined using an analytical expression which describes the behavior of all the components downstream of C_{dc} [53]:

$$R_{eq} = \frac{v_{dc}^2}{P_{SMPS}} \tag{3.1}$$

where P_{SMPS} is the rated power of SMPS load. Typical values of components L_{dc} and C_{dc} have been presented in [53]. Per-unit reactance of $X_{L_{dc}}$= 0.03 pu has been suggested to meet the harmonic limits. The value for dc-link capacitance has been selected based on the hold-up time requirements. Hold-up time is the amount of time that the device can maintain the dc-link voltage within the specified voltage range during power interruption. A common industry practice is to select the value of C_{dc} to satisfy a hold-up time of about 20 ms. Based on this criterion, the per-unit reactance value of C_{dc}, $X_{C_{dc}}$= 0.036 pu has been proposed in [53].

3.2.3 EMTP model of SMPS

The model of the SMPS was developed in EMTP®, based on the equivalent circuit previously shown in Figure 3.2. The EMTP® schematic of the circuit is illustrated in Figure 3.3 (refer to *"SMPS"* EMTP file). In the dashed-line box, the dc-link voltage is determined and used as the input value to the user-defined function f which implements (3.1) and yields R_{eq} which is the equivalent resistance. P_{SMPS} is the desired rated power of the SMPS load. R_{eq} is then applied to a variable (controlled) resistor, R(t) whose resistance is adjusted using this control signal.

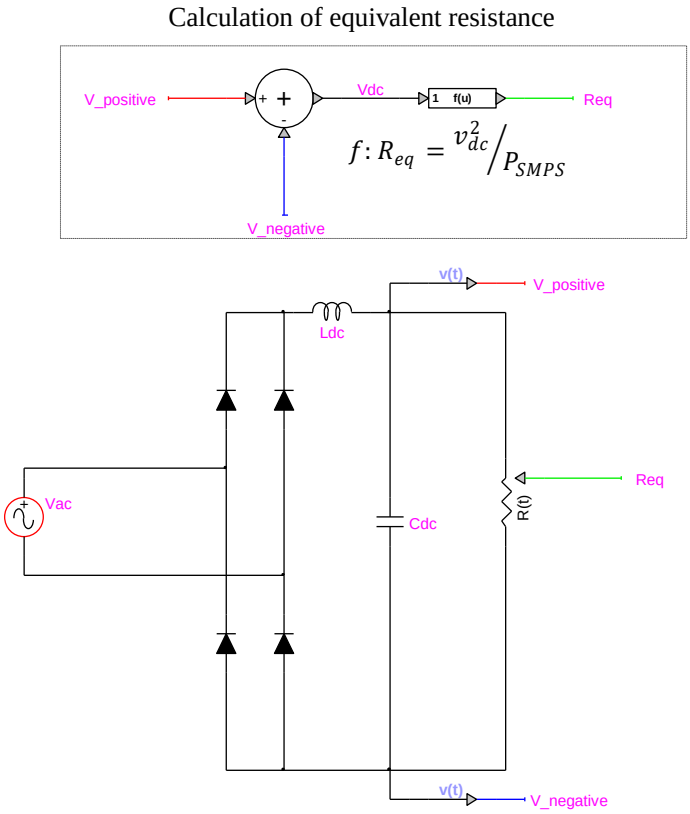

Figure 3.3 EMTP equivalent circuit of SMPS model

In order to validate this model, its equivalent exponential coefficients, n_p and n_q defined in (2.1) and (2.2), were obtained and compared to the results presented in [53] and previously listed in Table 3.1. This was achieved by performing a voltage ramp test on the developed model and obtaining the active and reactive power demands. For this purpose, a ramping voltage source was built in EMTP® and applied to the circuit of Figure 3.3. The implementation of the source is shown in Figure 3.4. The desired voltage amplitude (A) and frequency (f) of the source are defined in the signal generator. This signal is then multiplied by a desired voltage ramp function created using EMTP® table function, which is a look-up table of value pairs, see Figure 3.5. In this table, "x" corresponds to "time" (which is the input to the table function), and f(x) corresponds to per-unit voltage values at each time. The number of value pairs is arbitrary, and the look-up values will be interpolated between the specified value points. In this case study, the voltage source was set to ramp from 1 pu to 1.25 pu between t=3 s to t=5 s as shown in Figure 3.5. The output of the *product* function is the control signal which is applied to a controlled voltage source.

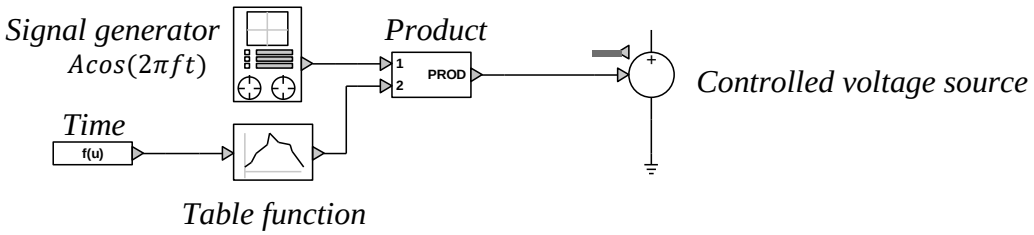

Figure 3.4 Structure of the ramping voltage source

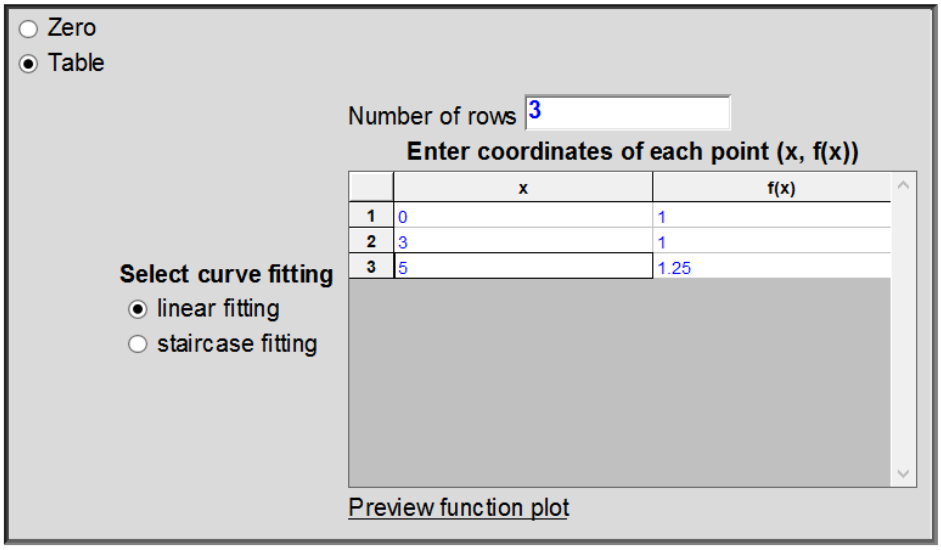

Figure 3.5 Table function employed in the structure of the ramping voltage source

The resulting P-V and Q-V characteristics by applying the ramping voltage source to the circuit of Figure 3.3 are shown in Figure 3.6. Curve fitting techniques can be used to fit an exponential model to the derived characteristics and find exponents n_p and n_q. Alternatively, as previously discussed in Section 2.1, the exponents correspond to the partial derivatives of active and reactive powers with respect to voltage. In this way, exponential coefficient deducted from characteristics of Figure 3.6 are n_p = 0 and n_q= -0.6. As the supply voltage magnitude increases, the value of the reactive power reduces. This can be attributed to the increased voltage drop across the inductance which in turn leads to slower rate of charge of the capacitor. As a result, the power factor improves, and the reactive power reduces. The obtained values are close to the ones presented in [53] and previously

listed in Table 3.1 (n_p = 0 , n_q = -0.5) with a slight difference which is attributed to different system frequencies i.e., 60 Hz vs 50 Hz. This validates the developed SMPS model.

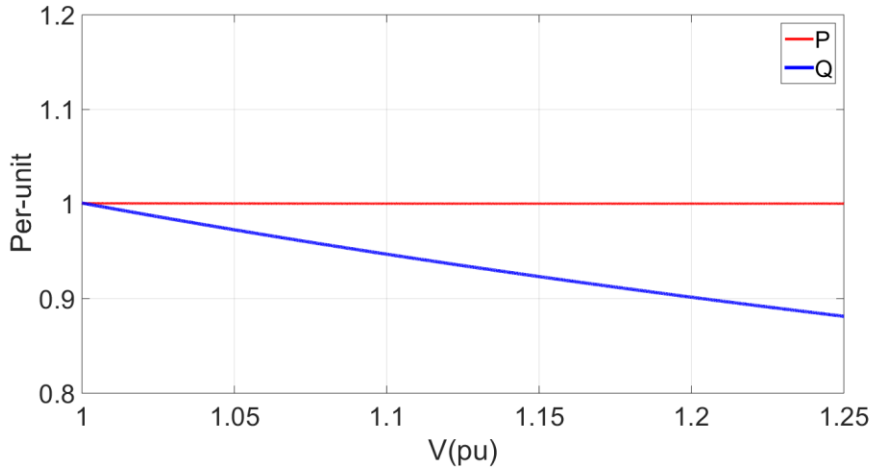

Figure 3.6 P-V and Q-V characteristics measured at the terminals of SMPS equivalent circuit

3.3 Lighting sources

This section investigates the characteristics of lighting components. Different types of lighting sources include general incandescent lamps (GILs), compact fluorescent lamps (CFLs), linear fluorescent lamps (LFLs), halogen incandescent lamps (HILs) and light emitting diodes (LEDs). Exponential and polynomial models of lighting sources are available in the literature as summarized in Table 3.2. GIL has active power characteristics between constant current and constant resistance [10], [51]. Exponential models of LFL have been reported in [23], [50], [51], [23]. Although the reactive power characteristic is different among the presented models, there is a general agreement on the active power characteristics close to constant current. The constant current characteristics can also be observed in CFL models suggested in [50],[53],[57],[58]. However, references [10], [59] have recommended to use constant power models for the discharge lighting category. The exponential and polynomial models of LED have been reported in [54] by means of measurements on several existing variations. It can be observed that there is a significant spread in the electrical characteristics of LEDs. Model parameters are strongly influenced by the type of the lamp. The active power varies in range including approximately constant power,

approximately constant current, and approximately constant impedance. The reactive power characteristic varies in a wider range with n_q from -1.14 to 3.59.

Table 3.2 Existing load models of lighting load category

Load Component	**Exponential Model**		**Polynomial Model**					
	n_p	n_q	Z_p	I_p	P_p	Z_q	I_q	P_q
GIL [10]	1.6	-	-	-	-	-	-	-
GIL [51]	1.55	-	-	-	-	-	-	-
LFL [51]	1.7	5	-	-	-	-	-	-
LFL [51]	1	3	-	-	-	-	-	-
LFL [51]	1	4.6	-	-	-	-	-	-
LFL [23]	0.96	7.38						
LFL [50]	0.49	0	-2.48	5.46	-1.97	0	0	0
CFL [50]	0.95	0.31	0.14	0.77	0.09	-0.06	-0.34	-0.6
CFL [50]	1.03	0.46	0.16	0.79	0.05	0.18	-0.83	-3.5
CFL [57]	-	-	-0.42	1.5	-0.06	0.66	-1.16	0.06
CFL [58]	1	0.35	-	-	-	-	-	-
CFL [53]	0.94	0.52	-0.01	0.96	0.05	0.1	-0.73	-0.37
LED 1 [54]	2.4	3.59	0.79	0.82	-0.62	4.12	-4.59	1.48
LED 2 [54]	-0.01	-1.14	-0.92	1.84	0.09	-0.49	-0.22	1.7
LED 3 [54]	1.07	0.83	-4.24	9.56	-4.32	-8.48	17.8	-8.31
LED 4 [54]	0.1	0.91	-0.86	1.82	0.04	0.39	0.14	0.48

Beside the presented static models, some analytical models have been presented in the literature for CFL tubes; Table 3.3 gives an overview. Most of the existing models present relationships between instantaneous current and voltage [60], [61], [62], [63]. However, some references [53], [54], [64], [65] have used the tube rms V-I characteristics to produce the tube model. Another group [66], [67], [68] has presented the equivalent resistance. It can be observed that several forms of analytical expressions, i.e., linear relationships, higher order quadratic equations, exponential functions, and logarithmic relationships, have been developed in the literature in order to produce the tube model.

Table 3.3 Existing fluorescent tube models

Reference	Tube Model
[60]	$v_T(t) = Ai_T(t) + Bi_T^3(t)$
[61]	$v_T(t) = \left(A + \frac{B}{I_T}\right) i_T(t)$
[62]	$v_T(t) = Ai_T(t) + (Bi_T(t))^3$
[63]	$v_T(t) = \frac{A_0 + A_1 e^{-A_2 I_T} - A_3 e^{-A_4 I_T}}{I_T} i_T$
[64]	$V_T = \frac{1}{A + BI_T}$
[65]	$V_T = A_0 + A_1 e^{-A_2 I_T} - A_3 e^{-A_4 I_T}$
[53],[54]	$V_T = AI_T^2 + BI_T + C$
[66]	$R_T = \frac{A}{P_T} - B$
[67]	$ln(R_T) = Aln(I_T) + B$
[68]	$R_T = \frac{A}{I_T} + BI_T + C$

where i_T and v_T are the instantaneous tube current and voltage, I_T and V_T are the tube rms current and voltage, P_T is tube rated power, R_T is tube equivalent resistance and A, B, C and A_0 to A_4 are tube coefficients, obtained from measurements.

The overall trend in improving the energy efficiency of power system loads has made formerly CFL and now LED technologies increasingly dominant. Hence, beside traditional GIL, this thesis focuses on those two types of lighting sources. Both CFL and LED have characteristics different than traditional GIL and should be represented with load models which are able to correctly reproduce their electrical behavior.

3.3.1 Incandescent lamps

As previously demonstrated in Table 3.2, incandescent lamps have active power characteristics between constant current and constant resistance. This is because a large temperature swing occurs

in the filament when supply voltage changes and hence the filament resistance changes accordingly. Therefore, incandescent can be represented using an exponential model as following:

$$P = P_0 \left(\frac{V}{V_0}\right)^{n_p} ;\ n_p = 1.55\text{-}1.6 \text{ (see GIL in Table 3.2)} \tag{3.2}$$

where V and P are the actual voltage and active power of the lamp, V_0 and P_0 are nominal voltage and active power of the lamp.

3.3.1.1 **EMTP model of incandescent lamp**

The model of the incandescent lamp was developed in EMTP® based on (3.2), i.e., an exponential model with the coefficient $n_p = 1.55$. The EMTP schematic of the incandescent lamp circuit is depicted in Figure 3.7 and includes a variable (controlled) resistance (refer to *"Incandescent"* EMTP file). In the dashed-line box (1), the resistance rms voltage is determined and used as the input parameter to the user-defined function f_1 which implements (3.2) and yields actual power P. In this function, V_0 and P_0 are desired nominal voltage and power of the lamp. In the dashed-line box (2), the square of the measured voltage is divided by P in order to calculate the value of the resistance, using function f_2. This is the control signal applied to the variable resistance.

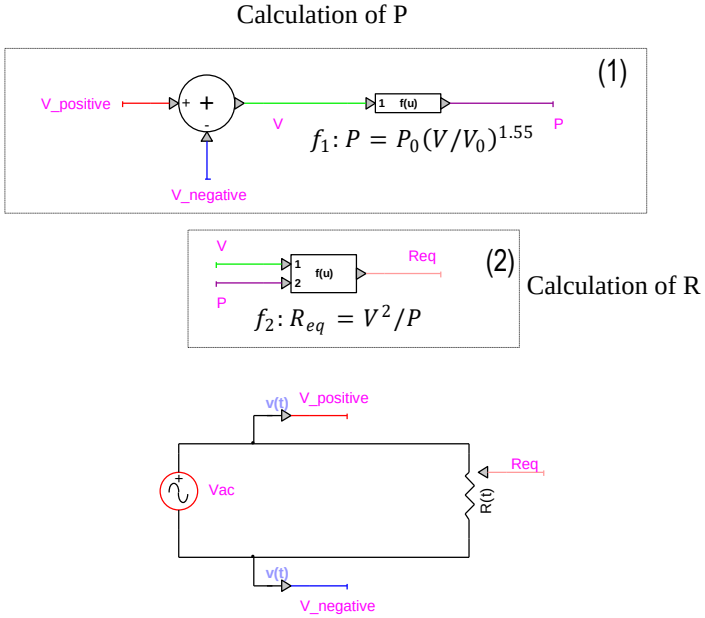

Figure 3.7 EMTP equivalent circuit of incandescent lamp model

3.3.2 Compact fluorescent lamps

3.3.2.1 **CFL topology**

CFL tube includes two electrodes on both ends which are coated with Barium. When a current is applied to the electrodes, electrons are emitted from Barium and strike Mercury atoms inside the tube which in turn ionize Mercury and result in forming a plasma. This process initiates the radiation of Mercury in Ultraviolet form. Tube's inner surface contains phosphors (a fluorescent powder) whose function is to convert Ultraviolet light into visible light. Ionization of Mercury requires a high voltage, called the striking voltage. This is achieved using a ballast circuit. Traditionally, simple ballast circuits have been used, referred to as magnetic ballast which consisted of a large value inductor, a capacitor and a starter switch. Magnetic ballasts have been replaced by electronic ballasts because of higher efficiency, smaller size and ability to reduce flicker which was an issue in magnetic ballasts. A general block diagram of electronic ballast CFL is shown in Figure 3.8. Beside the ballast circuit, it includes a bridge rectifier, EMI filter and an inverter. Further details on the components can be found in [53], [69].

Figure 3.8 General block diagram of CFL circuit topology [53]

3.3.2.2 **CFL circuit-based model**

The full circuit model of CFL shown in Figure 3.8 has been developed in the previous research [53]. First a tube model (see Table 3.3) has been developed and then incorporated with a detailed ballast circuit model to build the full circuit of CFL. However, it is not the purpose of this thesis to model the full CFL circuit. Due to the complexity and long simulation times, it is not straightforward for load aggregation. Instead, the full circuit has been reduced to an equivalent model in [53] which is adopted in this thesis. In this equivalent model, components downstream of the diode bridge rectifier in Figure 3.8 were represented as an equivalent resistance to form an equivalent circuit as shown in Figure 3.9.

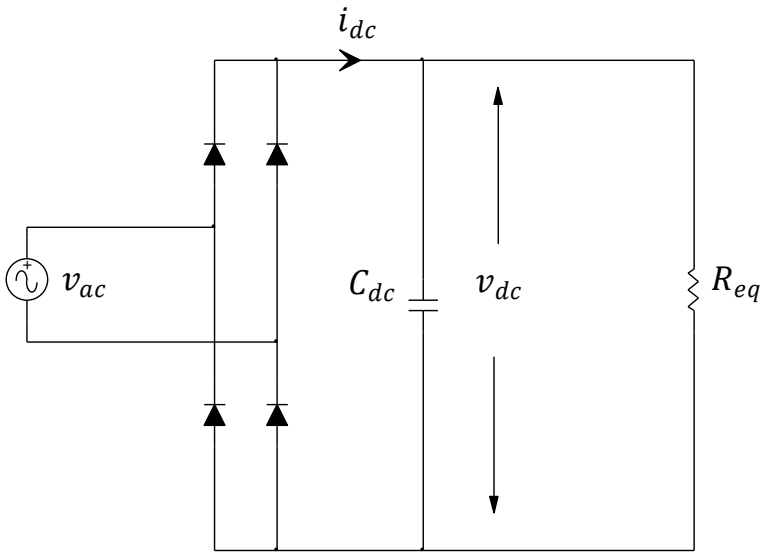

Figure 3.9 Equivalent circuit of CFL model

In [53], the equivalent resistance R_{eq} has been derived by finding the relationship between the instantaneous dc-link voltage, v_{dc} and the instantaneous dc current, i_{dc} using the full circuit model. To do so, i_{dc} of the full circuit model (Figure 3.8) has been plotted versus v_{dc}. Two distinct regions in this *v-i* curve have been identified. One region for the period when C_{dc} is discharging and a second region for the time it is charging. Next, the equivalent resistance R_{eq} has been determined by dividing the value of v_{dc} by corresponding i_{dc}, in each of the two regions. To derive expressions for this equivalent resistance, R_{eq} has been plotted versus v_{dc} in the two mentioned regions. Next, two functional relationships have been developed for fitting the results of R_{eq} as a function of v_{dc} to polynomial equations. A linear polynomial function for the discharge period, and a quadratic function for the charging period:

$$R_{eq1} = 23.7v_{dc} + 274 \tag{3.3}$$

$$R_{eq2} = 11v_{dc} + 0.021v_{dc}^2 + 1300$$

where R_{eq1} and R_{eq2} are the equivalent resistance during discharging and charging stage of the dc-link capacitor.

The size of C_{dc} has been selected as a trade-off between satisfying legislative harmonic limits [70] and tube lifetime. A smaller value of C_{dc} will lower the harmonic content but increase the ripple

content of the dc-link voltage and in turn increase the crest factor. The crest factor of a current is defined as the ratio of the rms current to peak current. The high crest factor imposes electrical stress on the tube, and hence shortens of the tube lifespan. These two criteria define upper and lower limits for the size of C_{dc} in CFL applications. A realistic per-unit value of C_{dc} has been presented as $X_{c_{dc}}$= 0.25 pu [70].

3.3.2.3 **EMTP Model of CFL**

The model of the CFL was developed in EMTP®, based on the equivalent circuit previously shown in Figure 3.9. The EMTP schematic of the CFL circuit is depicted in Figure 3.10 (refer to *"CFL"* EMTP file). In the dashed-line box (1), the dc-voltage is determined and used as the input parameter to two user-defined functions f_1 and f_2 which implement (3.3), and produce the two functional expressions for the equivalent resistances R_{eq1} and R_{eq2}. These two signals are then applied to two controlled resistances, see box (3). An "if" statement (box (2)) in combination with two switches (boxes (4)), are used to select the appropriate resistance based on charging or discharging state of the capacitor. If the measured current is greater than zero, i.e., the charging stage, "Charge" signal which is applied to switch "SW2" becomes 1 and expression R_{eq2} is selected. Otherwise, signal "Discharge" is applied to "SW1" and expression R_{eq1} is selected.

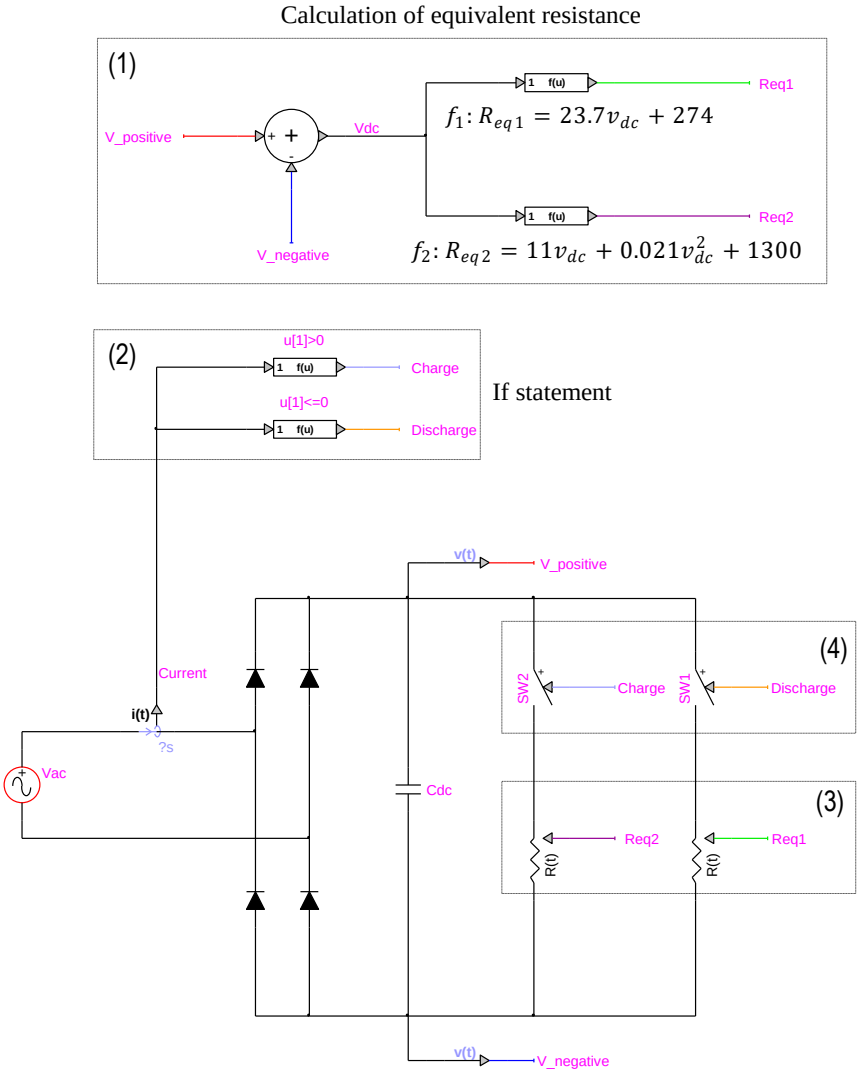

Figure 3.10 EMTP equivalent circuit of CFL model

In order to validate this model, its equivalent exponential coefficients (n_p and n_q) were derived and compared to the results presented in [53] and previously listed in Table 3.2. The methodology applied here is similar to that presented for SMPS, which is performing a voltage ramp test on the developed circuit to obtain the exponents. As demonstrated in Figure 3.4 and Figure 3.5, the voltage source ramps from 1 pu to 1.25 pu. The resulting P-V and Q-V characteristics are shown in Figure 3.11. The exponential coefficients which are partial derivatives of active and reactive powers with respect to voltage are deducted as n_p = 1.1, n_q= 0.9. These values are close to the ones presented in [53] and previously shown in Table 3.2 (n_p= 0.94, n_q= 0.52) with a slight difference which is

attributed to different system frequencies i.e., 60 Hz vs 50 Hz. This validates the developed CFL model.

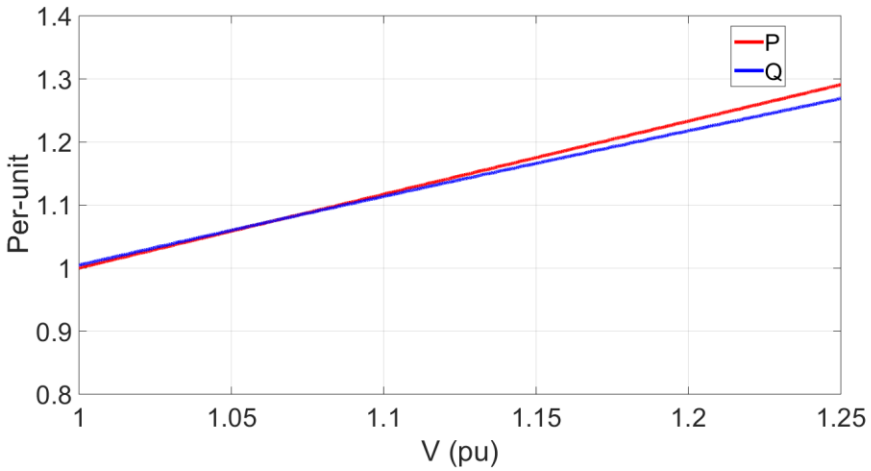

Figure 3.11 P-V and Q-V characteristics measured at the terminals of CFL equivalent circuit

3.3.3 Light emitting diodes

Improved brightness, lower energy consumption and longer life spans offered by LED lights have boosted their use in range of applications especially in the case of commercial buildings where a significant portion of the total energy consumption comes from lighting.

3.3.3.1 **LED topology**

LEDs include semiconductors that emit light when current flows through. Electrons in the semiconductor device recombine with electron holes, releasing energy in the form of photons in the visible light spectrum. LED operation is governed by standard diode mechanisms, which describes the relationship between the voltage and current, and is often referred to as the diode equation:

$$I_D = I_0\left[e^{\left(\frac{qV_D}{nkT}\right)} - 1\right] = I_0\left[e^{\left(\frac{V_D}{nV_T}\right)} - 1\right] \tag{3.4}$$

where I_D and V_D are diode current and voltage, I_0 is reverse saturation current, q is the charge on the electron (1.62×10^{-19}), n is the ideality factor that typically varies from 1 to 2, depending on the fabrication process and semiconductor material, and is set equal to 1 for the case of an ideal

diode, *k* is the Boltzmann constant (1.3805× 10^{-23}) and *T* is the temperature. $\frac{KT}{q}$ is also known as thermal voltage V_T. At room temperature V_T=29.5 mV.

In this thesis, LED is modeled using the piecewise linear model of diode which approximates the diode characteristic of (3.4) as a series of linear segments. It consists of a voltage source and a resistance in series [71], as shown in Figure 3.12. The I-V relationship of this model is given in:

$$V_d = R_d I_d + V_{thr} \tag{3.5}$$

where V_d and I_d, are the rated voltage and current, R_d is the resistance and V_{thr} is diode threshold voltage.

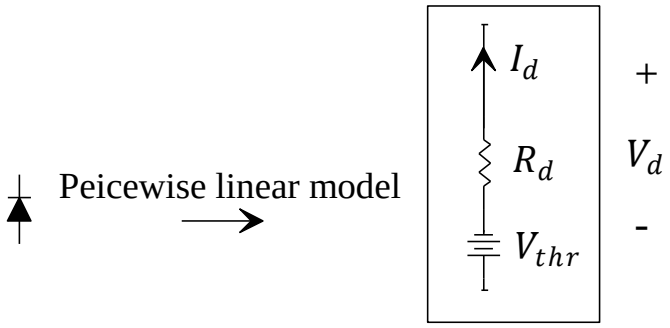

Figure 3.12 Piecewise linear model of LED

3.3.3.2 **LED circuit-based model**

An LED model was developed in EMTP® based on its circuit structure and principles of operation. Figure 3.13 shows the general structure of the LED circuit. Unlike CFL, LED technology does not involve the ionization procedure and hence does not require the ballast circuit. Instead, a driver circuit is required to convert the ac supply voltage to a dc voltage suitable for operation of LED modules (normally 12-24 V). Moreover, the driver circuit can protect the device from voltage or current fluctuations. A change in voltage could cause a change in the current being supplied to the LED. Because of the almost linear relationship between the LED current and its luminous output [72], the current fluctuation is transformed to luminous fluctuation. Therefore, LED lighting is particularly susceptible to flicker, and the driver circuit keeps the current flowing through LED at rated level and ensures a stable light output. Different driver circuits have been presented in

literature, e.g., [73], [74]. An overview on the main driver topologies of is given in [75]. Details of the components in Figure 3.13 are explained in the following section.

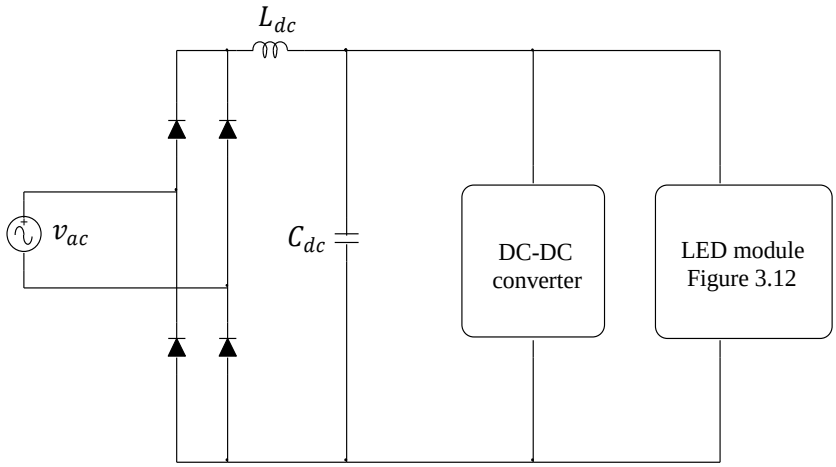

Figure 3.13 Equivalent circuit of LED model

3.3.3.3 **EMTP model of LED**

The model of the LED was implemented in EMTP based on the circuit of Figure 3.13. The EMTP schematic of the model is depicted in Figure 3.14 (refer to *"LED"* EMTP file).

LED modules are series-parallel combination of single LED chips for obtaining higher output power. Throughout this thesis, 30 W LED modules are used as a common wattage for LED lighting. An LED module can be simulated by adjusting the threshold voltage and the resistance in Figure 3.12. The 30 W module was simulated by setting V_{thr}=12 V and R_d=1.5 Ω which corresponds to 5 series strings of 2 parallel individual chips. This is because each individual 3 W LED chip has a threshold voltage of 2.4 V and dynamic resistance of 0.6 Ω [76].

For the driver, a flyback converter was selected as it is one of the most common driver topologies. In this driver topology as shown in Figure 3.14, the input dc source (v_s) and a controlled switch (*SW*) are connected in series with the primary of a flyback transformer. The diode (*D*) and the output filter (C_o) are connected in series with the secondary of the transformer. The flyback transformer model includes a magnetizing inductance and an ideal transformer with a turn ratio of $n = \frac{N_2}{N_1}$. The dc voltage transfer function of the flyback converter is:

$$\frac{V_o}{V_s} = \frac{D}{n(1-D)} \tag{3.6}$$

where D is switch duty ratio. In order to drive the considered 30 W LED module with its rated voltage of 15 V, the adjusted values in the above equation are n= 0.17 and D= 0.15.

As LED circuits are similar in structure to the SMPS, the same per-unit values were considered for C_{dc} and L_{dc}, $X_{C_{dc}}$= 0.036 pu and $X_{L_{dc}}$= 0.03 pu.

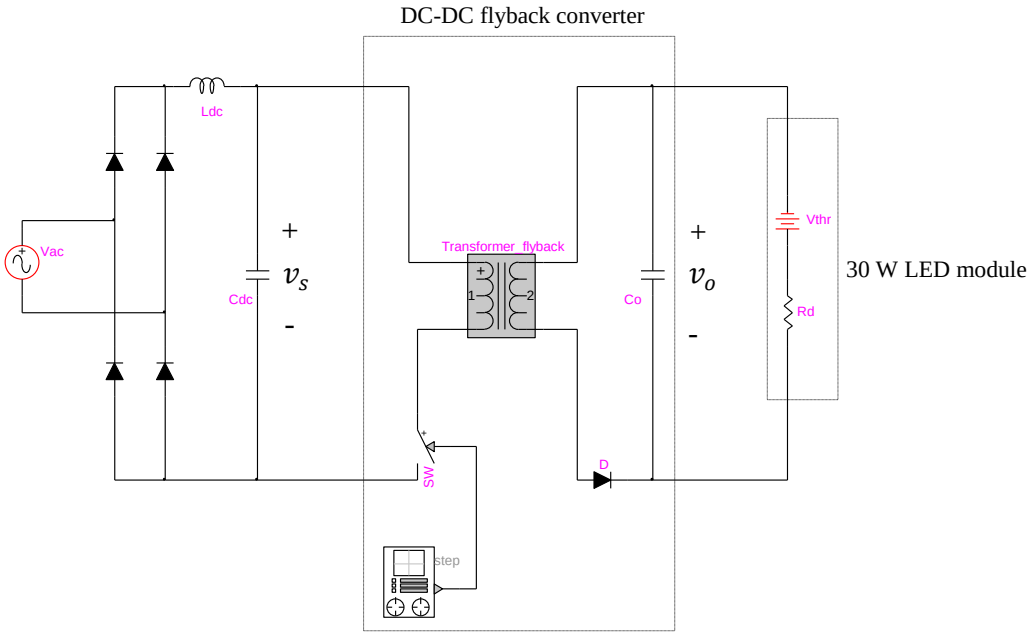

Figure 3.14 EMTP equivalent circuit of LED model

In order to validate this model, its equivalent exponential coefficients (n_p and n_q) were derived and compared to the results presented in [54] and previously listed in Table 3.2. The methodology applied here is similar to the previous loads which is performing a voltage ramp test on the developed circuit and obtaining the exponents n_p, n_q. As demonstrated in Figure 3.4 and Figure 3.5, the voltage source ramps from 1 pu to 1.25 pu. The resulting P-V and Q-V characteristics are shown in Figure 3.15. The exponential coefficient deducted from those characteristics are n_p=2 and n_q=1.9. They are in the range of values presented in Table 3.2. This validates the developed LED model.

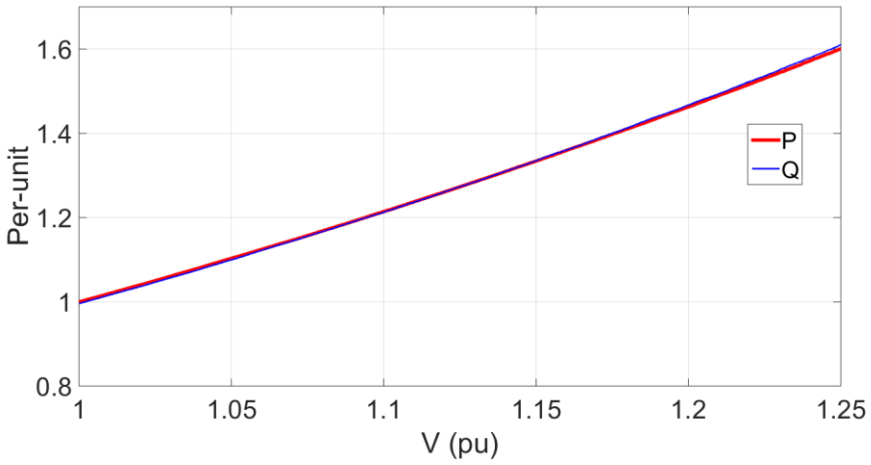

Figure 3.15 P-V and Q-V characteristics measured at the terminals of LED equivalent circuit

3.4 Induction motor

The induction motors (IM) can be categorized in several ways. In this thesis, they are categorized with respect to their electrical connections (single-phase or three-phase) and their mechanical load types. Normally three types of mechanical load types exist: variable torque (VT), constant torque (CT) and constant mechanical power (CP) loadings [77]. For VT, load torque requirement varies either as a linear (LT) or quadratic function (QT) of the changes in motor speed. For CT, torque is constant and not a function of motor mechanical speed. Finally, for CP, the torque varies inversely to the motor speed.

3.4.1 Single-phase induction motors

Single-phase IMs make up a significant proportion of the total energy consumed in the residential load sector. They are used in range of applications such as refrigerators, washing machines and dish washers, cloth dryers, air conditioners and heat pumps [28]. These motors are usually directly connected. At the moment, drive-controlled single-phase IM is not widespread within the residential load sector, but their application may increase in the future. In this thesis it is assumed that there are no contribution of drive-controlled single-phase IM to the residential load mix.

Refrigerators and freezers: fridge-freezers are the most common appliances that include single-phase IM. Their principle of operation involves a circulating refrigerant changing from a liquid

into a gas. This process, called evaporation, absorbs heat from within the device. To keep this cycle, the gaseous refrigerant must transform back to its liquid state, so it needs to be compressed to a higher pressure and temperature again. This is achieved by a single-phase motor acting as a compressor.

Washers and dryers: washing machines have a resistive heating element to heat the water, a motor to rotate the drum and a pump to draw water into the appliance. Dryers have a resistive heating element to heat the air and a motor to rotate the drum. Similarly, dishwashers have a resistive heating element to heat the water and a pump to draw water into the appliance.

Air conditioner and heat pump: in these devices, the compressor pressurizes a refrigerant gas and converts it back to a liquid, a similar cycle to what was described for fridge-freezers.

3.4.1.1 **EMTP model of single-phase motors**

Single-phase IM was modeled using EMTP® double-phase induction machine. This model implements and solves the equivalent circuit of a double-phase induction machine as shown in Figure 3.16.

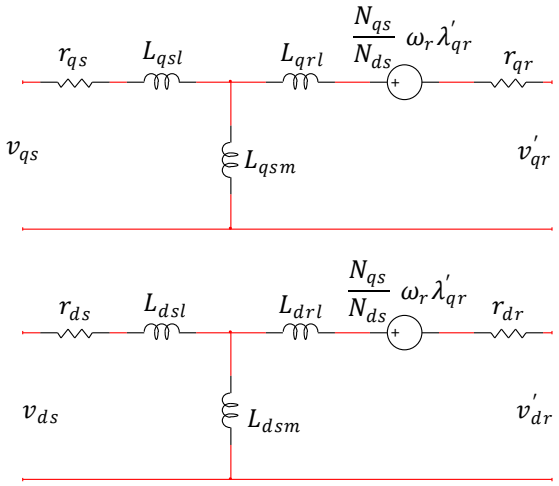

Figure 3.16 Equivalent circuit of double-phase induction machine

The equivalent stator windings are in quadrature and are denoted as the d-winding and the q-winding. As the double-phase machine is commonly used for single-phase induction motors, the q-axis winding is named “main winding” and the d-axis winding is named “auxiliary winding”. r_{qs} and r_{ds} are resistance of main and auxiliary stator coil, r_{qr} and r_{dr} are main and auxiliary rotor

resistance, L_{qs} and L_{ds} are main and auxiliary stator leakage inductance, L_{qr} and L_{dr} main and auxiliary rotor leakage inductance, L_{qsm} and L_{dsm} are q-axis and d-axis magnetizing inductance, N_{ds} and N_{qs} are main and auxiliary winding turn, λ'_{qr} and λ'_{dr} are main and auxiliary rotor flux linkage referred to the stator, ω_r is the electrical speed.

The data requirements for this model are:

1. Main data including total rated power of the machine, power factor, rated voltage, frequency and winding turn ratio between main and auxiliary windings.

2. Electrical data including stator and rotor resistance and leakage inductance (main and auxiliary winding) and d-axis and q-axis magnetizing inductance.

3. Mechanical data including the moment of inertia (or inertia constant).

In this thesis, electrical parameters exclusive to each application were used as summarized in Table 3.4 [7]. For each appliance, the presented set of parameters were used as input values for the main winding variables, and the auxiliary winding was disabled. Regarding the different types of mechanical loading conditions corresponding to motors used in different applications, some disagreement can be seen between the available information in literature. While [54] has considered refrigerator motors as CT, [53] has referred to them QT. While washers, dish washers and dryers are considered as QT in [53], the same motors are presented as CT in [54]. This disagreement is further investigated in section 4.5.4.1.

Table 3.4 Single-phase IM motor parameters

Type	$\boldsymbol{R_s}$ $(\boldsymbol{pu})$	$\boldsymbol{X_s}$ $(\boldsymbol{pu})$	$\boldsymbol{X_m}$ $(\boldsymbol{pu})$	$\boldsymbol{R_r}$ $(\boldsymbol{pu})$	$\boldsymbol{X_r}$ $(\boldsymbol{pu})$	$\boldsymbol{H}$	**Load factor**
Refrigerator	0.056	0.087	2.4	0.053	0.082	0.28	0.5
Dish washer	0.11	0.14	2.8	0.11	0.056	0.28	0.5
Cloth washer	0.11	0.12	2	0.11	0.13	1.5	0.4
Dryer	0.12	0.15	1.9	0.13	0.14	1.3	0.4
Heat pump	0.033	0.067	2.4	0.048	0.062	0.28	0.6
Air conditioner	0.1	0.1	1.8	0.09	0.06	0.28	0.6

where $\boldsymbol{R_s}$ and $\boldsymbol{X_s}$ are stator resistance and reactance, $\boldsymbol{R_r}$ and $\boldsymbol{X_r}$ are rotor resistance and reactance, respectively. $\boldsymbol{X_m}$ is magnetizing reactance and $\boldsymbol{H}$ is motor inertia constant.

3.4.2 Three-phase induction motors

Three phase IMs are used in a wide variety of applications in different load sectors especially commercial and industrial. Examples are compressors, which are commonly found in commercial air conditioning, fans commonly used in commercial ventilation and air-handling systems, and pumps used for water circulation.

3.4.2.1 **EMTP model of three-phase induction motors**

Three-phase IM was modeled using existing asynchronous machine model of EMTP®. This model implements and solves the equivalent circuit of a three-phase induction machine as shown in Figure 3.17 for a double cage rotor. The electromagnetic circuit structures of both the stator and the rotor are symmetric for most induction machines. Therefore, the equivalent circuit is only shown for d-axis.

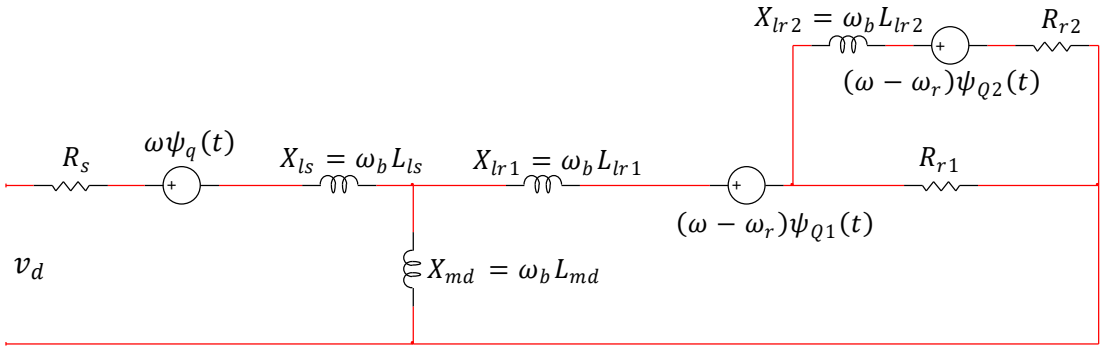

Figure 3.17 Equivalent circuit of three-phase induction machine

v_d is d-axis stator voltage, R_s is stator resistance, ω is reference frame speed, $\psi_q(t)$ is stator flux linkage, ω_b is base electrical speed, L_{ls} is stator leakage inductance, L_{md} is d-axis linkage inductance, L_{r1} is rotor leakage inductance, ω_r is electrical speed, $\psi_{Q1}(t)$ is rotor flux linkage, R_{r1} is rotor resistance, R_{r2} is rotor resistance of the second cage, L_{r2} is rotor leakage inductance of the second cage, $\psi_{Q2}(t)$ is second cage rotor flux linkage.

The data requirements for this model are:

1. Main data including total rated power of the machine, power factor, rated voltage, frequency and number of poles.

2. Electrical data including stator and rotor (single or double cage) resistance and leakage inductance, d-axis and q-axis magnetizing inductance.

3. Mechanical data including the moment of inertia (or inertia constant).

Single-cage or double-cage models of IM reflect different torque-speed characteristics. Figure 3.18 compares the single-cage and double-cage model behavior of an IM with the same nameplate ratings (output power, maximum torque, and full load speed), refer to "*DoubleCage_vs_SingleCage*" EMTP file . The difference in results can be observed, as well as the higher starting torque of the double-cage structure. This is because a single-cage rotor creates a low starting torque due to the low rotor resistance of the cage. On the other hand, in a double-cage model, the first cage has a dominant resistance under high slip conditions that helps generate the higher starting torque. This effect in combination with the second cage that has low resistance under low slip conditions, creates an accurate torque-speed profile. Reference [78] has shown that double-cage model better predicts starting current and torque manufacturer data. Therefore, the double-cage modeling is adopted in this thesis. It should be noted that modeling motors with deep bar design (NEMA A and NEMA B) [11] is not included in this thesis.

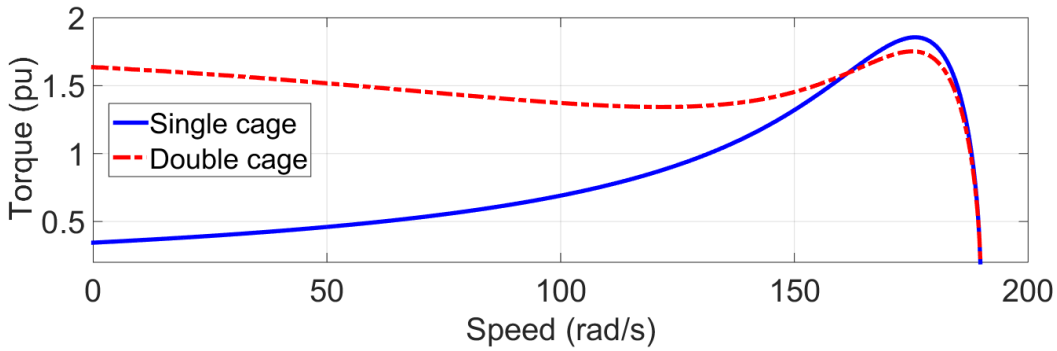

Figure 3.18 IM torque-speed characteristics modeled with single-cage and double cage rotor structure

In this thesis, electrical parameters exclusive to each application were used as summarized in Table 3.5 [11]. Regarding the different types of mechanical loading conditions corresponding to different motors, compressor and elevator motors are in the CT category while fans and pumps have QT loading characteristics [77]. It should be noted that older elevator motors typically have single-cage design.

Table 3.5 Three-phase IM motor parameters

Type	R_s (pu)	X_s (pu)	L_M (pu)	R_{r1} (pu)	X_{r1} (pu)	R_{r2} (pu)	X_{r2} (pu)	Load factor
Compressor	0.04	0.07	1.73	0.05	0.07	0.12	0.03	0.6
Fan	0.03	0.1	1.7	0.02	0.1	0.13	0.04	0.6
Pump	0.03	0.1	1.7	0.02	0.1	0.13	0.04	0.6
Elevator	0.04	0.04	2.1	0.02	0.13	0.07	0.04	0.6

3.5 Variable frequency drives of three-phase induction motors

Motors directly connected to the supply system exhibit high starting currents and low power factors and have limited speed and torque control. Variable speed drives (VFD) are used to overcome these issues and provide more sophisticated control. This section discusses three-phase IM drive circuits.

3.5.1 VFD topology

Figure 3.19 shows the configuration of the most common type of VFD which includes the pulse-width modulation (PWM) controlled voltage source inverter (VSI). The ac supply voltage is rectified by a full-bridge diode rectifier and smoothed by a dc-link capacitor. The three-phase inverter (consisting of switching IGBTs) converts the dc-link voltage to an ac voltage of desired frequency and magnitude. Another type of variable frequency drive configuration is thyristor-based load commuted VFD which is mostly used in the industry and is not discussed in this thesis. Depending on the inverter control strategy, different types of VFD can be established. Control strategies are grouped into two main categories namely scalar-based approach and vector-based approach as summarized in Figure 3.20 [28], [79] . These two categories are explained in the following section.

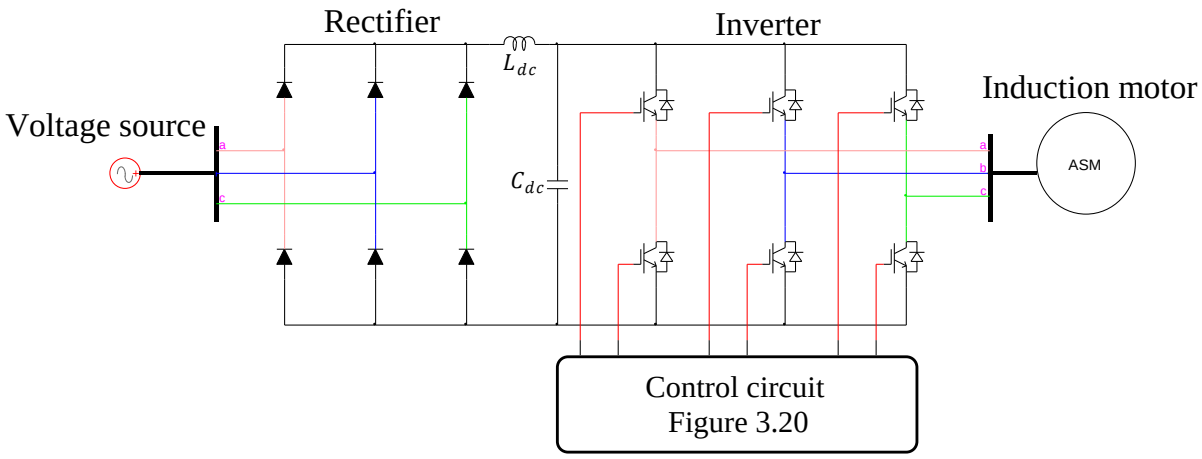

Figure 3.19 VFD circuit topology

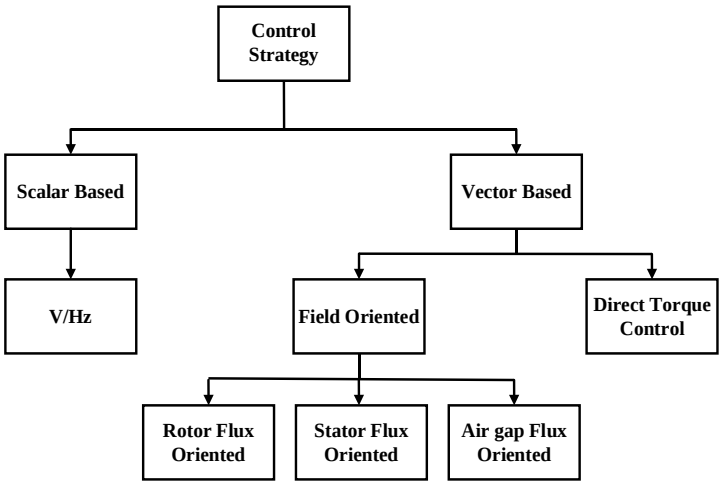

Figure 3.20 Types of VFD control

3.5.2 Scalar-based control

The simplest and least expensive control strategy is constant volt-per-hertz (V/Hz). The general concept is that around synchronous speed, the electrical rotor speed will be near the electrical frequency. So, by controlling the frequency, speed can be approximately controlled. Furthermore, in order to maintain constant flux linkage (to avoid saturation), the stator voltage magnitude should be proportional to frequency. This can be explained using the voltage equation expressed as (for phase a):

$$v_{as} = r_s i_{as} + p\lambda_{as} \tag{3.7}$$

where v_{as}, i_{as}, r_s, λ_{as} are stator voltage, current, resistance and flux linkage respectively. For steady-state conditions at mid to high speeds, the flux linkage term dominates the resistive term. So, the magnitude of the applied voltage is proportional to the magnitude of the stator flux linkage. By keeping the ratio of stator voltage magnitude and frequency constant, fairly accurate control of motor speed can be achieved. Reference [28] gives a detailed description of the theory behind and implementation of V/Hz control. In this thesis, the vector control method is employed as explained in the next section.

3.5.3 Vector control

When maximum performance and the ability to control over a wide speed range is required, vector control methods are used. Unlike the scalar control method which is based upon the steady-state model of the machine, in vector control method the dynamic machine model is used. Several vector control methods have been developed among which the field-oriented control (FOC) and direct torque control (DTC) have become the industrial standards and are widely used in drive applications. Since the rotor flux orientation is extensively used in ac drives, this scheme is used in this thesis and will be analyzed in detail. Discussions of the other types is available in [28] and [80].

3.5.3.1 **Rotor flux-oriented control**

The basic principle of FOC is to decouple the torque-producing and flux-producing components of stator current such that the torque and magnetic flux of the IM can be controlled independently. This is obtained using a proper field orientation in which the stator current can be decomposed into a flux-producing component and a torque-producing component. FOC can be generally classified into stator flux, air-gap flux, and rotor flux orientations [81]. In this thesis, the rotor flux orientation is employed.

Throughout this section, *v, i, R, L,* λ and ω are the voltage, current, resistance, inductance, flux, and angular frequency variables, respectively. Subscripts *m* and *l* denote the magnetizing and leakage inductance, respectively. The *s* subscript denotes variables and parameters associated with

the stator circuit, and the *r* subscript denotes variables and parameters associated with the rotor circuit. Subscripts *d* and *q* represents the d-axis and q-axis components. *P* is number of motor pole pairs.

The rotor flux orientation is achieved by aligning the d-axis of a synchronous reference frame with the rotor flux vector. Hence, the resultant dq-axis rotor flux components are:

$$\lambda_{qr} = 0 \text{ and } \lambda_{dr} = \lambda_r \tag{3.8}$$

The electromagnetic torque of an IM can be expressed using (3.9) [28].

$$\tau_e = \frac{3PL_m}{2L_r}(i_{qs}\lambda_{dr} - i_{ds}\lambda_{qr}) \tag{3.9}$$

Substituting (3.8) into (3.9) yields the torque expression with the rotor field orientation:

$$\tau_e = \frac{3PL_m}{2L_r} i_{qs}\lambda_{dr} = \frac{3PL_m}{2L_r} i_{qs}\lambda_r \tag{3.10}$$

Equation (3.10) indicates that by keeping λ_r constant, the torque can be independently controlled by the q-axis stator current.

One of the main aspects of the rotor field-oriented control is to determine the rotor flux angle to align the d-axis. By using this angle, the stator current vector is resolved into two perpendicular components. The d-axis current is the flux-producing component while the q-axis current, is the torque-producing component. Methods of finding the rotor flux angle classify the FOC into two categories: direct and indirect. If the rotor flux angle is obtained by using flux-sensing devices that are placed inside the airgap, the method is referred to as direct FOC. Indirect FOC (IFOC) on the other hand, does not require direct sensing of the rotor flux linkages and is more sensitive to knowledge of the machine parameters. The focus of this thesis is on indirect FOC since it is more practical for not requiring the airgap flux sensors. A general block diagram of a drive circuit with IFOC control is shown in Figure 3.21 and is described below.

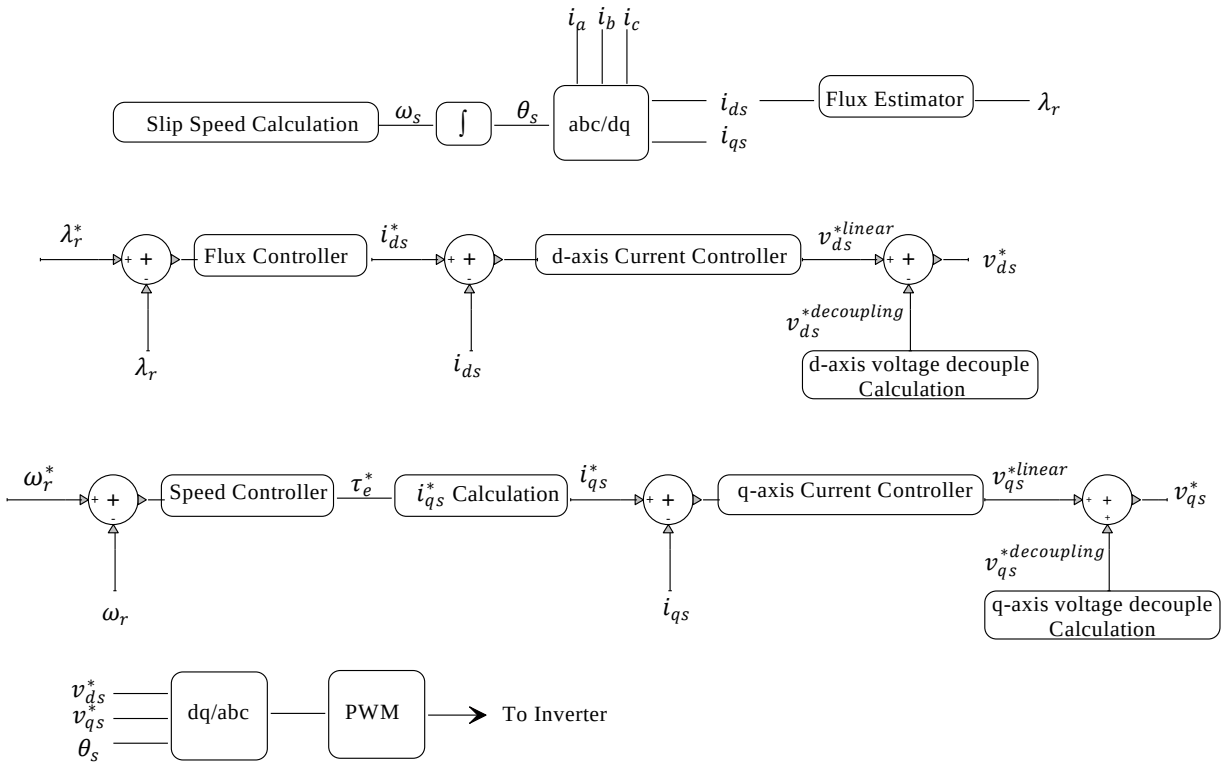

Figure 3.21 Block diagram of IFOC control

Dynamic equations of IM

Voltage equations of the IM in the d/q reference frame can be represented by (3.11) [28].

$$\begin{bmatrix} v_{qs} \\ v_{ds} \\ v_{qr} \\ v_{dr} \end{bmatrix} = \begin{bmatrix} R_s + L_s\frac{d}{dt} & \omega_e L_s & L_m\frac{d}{dt} & \omega_e L_m \\ -\omega_e L_s & R_s + L_s\frac{d}{dt} & -\omega_e L_m & L_m\frac{d}{dt} \\ L_m\frac{d}{dt} & (\omega_e - \omega_r)L_m & R_r + L_r\frac{d}{dt} & (\omega_e - \omega_r)L_r \\ -(\omega_e - \omega_r) & L_m\frac{d}{dt} & -(\omega_e - \omega_r)L_r & R_r + L_r\frac{d}{dt} \end{bmatrix} \begin{bmatrix} i_{qs} \\ i_{ds} \\ i_{qr} \\ i_{dr} \end{bmatrix} \tag{3.11}$$

The rotor flux linkage equations are as (3.12):

$$\lambda_{qr} = L_{lr} i_{qr} + L_m(i_{qs} + i_{qr}) = L_r i_{qr} + L_m i_{qs} \tag{3.12}$$
$$\lambda_{dr} = L_{lr} i_{dr} + L_m(i_{ds} + i_{dr}) = L_r i_{dr} + L_m i_{ds}$$

These set of equations will be used throughout this section. Using (3.12), equations of (3.11) can be rewritten as following sets of equations:

$$\begin{bmatrix} \frac{i_{ds}}{dt} \\ \frac{i_{qs}}{dt} \\ \frac{\psi_{dr}}{dt} \\ \frac{\psi_{qr}}{dt} \end{bmatrix} = \begin{bmatrix} \frac{-R_s}{\sigma L_s} - \frac{{L_m}^2}{\sigma L_s L_r \tau_r} & \omega_e & \frac{L_m}{\sigma L_s L_r \tau_r} & \frac{L_m \omega_r}{\sigma L_s L_r \tau_r} \\ -\omega_e & \frac{-R_s}{\sigma L_s} - \frac{{L_m}^2}{\sigma L_s L_r \tau_r} & \frac{-L_m \omega_r}{\sigma L_s L_r \tau_r} & \frac{L_m}{\sigma L_s L_r \tau_r} \\ \frac{L_m}{\tau_r} & 0 & \frac{-1}{\tau_r} & (\omega_e - \omega_r) L_r \\ 0 & \frac{L_m}{\tau_r} & -(\omega_e - \omega_r) L_r & \frac{-1}{\tau_r} \end{bmatrix} \begin{bmatrix} i_{ds} \\ i_{qs} \\ \psi_{dr} \\ \psi_{qr} \end{bmatrix} + \begin{bmatrix} \frac{1}{\sigma L_s} & 0 & 0 & 0 \\ 0 & 0 & 0 & \frac{1}{\sigma L_s} \\ 0 & 0 & 0 & 0 \\ 0 & 0 & 0 & 0 \end{bmatrix} \begin{bmatrix} v_{ds} \\ v_{qs} \\ v_{dr} \\ v_{qr} \end{bmatrix} \tag{3.13}$$

where $\tau_r = \frac{L_r}{R_r}$ is rotor time constant and $\sigma = 1 - \frac{L_m^2}{L_s L_r}$ is total leakage factor.

Rotor flux angle

Knowledge of the rotor flux space vector position is vital for IFOC. Using this space vector position, the rotational reference frame can be established as shown in the abc/dq transformation block of Figure 3.21. θ_s can be identified by integrating the sum of the slip speed and rotor speed:

$$\theta_s = \int (\omega_r + \omega_{sl}) dt \tag{3.14}$$

where ω_{sl} is the slip speed.

Slip speed calculation

ω_{sl} can be derived from the third equation of (3.13) as shown separately in (3.15).

$$\frac{d\lambda_{qr}}{dt} + \frac{L_r}{R_r}\lambda_{qr} - \frac{L_m}{L_r}R_r i_{qs} + (\omega_e - \omega_r)\lambda_{dr} = 0 \tag{3.15}$$

By taking into account the rotor flux orientation concept ($\frac{d\lambda_{qr}}{dt} = 0$ and $\lambda_{qr} = 0$) (3.15) can be simplified to (3.16) which yields the required slip speed.

$$\omega_e - \omega_r = \omega_{sl} = \frac{L_m}{\lambda_{dr}}\frac{R_r}{L_r}i_{qs} \tag{3.16}$$

Decoupled control of flux and torque

As previously mentioned, the essence of the FOC is the decoupled control of flux-producing (i_{ds}) and torque-producing (i_{qs}) components of stator current.

The d-axis stator current reference i_{ds}^* is generated by comparing λ_r with its reference value λ_r^* through the flux controller. When the motor operates at or below its rated speed, the rotor flux reference λ_r^* is normally kept at its rated value. λ_r can be calculated using the last equation of (3.13) as shown separately in (3.17).

$$\frac{d\lambda_{dr}}{dt} + \frac{R_r}{L_r}\lambda_{dr} - \frac{L_m}{L_r}R_r i_{ds} + (\omega_e - \omega_r)\lambda_{qr} = 0 \tag{3.17}$$

Since $\lambda_{qr} = 0$, the previous equation can be simplified as (3.18) which yields λ_r with respect to i_{ds} . This equation is evaluated in the flux estimator block in Figure 3.21.

$$\lambda_r = \frac{L_m i_{ds}}{1 + \tau_r \frac{d}{dt}} \tag{3.18}$$

To find the q-axis stator current reference i_{qs}^*, first the torque reference τ_e^* is generated from the speed controller by comparing the reference speed ω_r^* and the measured rotor speed ω_r. i_{qs}^* is then

derived from the torque equation (3.10). This is evaluated in the i_{qs}^{*} calculation block in Figure 3.21.

In the next step, i_{ds} and i_{ds} must be compared with their reference values in order to generate stator voltage references v_{ds}^{*} and v_{qs}^{*}.The relationship between the voltages and currents are the two first equations of (3.13). However, those equations are coupled, which means v_{ds} also depends on i_{sq}, and v_{qs} also depends on i_{sd}. To independently control the stator current components, stator voltage equations should be decoupled. To this end, voltage equations in (3.13) can be reformulated and separated into two components: linear and decoupling components:

$$v_{ds} = v_{ds}^{linear} + v_{ds}^{decoupling} \tag{3.19}$$

$$v_{qs} = v_{qs}^{linear} + v_{qs}^{decoupling}$$

Linear components are the outputs of the current controllers (see Figure 3.21, d-axis and q-axis current controllers), and are added to the voltage decoupling components:

$$v_{ds}^{decoupling} = \omega_s \sigma L_s i_{qs} + \frac{L_m}{T_r L_r}\psi_{dr} \tag{3.20}$$

$$v_{qs}^{decoupling} = \omega_s \sigma L_s i_{ds} + \frac{\omega_r L_m}{L_r}\psi_{dr}$$

Finally, v_{ds}^{*} and v_{qs}^{*} are transformed back to the three-phase stator voltages v_{as}^{*}, v_{bs}^{*}, v_{cs}^{*} in the stationary frame, see the dq to abc transformation block of Figure 3.21. Subsequently, in a PWM schemes, v_{as}^{*}, v_{bs}^{*}, v_{cs}^{*} are compared with a triangular carrier wave to generate gating signals for the switching devices in the inverter.

3.5.4 EMTP model of VFD

The model of the VFD was developed in EMTP, based on the circuit of Figure 3.19 and control circuit of Figure 3.21. The EMTP schematic of the VFD is shown in Figure 3.22 (refer to *"VFD"* EMTP file). In this figure, "IFOC circuit" block includes the implementation of the vector control as described in the previous section and depicted in Figure 3.21. To validate this model, results of simulations were compared with those produced by an existing built-in Simulink drive model [82].

The controlled IM in this model is a 50 HP, 460 V, four-pole, 60 Hz motor having the following parameters:

Table 3.6 Motor parameter related to comparison of VFD models in EMTP and Simulink

R_s (Ω)	L_{ls} (mH)	L_m (mH)	R_r (Ω)	L_{lr} (mH)	J $(kg.m^2)$
0.087	0.8	34.7	0.228	0.8	1.662

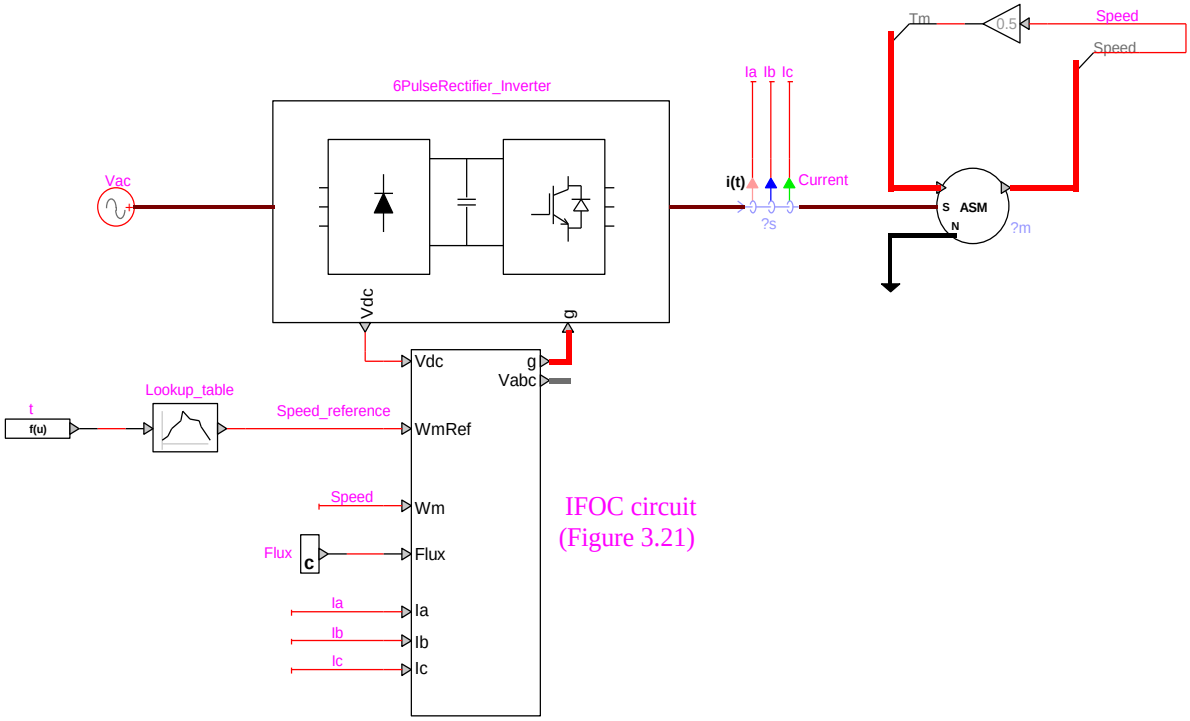

Figure 3.22 EMTP equivalent circuit of VFD model

The same motor parameters were also applied to the developed model. A linear mechanical torque was applied to both motors and the reference speed was set to a desired value of 120 rad/s. The results of the comparison between these two models are shown in Figure 3.23 to Figure 3.25. Furthermore, Figure 3.26 shows the performance of the drive model when there is a step change in the reference speed. At t=2 s, the reference speed jumps from its initial value of 120 rad/s to 160 rad/s. The EMTP® and Simulink models match each other well with respect to rotor speed and stator input current. This verifies the developed VFD model.

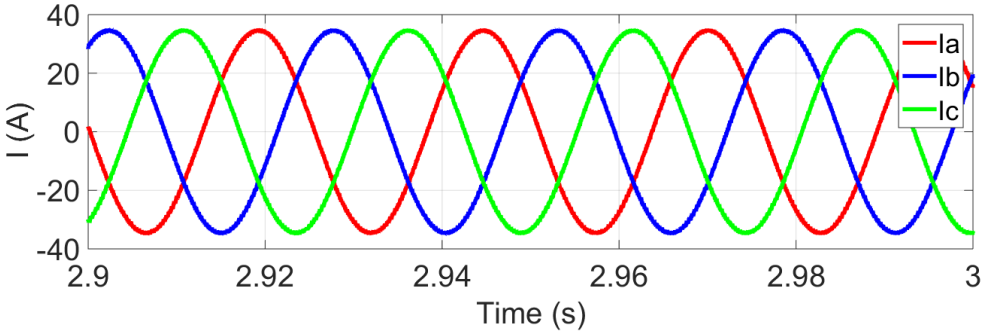

Figure 3.23 Stator currents of developed VFD model in EMTP

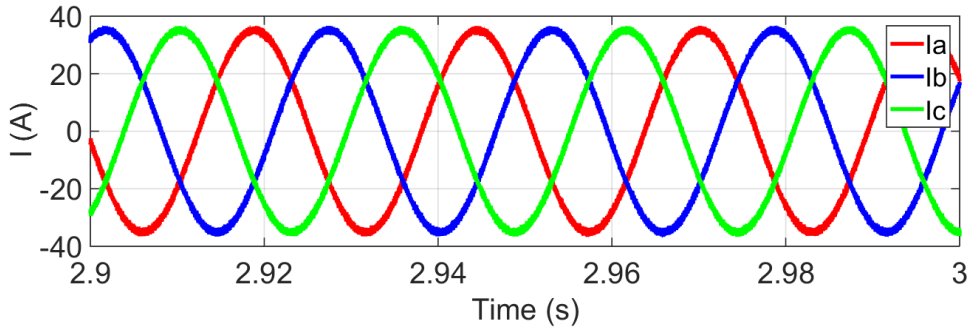

Figure 3.24 Stator currents of Simulink VFD model

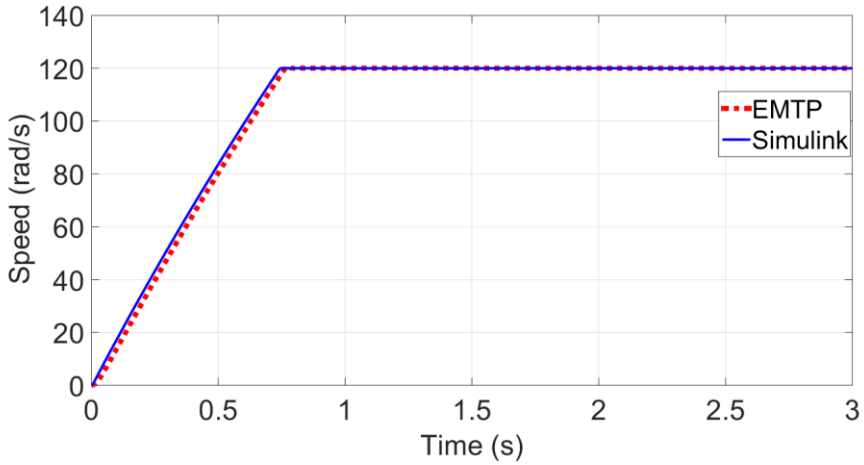

Figure 3.25 Rotor speed comparison between EMTP and Simulink models of VFD

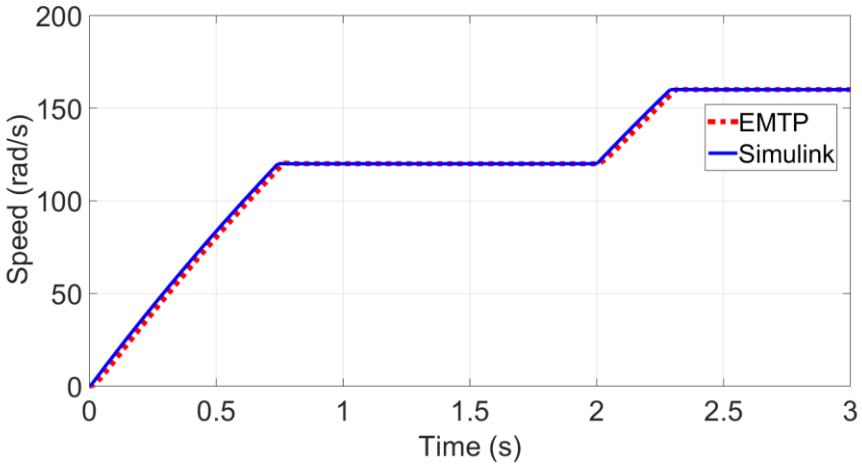

Figure 3.26 Rotor speed comparison between EMTP and Simulink models for VFD, reference speed change from 120 rad/s to 160 rad/s at t=2s

3.6 Summary

This chapter has focused on modelling different load components including resistive loads, switch-mode power supplies, light sources, single-phase and three-phase directly connected induction motors and drive-controlled three-phase induction. Description of circuit topologies and principles of operation is presented for each category followed by circuit-based model implementation in EMTP. Now that the models of load components have been developed, they will be used in a component-based procedure in the next chapter to form mixed-type aggregate loads.

CHAPTER 4 AGGREGATED DETAILED LOAD MODEL

Following the overview of the models of individual load components in Chapter 3, those components are intended for use in a component-based procedure to form the new aggregate load model, which is described in this chapter. This new EMT-type component-based model is capable of accounting for nonlinearities (i.e., power electronics), single-phase loads (e.g., single-phase motors) and unbalanced conditions (i.e., asymmetrical faults). First, the adopted component-based approach and its requirements are described. Next, load model development and implementation in EMTP® are discussed. The static characteristics of the model are validated by converting it to the form which is of most practical use, the exponential model. Importance of the detailed model to capture load behaviour in dynamic simulations is introduced. This chapter further aims to illustrate some of the applications of the developed model in predicting load behaviour in different load sectors, highlighting its flexibility and versatility. For this purpose, the model is used in range of case studies to simulate load behavior in voltage sag events, and its performance is validated against field data recorded during those events.

4.1 Component-based aggregation procedure

The adopted component-based aggregation methodology as described in section 2.5.2 and schematized in Figure 2.9, is broken down into three main steps.

In the first step, a high-level breakdown of the system loads is performed in order to identify load sectors. Load sectors, also known as classes of customers, represent customers with similar performed tasks and activities. This similarity results in typical electrical characteristics and composition of devices found in a specific load sector which in turn allows the use of similar load models for the representation of that sector. In technical literature [44], [52], [83] system loads are generally divided into three different load sectors: residential, commercial and industrial. The residential load sector is defined as houses or buildings for dwellings. The commercial load sector consists of establishments and businesses, whose purpose is to provide a specific service. Industrial sector includes product manufacturing, material processing and fabrication or similar activities. In this thesis the same three load sectors are considered.

In the second step, three sets of data must be identified to fully represent each load sector: load demand profiles, load categories and components, and the load mix (i.e., percentage contribution of each component to the total demand), from either measured or estimated load shapes and end-use profiles.

- Information on load demand profiles, which demonstrate variations in active and reactive power demands within each load sector, can be obtained from previous reports and studies, or measurements provided by utilities and network operators [84], [85]. In the latter case, it is generally possible to obtain load demand profiles from the measured demands of LV customers using smart meters. However, such measurements are not widely implemented, and hence relative information may not currently be available. Instead, power flow recordings are widely available in power systems which are recorded at higher voltage levels and therefore include information on demand profiles of mix of load sectors.
- Sources of load composition also include research documents and end-use statistics [86], [87]. Moreover, references [44] and [52] have presented an alternative way for determining load composition in which a voltage drop scenario is created using the onload tap changing transformer (OLTC), and the active and reactive power responses are measured. The aggregate load response is then decomposed based on the typical responses of different load components within the load. As another method, reference [88], has analyzed the current waveform to identify the composition. In this thesis, information in the literature (where available) is used to find load demand and load composition. Where precise information is not available, estimations are made to come up with the best approximation of load demand and composition.
- As previously discussed in Chapter 3, major types of electrical equipment found in different load sectors can be divided into one of five general load categories:

  1. Resistive loads: This load category has been presented in section 3.1.

  2. SMPS: This load category (section 3.2) can include a large number of different load components such as PCs, TVs, VCR/DVD players, set-top boxes, monitors, laptops and printers. This thesis accounts for TVs and PCs as they are assumed to have the largest contribution in this load category.

3. Lighting sources: this thesis considers incandescent, CFL and LED from lighting category, see section 3.3.

4. Single-phase and three-phase directly connected (IM): different components of this category has been discussed in section 3.4.

5. Drive-controlled motors: detailed discussion of this category has been presented in section 3.5

Finally, developed models of load components of each load sector are combined to create the mixed aggregate model based on the identified load composition.

4.2 Implementation of the new aggregated load model

After presenting the component-based approach, this section focuses on implementation of the new mixed aggregated load model using this approach. “Mixed aggregated” and “aggregated” model are used interchangeably in this thesis and refer to an aggregated load model containing various load sectors. The model was developed based on the structure shown in Figure 2.9 by connecting together the EMT-type models of individual load components presented in Chapter 3. The new model is a subcircuit in EMTP® in which the component models are placed inside, and a scripted mask is created for it, see Figure 4.1. This is a hierarchical way of representation which provides high-level access to subcircuit contents and allows the creation of a user-defined model. In the mask, user-defined specifications of a desired mixed aggregate load (e.g., connected voltage, power demand, compositions, etc.) are defined and transformed into actual circuit parameter values using JavaScript coding. Inside the subcircuit, named values are entered in data fields of component circuits instead of entering numeric values. The named values are the receptacles of calculated circuit parameters in the codes. This subcircuit yields a generic and flexible EMT-type aggregate model which can be tuned to be the representative of any desired load. The subcircuit contents and the coded mask are presented in detail the following subsections to fully conceptualize the model. Due to the level of detail placed in the development process, the proposed model hereafter is referred to as the detailed model or DM.

4.2.1 Subcircuit contents

Inside the subcircuit, total load connected to a bus is resolved into three load sectors namely residential, commercial and small industrial, see dashed-line boxes in Figure 4.1. For each sector, circuit-based models of load components (presented in section 4.1 and discussed in detail in Chapter 3) are connected together. For each component model, the corresponding circuit (figure number) developed in Chapter 3 is specified. Full circuits of incandescent and SMPS in commercial load sector are illustrated as examples of the implementation. The classification of load components included in each load sector is shown in Table 4.1 based on the typical electrical devices found within its end-use application.

Table 4.1 Classification of load components in different load sectors

Load Category	**Load Component**		**Load Sector**		
			Residential	**Commercial**	**Small Industrial**
Resistive	Water/space heater		✓	✓	
	Cooking		✓	✓	
Lighting	Incandescent		✓	✓	✓
	CFL		✓	✓	✓
	LED			✓	
Power Electronics	TV		✓		
	PC		✓	✓	
Directly connected Motors	Three-phase Motor	Compressor		✓	
		Fan		✓	
		Pump		✓	
		Industrial motor			✓
	Single-phase Motor	Refrigerator	✓	✓	
		Dish Washer	✓		
		Cloth Washer	✓		
		Dryer	✓		
		Heat Pump	✓		
		AC	✓		
Drive-controlled Motors	Elevator		✓	✓	
	Fan			✓	
	Pump			✓	

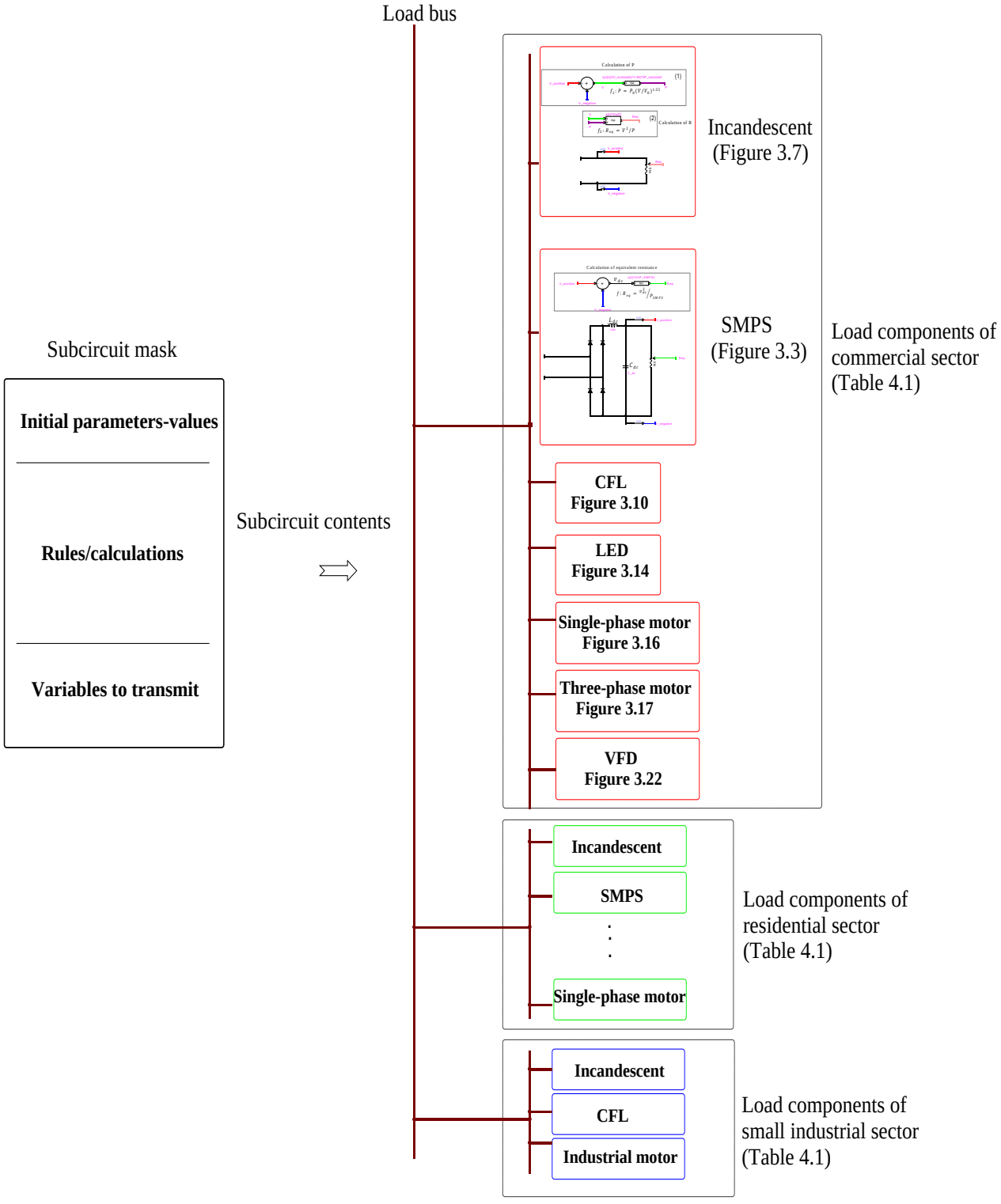

Figure 4.1 Implementation of the detailed model (DM) in EMTP, subcircuit mask and contents

As it is not practical to model large number of individual devices, each component model must represent the aggregate characteristics of same type of load. It should be noted that individual component models were given in per-unit form in Chapter 3, so are able to represent the characteristics of same-type aggregates. This allows further aggregation with other components to form the mixed aggregate load. The aggregation methodology to form same-type aggregates and ultimately a mixed aggregate load is coded in the subcircuit mask and presented in detail in the next subsection.

In addition to load components, consumer transformers are also included in each load sector. The most common representations for power transformers have been presented in [4], [15], [18], [89], [90]. In this thesis, Electra No.167 model is adopted as shown in Figure 4.2 [18]. This model represents the power transformer by a resistance R_s in series with a parallel combination of a reactance X_h and a resistance R_p. The model assumes that the leakage inductance L is constant over the range of frequencies of interest, therefore X_h increases linearly with frequency. The resistances R_s and R_P are constant at all frequencies and their values are given in Ohm as per (4.1).

$$X_1 = 2\pi f L \, , X_h = hX_1 \tag{4.1}$$

$$R_s = \frac{X_1}{\tan(\psi_1)}$$

$$R_p = 10X_1 \tan(\psi_1)$$

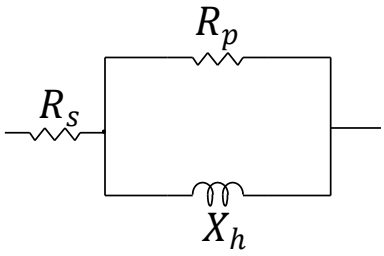

Figure 4.2 Transformer model Electra No.167 [18]

4.2.2 Subcircuit masking

After creating the subcircuit, a scripted mask is created for it to apply the aggregation methodology to the component models inside and form same-type aggregates and ultimately a mixed aggregate

load according to the percentage contribution of each component to the total demand. For this purpose, parameters of the component models inside the subcircuit are given named values. These values are first calculated in the aggregation procedure coded in the mask and then transmitted to the related subcircuit content, using three sections in this mask:

1. Initial parameters-values: for entering parameters and user-defined values. In this section, parameters listed in Table 4.2 must be given user-defined values. These are specifications of the desired load to be modeled and serve as the input parameters of the developed DM which are used in subsequent coding.

2. Rules/calculations: for developing aggregation codes.

3. Variables to transmit: for selecting the variables resulting from the codes or entered directly in initial parameters-values sections, that must be transmitted to subcircuit contents. These are the named values used in the subcircuit contents.

Table 4.2 Initial parameter-values of the DM subcircuit mask

Parameter	Description
V	Voltage level at the load bus
P_{total}	Total load power demand
$\rho_{residential}$, $\rho_{commercial}$, $\rho_{small\ industrial}$	Percentage contribution of each load sector in the total demand
$\rho_{cooking}$, $\rho_{water/space\ heater}$, , $\rho_{incandescent}$, ρ_{CFL}, ρ_{LED}, ρ_{TV}, ρ_{PC}, $\rho_{compressor}$, ρ_{fan}, ρ_{pump}, $\rho_{industrial\ motor}$, $\rho_{elevator}$, $\rho_{refrigerator}$, $\rho_{dishwasher}$, $\rho_{clothwasher}$, ρ_{dryer}, $\rho_{heat\ pump}$, ρ_{AC}	Percentage contribution of individual load components. Definition of these set of percentages are repeated for each load sector based on its composition as listed in Table 4.1. For example: $\rho_{incandescent\_residential}$ $\rho_{incandescent\_commercial}$ $\rho_{incandescent\_industrial}$
ρ'_{fan}, ρ'_{pump}	Proportion of motors controlled with a variable speed drive. Among motor loads, only fan and pump are considered both drive-controlled and directly connected. Compressors are only directly connected, and elevators are only drive-controlled. Therefore, this parameter is only defined for fan and pump.
σ_{fan}, σ_{pump}, $\sigma_{compressor}$	Percentage of directly connected motors' reactive power compensation

4.2.2.1 **Aggregation codes**

In this section, the aggregation codes provided in the mask are explained together with the named values which helps to better follow the flow of the code. The complete code is developed in three parts, each one dedicated to one load sector i.e., commercial, residential and small industrial. Each part contains the calculations for same-type aggregation of components in that sector. In the following text, operation of the code for aggregation is also explained component by component. In the actual code, the calculations for common components between load sectors are identical. However, to avoid repetition in the explanations provided below, some general terms are used and when replaced by specified expressions, components related to each load sector are characterised.

In the following text, the numbered items enclosed between two "#" characters are the named values related to each component circuit model inside the subcircuit, and the boxed area below each numbered item is its calculation steps as a part of the whole aggregation procedure. Definition of all the parameters is previously provided in Table 4.2.

Resistive load

- Subcircuit content: ideal resistor
- Variables and calculations:

1. #$R_{resistive}$# (aggregated resistance)

1.1 Aggregated power: $P_{resistive\_sector} = \rho_{sector} * \rho_{resistive\_sector} * P_{total}$; *// term "sector" can be replaced by "residential" and "commercial". Term "resistive" can be replaced by "space heater", "water heater" and "cooking"*

1.2 $R_{resistive\_sector} = \frac{V_{Low,1}^2}{P_{resistive\_sector}}$; *// $V_{Low,1}$= 0.208 $kVrms_{LL}$*

SMPS

- Subcircuit content: Figure 3.3
- Variables and calculations:

1. #P_{SMPS}# (aggregated power), see function f in Figure 3.3

$P_{SMPS\_sector} = \rho_{sector} * \rho_{SMPS\_sector} * P_{total}$; *//term "sector" can be replaced by "residential" and "commercial". Term "SMPS" can be replaced by "TV" and " PC"*

2. #C_{dc}# (aggregated dc-link capacitance)

2.1 Base impedance: $Z_{base\_sector} = \frac{V_{Low,1}^2}{P_{SMPS\_sector}}$; *// $V_{Low,1}$= 0.208 $kVrms_{LL}$*

2.2 $X_{c_{dc}}$ = 0.036 pu *Z_{base_sector} ; *//typical per-unit value of reactance, section 3.2.2*

2.3 $C_{dc\_sector} = \frac{1}{X_{c_{dc}} \cdot 2\pi f}$;

3. #L_{dc}# (aggregated dc-link inductance)

3.1 $X_{L_{dc}} = 0.03$ pu $*Z_{base\_sector}$; *//typical per-unit value of reactance, section 3.2.2*

3.2 $L_{dc\_sector} = \frac{X_{L_{dc}}}{2\pi f}$;

CFL

- Subcircuit content: Figure 3.10
- Variables and calculations:

1. #nb# (number of aggregated CFLs). This variable is added to functions f_1 and f_2 in Figure 3.10 in order to create an aggregated equivalent resistance: $R_{eq,agg} = \frac{R_{eq}}{nb}$.

1.1 Aggregated power: $P_{CFL\_sector} = \rho_{sector} * \rho_{CFL\_sector} * P_{total}$; *//term "sector" can be replaced by "residential", "commercial" and "small industrial"*

1.2 $nb\_sector = \frac{P_{CFL\_sector}}{P_{rated,CFL}}$; *//$P_{rated,CFL} = 15$ W*

2. # C_{dc}# (aggregated dc-link capacitance)

2.1 Base impedance: $Z_{base\_sector} = \frac{V_{Low,1}^2}{P_{CFL\_sector}}$; *// $V_{Low,1} = 0.208\ kVrms_{LL}$*

2.2 $X_{c_{dc}\_sector} = 0.25$ pu $*Z_{base\_sector}$; *//typical per-unit value of reactance, section 3.3.2.2*

2.3 $C_{dc\_sector} = \frac{1}{X_{c_{dc}} \cdot 2\pi f}$;

LED

- Subcircuit content: Figure 3.13
- Variables and calculations:

1. #R_{LED}# (aggregated LED module resistance)

1.1 Aggregated power: $P_{LED\_sector} = \rho_{sector} * \rho_{LED} * P_{total}$; *//term "sector" can be replaced by "commercial"*

1.2 Number of aggregated LEDs: $nb\_sector = \frac{P_{LED\_sector}}{P_{rated,LED}}$; *// $P_{rated,LED} = 30$ W*

1.3 $R_{LED\_sector} = \frac{R_{LED,single\ module}}{nb}$; *//$R_{LED,single\ module} = 1.5\ \Omega$, section 3.3.3.3*

2. #C_{dc}# (aggregated dc-link capacitance)

2.1 Base impedance: $Z_{base\_sector} = \frac{V_{Low,2}^2}{P_{LED\_sector}}$; // $V_{Low,2}$= 0.6 $kVrms_{LL}$

2.2 $X_{c_{dc}\_sector} = 0.036$ pu *Z_{base_sector} ; *//typical per-unit value of reactance, section 3.3.3.3*

2.3 $C_{dc\_sector} = \frac{1}{X_{c_{dc}\_sector} \cdot 2\pi f}$;

3. #L_{dc}# (aggregated dc-link inductance)

3.1 $X_{L_{dc}\_sector} = 0.03$ pu *Z_{base}; *//typical per-unit value of reactance, section 3.3.3.3*

3.2 $L_{dc\_sector} = \frac{X_{L_{dc}\_sector}}{2\pi f}$;

Directly connected fan and pump

- Subcircuit content: Figure 3.17
- Variables and calculations:

1. Motor electrical parameters

Per-unit values as defined in Table 3.5;

2. #Pn_{motor}# (nominal aggregated motor power)

2.1 Aggregated motor power: $P_{motor\_sector} = [\rho_{sector} * \rho_{motor} * (1 - \rho'_{motor})] * P_{total}$; *//term "sector" can be replaced by "commercial". term "motor" can be replaced by "fan" and "pump"*

2.2 $Pn_{motor\_sector} = \frac{P_{motor\_sector}}{Load\ factor}$; *//Load factor as defined in Table 3.5*

3. #$C_{compensation}$# (aggregated capacitance connected at motor terminal for reactive power compensation)

3.1 Required reactive power: $Q_{compensation\_sector} = \sigma_{motor\_sector} * Pn_{motor\_sector}$;

3.2 $C_{compensation\_sector} = \frac{Q_{compensation\_sector}}{2\pi f \cdot V_{Low,2}^2}$; // $V_{Low,2}$= 0.6 $kVrms_{LL}$

Compressor

- Subcircuit content: Figure 3.17
- Variables and calculations:

1. Motor electrical parameters

Per-unit values as defined in Table 3.5;

2. #$Pn_{compressor}$# (nominal aggregated motor power)

2.1 Aggregated motor power: $P_{compressor\_sector} = \rho_{sector} * \rho_{compressor} * P_{total}$; *//term "sector" can be replaced by "commercial"*
2.2 $Pn_{compressor\_sector} = \frac{P_{compressor\_sector}}{Load\ factor}$; *//Load factor as defined in Table 3.5*

3. #$C_{compensation}$# (aggregated capacitance connected at motor terminal for reactive power compensation)

3.1 Required reactive power: $Q_{compensation\_sector} = \sigma_{compressor\_sector} * Pn_{compressor\_sector}$;
3.2 $C_{compensation\_sector} = \frac{Q_{compensation\_sector}}{2\pi f.\ V_{Low,2}^2}$; // $V_{Low,2}$= 0.6 $kVrms_{LL}$

Industrial motor

- Subcircuit content: Figure 3.17
- Variables and calculations:

1. Motor electrical parameters

Per-unit values as defined in Table 3.5;

2. #$Pn_{motor,industrial}$# (nominal aggregated motor power)

2.1 Aggregated motor power: $P_{motor,industrial} = \rho_{sector} * \rho_{motor,industrial} * P_{total}$; *//term "sector" can be replaced by "small industrial"*
2.2 $Pn_{motor,industrial} = \frac{P_{motor,industrial}}{Load\ factor}$; *//Load factor as defined in Table 3.5*

Drive-controlled fan and pump

- Subcircuit content: Figure 3.22
- Variables and calculations:

1. Motor electrical parameters

Per-unit values as defined in Table 3.5;

2. #$Pn_{motor,drive}$# (nominal aggregated motor power)

2.1 Aggregated motor power: $P_{motor,drive} = (\rho_{sector} * \rho_{motor} * \rho'_{motor}) * P_{total}$; *//term "sector" can be replaced by "commercial". Term "motor" can be replaced by "fan" and "pump"*
2.2 $Pn_{motor,drive} = \frac{P_{motor}}{Drive\ efficiency * Load\ factor}$; *//load factor as defined in Table 3.5, efficiency = 0.92*

3. #R_{loss}# (drive losses)

$R_{loss} = \frac{V_{Low,2}^2}{Loss\ percentage * P_{motor,drive}}$; *//$V_{Low,2}$= 0.6 $kVrms_{LL}$, loss percentage= 0.08*

4. #C_{dc}# (aggregated dc-link capacitance)

4.1 Base impedance: $Z_{base} = \frac{V_{Low,2}^2}{P_{motor,drive}}$; *//$V_{Low,2}$= 0.6 $kVrms_{LL}$,*
4.2 $X_{c_{dc}}$ = 0.2 pu *Z_{base} ; *//typical per-unit value of reactance, section 3.5.4*
4.3 $C_{dc} = \frac{1}{X_{c_{dc}} \cdot 2\pi f}$;

5. #L_{dc}# (aggregated dc-link inductance)

5.1 $X_{L_{dc}}$ = 0.03 pu *Z_{base}; *//typical per-unit value of reactance, section 3.5.4*
5.2 $L_{dc} = \frac{X_{L_{dc}}}{2\pi f}$;

Elevator

- Subcircuit content: Figure 3.22
- Variables and calculations:

1. Motor electrical parameters

Per-unit values as defined in Table 3.5;

2. #$Pn_{elevator}$# (nominal aggregated motor power)

2.1 Aggregated motor power : $P_{elevator\_sector} = \rho_{sector} * \rho_{elevator} * P_{total}$; *//term "sector" can be replaced by "commercial" and "residential"*
2.2 $Pn_{elevator\_sector} = \frac{P_{elevator\_sector}}{Drive\ efficiency * Load\ factor}$; *//load factor as defined in Table 3.5, efficiency = 0.92*

3. #R_{loss}# (drive losses)

$R_{loss} = \frac{V_{Low,2}^2}{Loss\ percentage * P_{elevator\_sector}}$; *//$V_{Low,2}$= 0.6 $kVrms_{LL}$, loss percentage= 0.08*

4. #C_{dc}# (aggregated dc-link capacitance)

4.1 Base impedance: $Z_{base\_sector} = \frac{V_{Low,2}^2}{P_{elevator\_sector}}$; *//$V_{Low,2}$= 0.6 $kVrms_{LL}$*
4.2 $X_{c_{dc}\_sector}$ = 0.2 pu *Z_{base_sector} ; *//typical per-unit value of reactance, section 3.5.4*
4.3 $C_{dc\_sector} = \frac{1}{X_{c_{dc}\_sector} \cdot 2\pi f}$;

5. #L_{dc}# (aggregated dc-link inductance)

5.1 $X_{L_{dc}\_sector}$ = 0.03 pu *Z_{base_sector}; *//typical per-unit value of reactance,section 3.5.4*
5.2 $L_{dc\_sector} = \frac{X_{L_{dc}\_sector}}{2\pi f}$;

Single-phase motor

- Subcircuit content: Figure 3.16
- Variables and calculations:

1. Motor electrical parameters

Per-unit values as defined in Table 3.4;

2. #$Pn_{single-phase\ motor}$ # (nominal aggregated motor power)

2.1 $P_{single-phase\ motor} = \rho_{sector} * \rho_{single-phase\ motor} * P_{total}$; *//term "sector" can be replaced by "residential". Term "single-phase motor" can be replaced by "refrigerator", "dish washer", "cloth washer", "dryer", "heat pump "and "air conditioner"*
2.2 $Pn_{single-phase\ motor} = \frac{P_{single-phase\ motor}}{Load\ factor}$; *//load factor as defined in Table 3.4*

Transformer

- Subcircuit content: Figure 4.2
- Variables and calculations:

1. #n# (turn ratio)

1.1 Transformer T_1, fed from the main electrical entrance
$n_{T_1} = \frac{V_{2,T_1}}{V_{1,T_1}}$; *//primary voltage $V_{1,T_1} = V$, secondary voltage V_{2,T_1}=0.6 $kVrms_{LL}$*
1.2 Transformer T_2, fed from T_1
$n_{T_2} = \frac{V_{2,T_2}}{V_{1,T_2}}$; *//primary voltage $V_{1,T_2} = 0.6\ kVrms_{LL}$, secondary voltage V_{2,T_2}= 0.208 $kVrms_{LL}$*

2. #R_s, L_T, R_p # (aggregated transformer winding resistance, inductance and parallel resistance)

2.1 Nominal power: $S_{T_1} = 2.5^* S_{total}$; *//based on practical aspects, installed capacity of transformer is assumed to be 2.5 times the total load*
Base impedance: $Z_{base,T_1} = \frac{{V_{1,T_1}}^2}{S_{T_1}}$;
$R_{s,T_1} = 0.004$ pu*Z_{base,T_1}; *//typical per-unit value of winding resistance*
$X_{L,T_1} = 0.08$ pu*Z_{base,T_1}; *//typical per-unit value of winding reactance*
$L_{T_1} = \frac{X_{L,T_1}}{2\pi f}$;

$R_{p,T_1} = 10 * X_{L,T_1} * \frac{X_{L,T_1}}{R_{s,T_1}}$; *//see equation (4.1)*

2.2 Nominal power: $S_{T_2} = 1.5 * S_{total}$; *//based on practical aspects, installed capacity of transformer is assumed to be 1.5 times the total load*

Base impedance: $Z_{base,T_2} = \frac{{V_{1,T_2}}^2}{S_{T_2}}$;

$R_{s,T_2} = 0.003$ pu*Z_{base,T_2}; *//typical per-unit value of winding resistance*

$X_{L,T_2} = 0.03$ pu*Z_{base,T_2}; *//typical per-unit value of winding reactance*

$L_{T_2} = \frac{X_{L,T_2}}{2\pi f}$;

$R_{p,T_2} = 10 * X_{L,T_2} * \frac{X_{L,T_2}}{R_{s,T_2}}$; *//see equation (4.1)*

The presented scripted-masked subcircuit is a generic and flexible load model structure which can be used in any desired network and load condition. What is changed from case to case is the associated input parameter values, for example power demand at the load bus, or load composition for different time of the day or different time of the year.

4.3 Static characteristics

This section presents the exponential interpretation of the DM which illustrates its static characteristics. For this purpose, the DM of a typical mixed residential-commercial load was converted to its equivalent exponential model form which is the most widely used static model as presented in (2.1) and (2.2). This was accomplished using the simulation setup of Figure 4.3 (refer to *"DM_vs_static"* EMTP file). First, DM of a 132 kW mixed residential (80%)-commercial (20%) was formed and connected to a 120 kV source via step-down transformers to represent a typical distribution system. Next, slow voltage ramp tests were performed to determine the active and reactive power sensitivities (n_p and n_q) with respect to voltage. The "Voltage ramp" subcircuit in Figure 4.3 was developed for this purpose. In the following sections, first the DM of the mixed load is described and next the voltage ramp tests are presented.

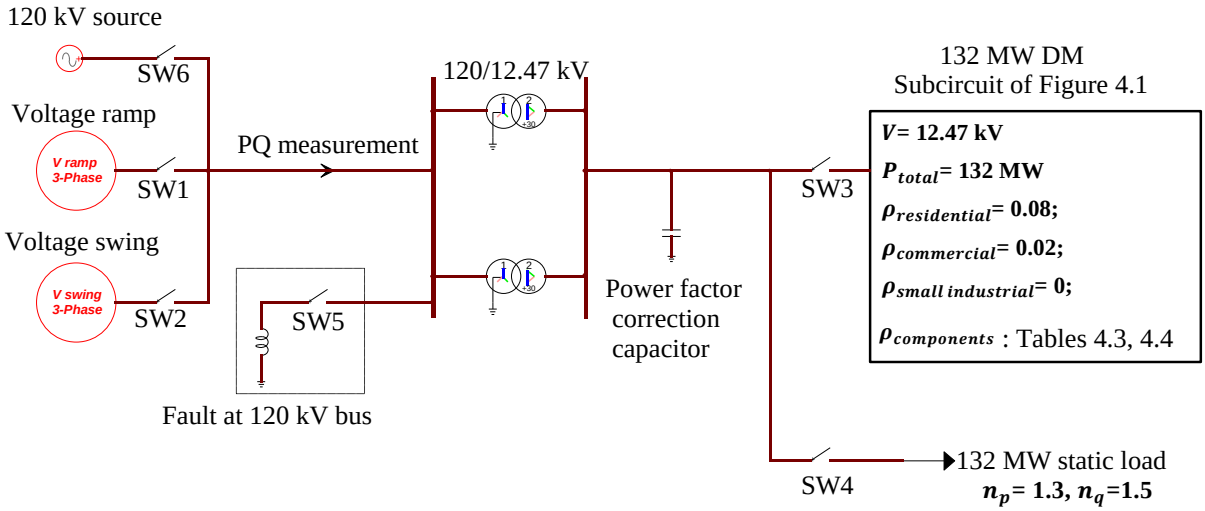

Figure 4.3 System set-up for comparison of the DM and static load model

4.3.1 Forming the DM of the residential-commercial load

Input parameters for forming the DM of the considered mixed residential-commercial load is demonstrated in Figure 4.3. Finding the information on load composition as one of the input parameters is a challenging aspect since it is different for each network and also changes with time. Undertaking customer surveys may be the best approach to obtain this data but it is quite a time consuming and expensive endeavor. It should be noted that even with such surveys it is still difficult to find an exact composition. Therefore, in this thesis, where available, information in the literature is used and where enough data are not available, estimations are made to come up with the best approximate of decomposition of load mix related to each case study. Later in this chapter, it is demonstrated that an approximate, based on realistic assumptions, load composition can reproduce the actual characteristics of the load. Table 4.3 and Table 4.4 present typical load compositions for commercial and residential sectors, one set of data for each loading condition, i.e., heavy and light load. Light load corresponds to the summer power demand, 4 a.m. in the month of August and heavy load corresponds to the winter peak load demand, 12 a.m. in the month of February. Those compositions were obtained from end-use data provided by Hydro-Quebec [87], in combination with EPRI load shape library [91]. These two tables serve as a basis for composition data in several case studies of this thesis. It should be noted that NERC Load Model Data Tool (LMDT) [11] can also be used as the source of load composition data.

Table 4.3 Residential load composition

Load Component	Composition	
	Heavy Load	Light Load
CFL	4.9%	15.4%
Incandescent	2.1%	6.6%
PC	3%	12%
TV	3%	12%
Freezer	8%	8%
Refrigerator	8%	8%
Dish washer	0%	0%
Cloth dryer	8%	8%
Cloth washer	0%	0%
Room AC	0%	16%
Heat pump	10%	0%
Heating	41%	0%
Cooking	1%	0%
Water heating	6%	13%
Elevator	5%	1%

Table 4.4 Commercial load composition

Load Component	Composition	
	Heavy Load	Light Load
Compressor	0%	18%
Pump	4%	5%
Fan	9%	21%
Elevator	8%	5%
CFL	8%	8%
Incandescent	9%	12%
LED	19%	16%
PC	4%	8%
Refrigerator	6%	5%
Heating	32%	0%
Cooking	1%	2%

4.3.2 Voltage ramp tests

The “Voltage ramp” subcircuit in Figure 4.3 was developed for performing voltage ramp test on the DM in order to find its static characteristics. Inside the subcircuit, there are three controlled voltage sources, one to apply to each phase. The structure of each voltage source is the same as Figure 3.4, so it is not repeated here. Using a look-up table as similar to Figure 3.5, the voltage was

ramped from 1 pu to 1.25 pu from t=3.5 s to t=5.5 s, and subsequently decreased to 1 pu from t=5.5 s to t=7.5 s (refer to the green voltage curves in Figure 4.4). In the circuit of Figure 4.3, switches "SW1" and "SW3" were closed to apply the voltage ramp source to the DM. Switches "SW2", "SW4", "SW5" and "SW6" were open. Two voltage ramp tests were performed for the two cases of heavy load and light load as defined in the previous section. The compositions listed in Table 4.3 and Table 4.4 were used for residential and commercial loads while forming the DM in each of the two cases. The active and reactive power demands were simulated to deduct the corresponding coefficients of the exponential model (n_p and n_q). The resulting power demands are depicted in Figure 4.4. Those curves were taken one step further and converted into trajectories of active and reactive power versus supply voltage, see Figure 4.5 and Figure 4.6. This allows for deduction of exponential model coefficients because parameters n_p and n_q can be considered as partial derivatives of real and reactive power with respect to voltage in the vicinity of rated voltage, respectively [23]. In this way, the coefficients obtained from the two curves are as following: for heavy load, n_p is about 1.3 and n_q is close to 1.5. For light load, n_p is approximately 0.9 and n_q is around 2. In a qualitative manner, n_p has a larger value during heavy load as a result of higher contribution of heating load. The higher value of n_q can be expected in light load due to higher percentage of single-phase motors which serve as the main reactive power demand in the residential load sector. The obtained coefficients are in accordance with Hydro-Quebec measured values, i.e., n_p= 1.4, n_q= 1.75 for heavy load and n_p= 1, n_q= 1.76 for light load [87]. The closeness of simulation results with measurements is an indication that the considered load compositions (Table 4.3 and Table 4.4) are sufficiently accurate. This comparison further provides the first stage of DM validation in terms of its static characteristics.

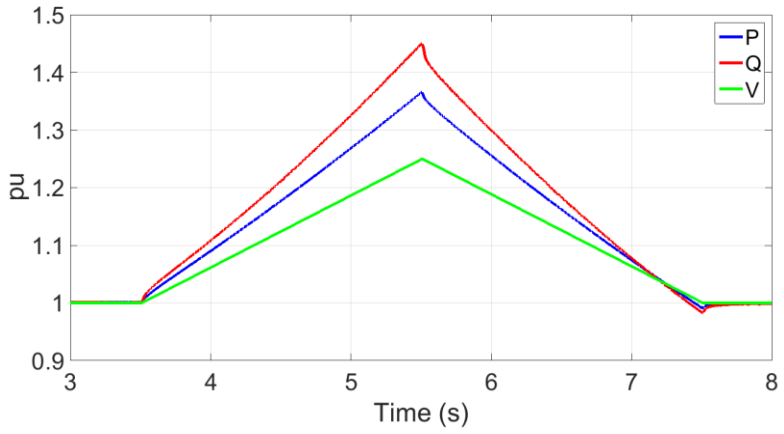

(a)

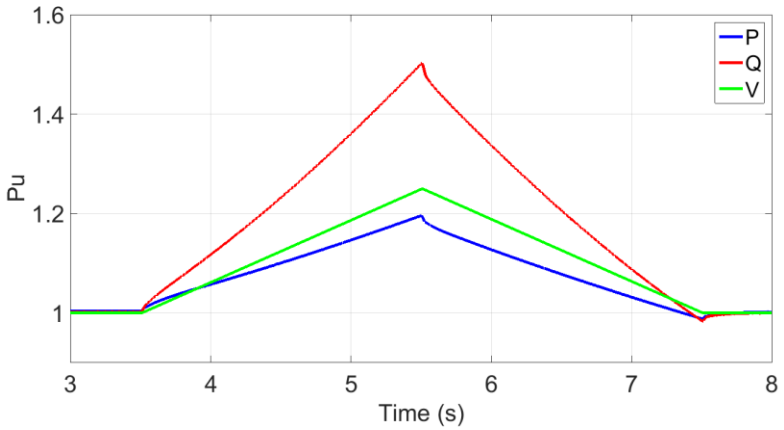

(b)

Figure 4.4 Static characteristics of the DM: (a) winter, (b) summer

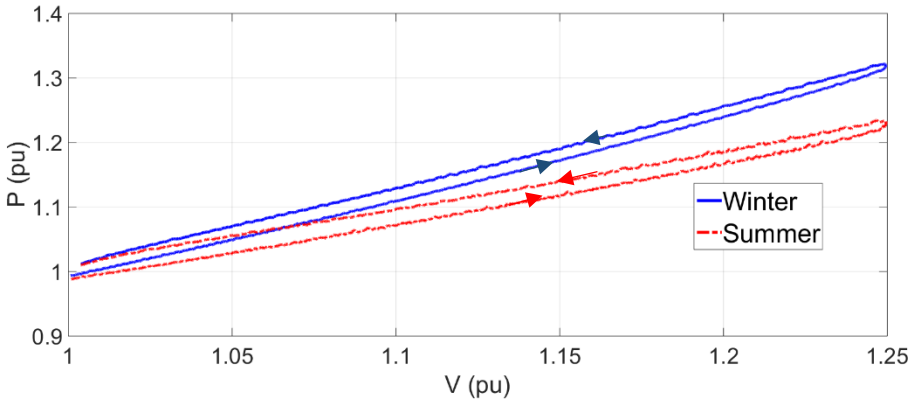

Figure 4.5 P-V characteristics of winter and summer load, modeled by DM

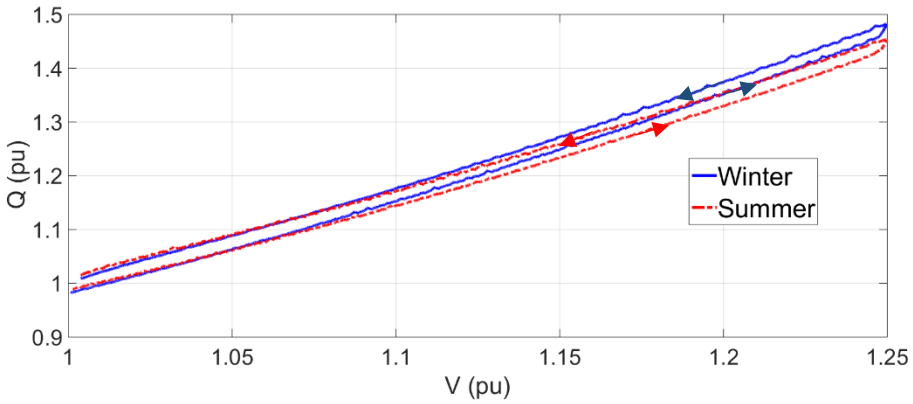

Figure 4.6 Q-V characteristics of winter and summer load, modeled by DM

4.4 Importance of the detailed load model

Static models are the current practice in most dynamic studies. Although some standards require utilities to use dynamic models [92], results of an international survey shows that only about 30% of utilities and system operators use some form of dynamic or composite model to represent loads in dynamic power system studies [93]. In this section, the performance of an exponential static model in dynamic simulations is examined. For this purpose, the developed DM was compared against its exponential equivalent (as derived in the previous section) in two different dynamic event scenarios using the simulation setup of Figure 4.3. The exponential equivalents of the DM were obtained in the previous section for two conditions of heavy and light load. One of those equivalents i.e., the heavy load condition which is an exponential model with the coefficients n_p= 1.3, n_q= 1.5, was selected for the current case study.

In the first scenario, a voltage swing test was conducted to observe and compare the behaviour of static load and DM during the power system oscillations. The test was performed by applying a voltage swing to the load. For this purpose, a subcircuit was developed to implement a voltage source with the desired swing, see Figure 4.3, "Voltage swing" block (refer to *"DM_vs_static"* EMTP file). The subcircuit mask and its contents are shown in Figure 4.7 and Figure 4.8, respectively. In the mask, the following parameters are user defined: desired line-to-line amplitude of voltage source (V_{LL}), initial phase angle of phase "a" (φ_a), frequency (f), swing amplitude (A_{swing}), swing frequency (A_{swing}), starting time of the swing (t_{swing}) and swing time constant

(α_{swing}). In the rules/calculation section, the line-to-line voltage is transformed into phase voltage (V) and initial phase angles of phase "b" and "c" are determined. All of the above parameters are transmitted into the subcircuit contents.

Inside the subcircuit (Figure 4.8), three controlled voltage sources are used, one to apply to each phase. The methodology is similar for all three phases, so the explanation in provided here only for phase "a". Before the starting time of the swing, a simple cosine wave is applied to the controlled voltage source. This is implemented starting from function f_1. For $t < t_{swing}$, the output of function f_1 is zero and therefore swing function (see sg_1) is not transferred to f_3. Output of f_3 in this case is the signal generated by sg_2. This is a cosine wave with amplitude of one, frequency f and initial angle φ_a. It is multiplied by the amplitude V and then applied to the controlled voltage source. After the starting time of the swing i.e., $t \geq t_{swing}$, the output of function f_1 is one, and therefore swing function sg_1 is transferred to f_3. It is then multiplied by sg_2 and V to produce a voltage source with the desired swing.

In this case study, the voltage source was set to 120 kV and a 1 Hz swing with the amplitude of 0.3 pu was imposed in order to reproduce typical network swings. The starting time of the swing was at t=3.5 s (after the DM reaches steady-state operating conditions). The positive sequence voltage at 120 kV bus in Figure 4.9 shows the adjusted voltage swing. In the circuit of Figure 4.3, "SW2" was closed to apply the source to the circuit. Switches "SW1", "SW5", and "SW6" were open, and switches "SW3" and "SW4" were closed one at a time. Figure 4.9 presents the comparative simulation results of active and reactive power demands. It is noticed that although the static model can approximate the active power, it cannot capture the dynamic mode of reactive power.

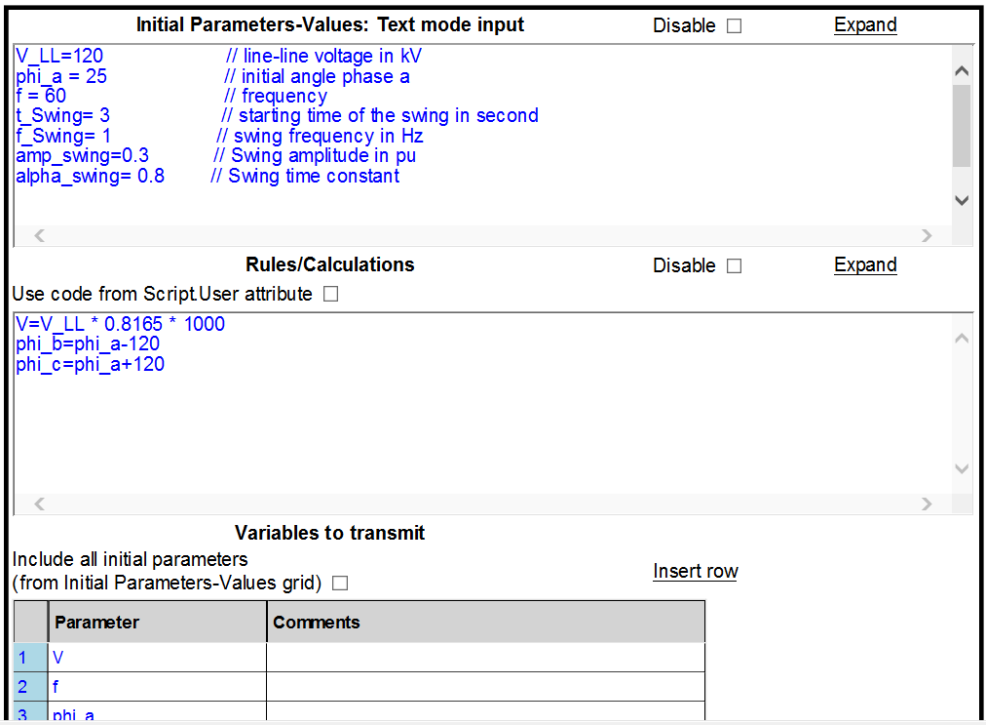

Figure 4.7 Subcircuit mask for voltage swing block in Figure 4.3

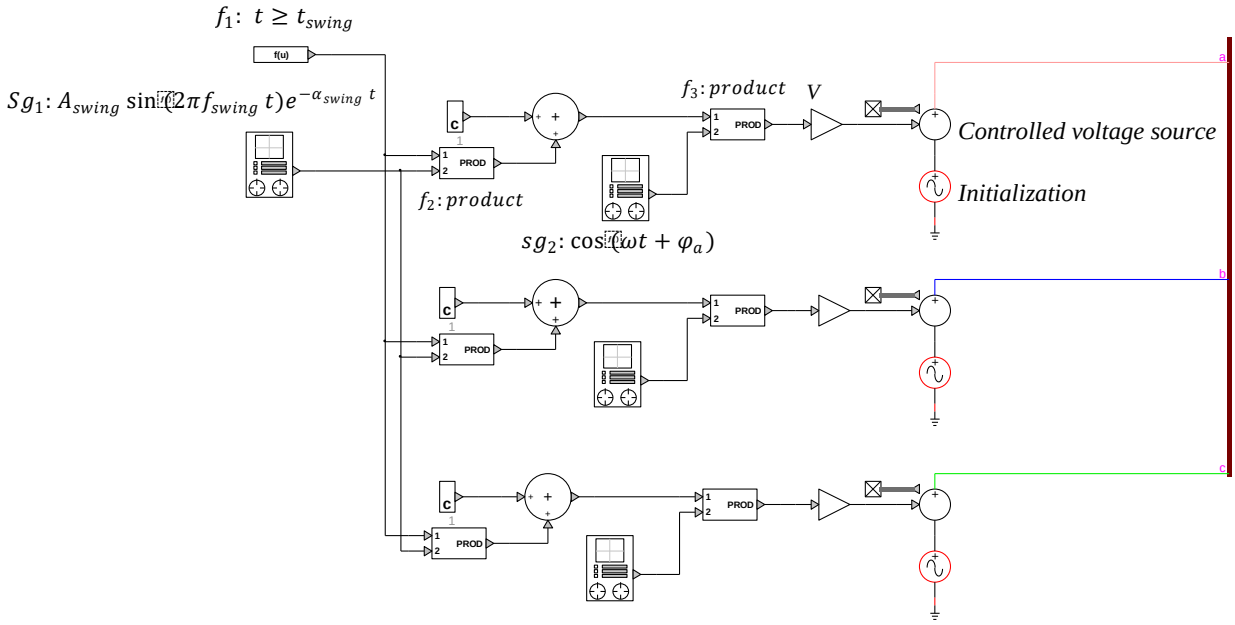

Figure 4.8 Subcircuit contents for voltage swing block in Figure 4.3

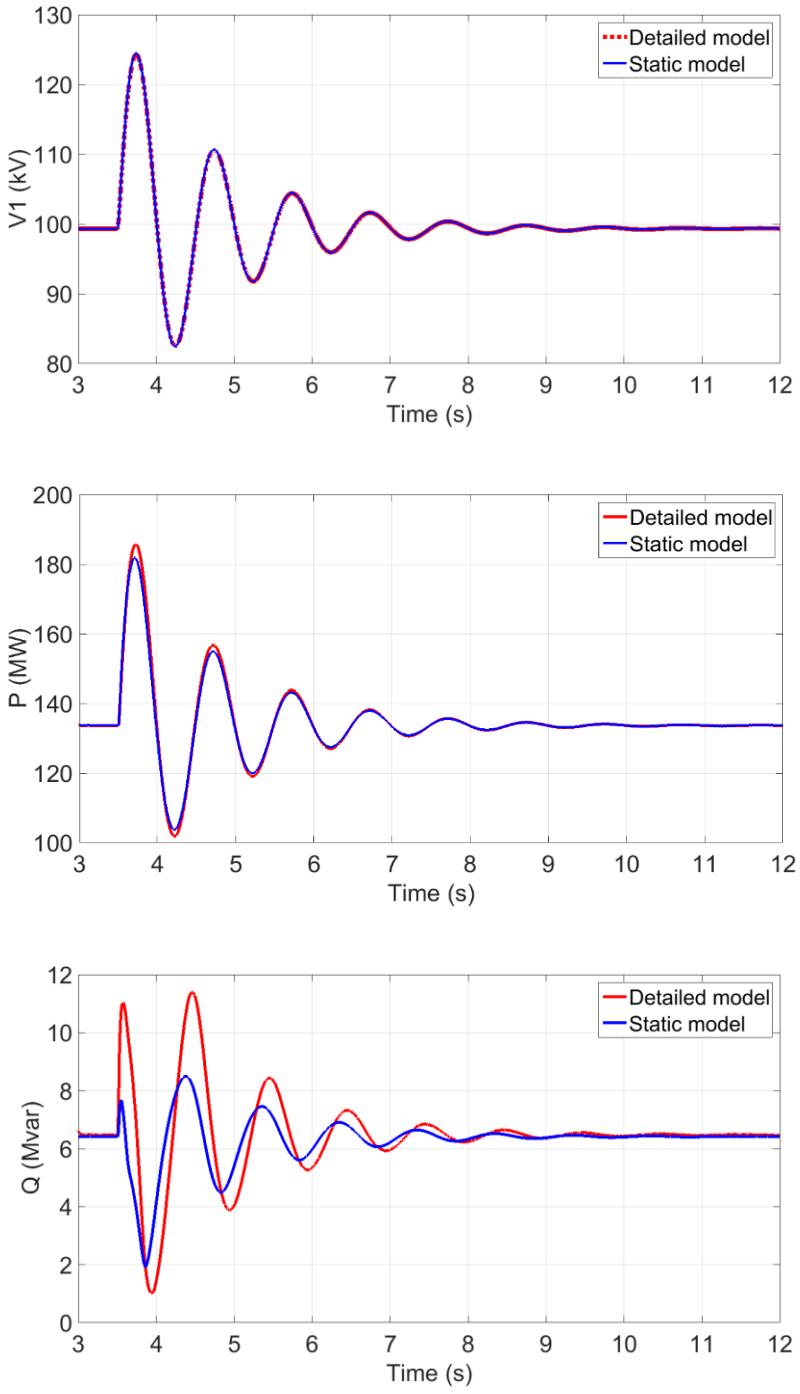

Figure 4.9 Voltage swing dynamic characteristics: positive sequence voltage, active and reactive power

In the second scenario, a three-phase fault at the 120 kV bus in Figure 4.3 was simulated and cleared after 6 cycles. Switch “SW6” was closed to apply a 120 kV source to the circuit, “SW5” was closed

between t= 3.5 s and t= 3.58 s, switches “SW1” and “SW2” were open and “SW3” and “SW4” were closed one at a time. The comparative results are presented in Figure 4.10.

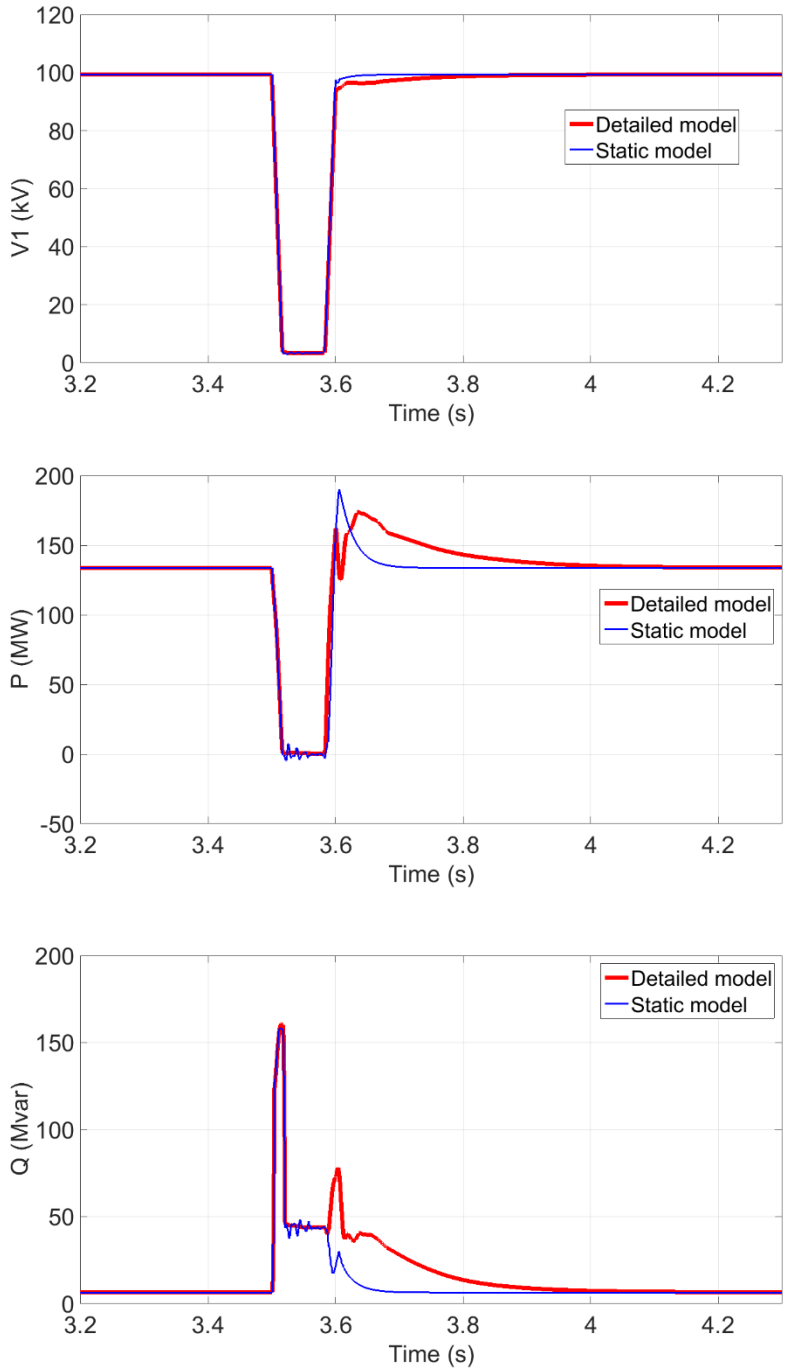

Figure 4.10 Post-fault dynamic characteristics: positive sequence voltage, active and reactive power

As shown in Figure 4.10, the static model is not capable of reproducing the reactive power demand. A noticeable difference exists at the time of fault removal t=3.58 s which is attributed to the high demand of motor loads during acceleration. When a fault occurs near induction motors, their torques and speeds are dropped below the nominal values and their internal electromagnetic force (emf) declines. After the fault is removed, motors attempt to re-establish their internal emf and reaccelerate. Therefore, they draw an excessive amount of current and hence reactive power from the supply.

Results of the two case studies clearly suggest that although static models can be utilized for steady-state analysis, they are not suitable to reproduce the dynamic behavior. The differences in results highlight the necessity to include a more accurate load model in power system studies which can realistically represent the sensitivity of loads to deviations in the grid such as those experienced during voltage swings or faults. Detailed models such as the developed model in this thesis (DM) are expected to have a larger range of validity in terms of the predicted response to voltage deviation which will be further investigated in the following sections.

4.5 Dynamic characteristics

After presenting the static characteristics of the DM and its significance in representing load dynamics, its application in dynamic events of different load sectors is presented and validated in this section. This requires the simulated response of the load to be compared to the actual observed dynamic behaviors. This is one of the most challenging aspects of load modeling as it would require a large number of measurements performed on specific points of the power system where the network and load configurations are relatively well known. If event recordings for faults at those points in the system are available, then by comparing the actual recordings to the simulated response, one can obtain an understanding of the performance of the load model. Hydro-Quebec has recorded a number of disturbances and events at representative feeders on the network which provided very useful information for validating the DM dynamic performance. In the following section, comparisons of simulated and measured responses in voltage sag events are presented, and the validation is achieved by assessing the level of agreement between the two. A voltage sag (dip) is a reduction between 10% and 90% in rms voltage, with a duration between 0.5 cycles and 1 minute [94]. It is generally originated by a short circuit in the utility system and its magnitude

depends on power system topology, lines and cables impedance and the proximity to fault site. The comparisons are done for different events in order to test the model performance in various load sectors. The available measurement data provided by Hydro-Quebec include the actual recordings of instantaneous voltage and current waveforms.

One additional aspect of load modeling addressed in this section is the combination of component-based and measurement-based approaches. As outlined in Chapter 2, component-based approach employs a knowledge of modelling applicable to individual load components, as well as the participation of those components in the total load at a given bus. The measurement-based approach, on the other hand, does not require any similar knowledge and instead, relies on field measurements to develop load models. One of the difficulties associated with measurement-based approach which may limit its application is the availability of suitable measurement data coming from the field. In this research work, up to date measurements performed by Hydro-Quebec not only were used for model validation but ensured the availability of event data to benefit from the advantages of measurement-based approach as well. The combination of the two methods aims to refine the DM and find some additional information on load characteristics which will provide general considerations when modeling similar types of loads in power system studies. In the following case studies, two applications of measurements to the DM are highlighted. First during sensitivity analysis for finding more realistic load compositions and second for finding tripping characteristics of induction motors in a voltage sag.

4.5.1 Event at hospital-A

In the first case study, a voltage sag event recorded at the customer bus of a hospital in Montreal on 15:41 July 13th , 2020, was reproduced. According to the recorded instantaneous voltage waveforms at the load bus (refer to *"Hospital_A recording"* file), the disturbance lasted for 0.072 seconds and provoked 29.4% voltage drop on phase a, 26.1% voltage drop on phase b and 8% voltage drop on phase c of a 25 kV system, see solid lines in Figure 4.11 at t=3 s. An adjusted voltage source was developed in EMTP to reproduce the recorded instantaneous voltages (refer to *"Hospital_A"* EMTP file). This voltage source includes one controlled voltage sources and one table function (see Figure 3.4) for each phase. The table function was used to imitate the values of

the actual measured voltage signal, cycle by cycle. The result is presented in the dashed lines in Figure 4.11

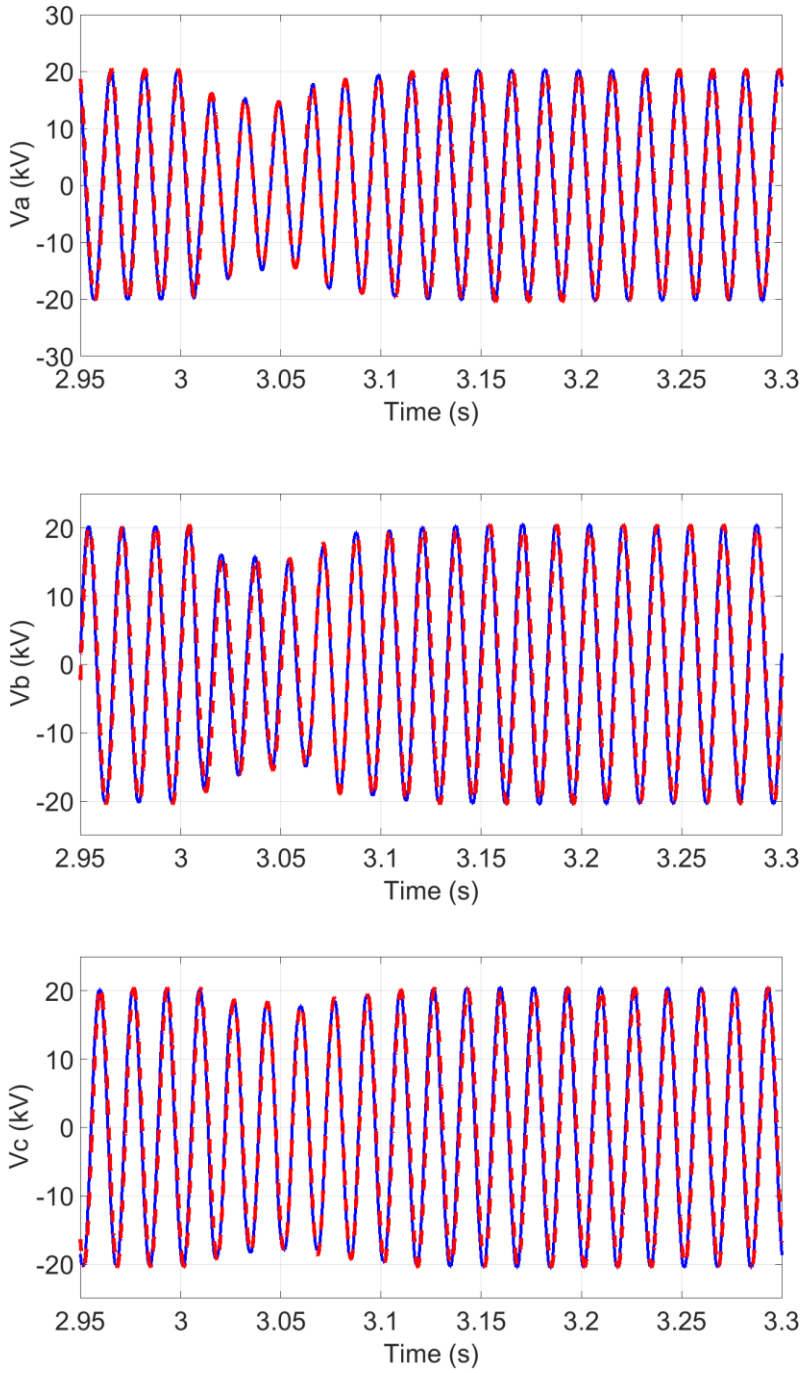

Figure 4.11 Three-phase voltages, simulation (red dotted) vs measurement (blue solid), Hospital-A case study

The event was reproduced by applying the adjusted voltage source to the DM of the hospital, formed using the following input data (for DM input parameters refer to Table 4.2):

- Voltage level at the load bus is 25 kV.
- Total active power: the recorded pre-fault power demand of the hospital is 8.2 MW.
- Load composition: As previously mentioned in this thesis, where enough information on the load composition is not available, estimations are made to come up with the best approximate. Since no information is available on the percentage contribution of components inside the hospital, first some assumptions were made based on the typical usage of a hospital on the time of the event. Next, further adjustments were made to that load composition in an attempt to match the simulation results with the measured signals as closely as possible. This adjustment procedure is further discussed in section 4.5.1.1 and is the first application of the measurement-based technique to the DM. The composition which provides the best match to the recordings is listed in Table 4.5.

Table 4.5 Load composition of Hospital-A

Load Component	**Composition**
Compressor	13%
Pump	20%
Fan	25%
Elevator	2%
CFL	10%
Incandescent	0%
LED	10%
SMPS	7%
Refrigerator	10%
Cooking	3%

- Percentage of drive-controlled motors: the fact that this hospital is not newly constructed, gives rise to an assumption that the percentage of VFD is not dominant. This presumption can be verified in two ways. First, by comparing the harmonic contents of the simulated and measured currents. This is because the source of existing current harmonics (mainly 5^{th} and 7^{th} order) is VFD and, to a lesser extent, CFL, LED and SMPS. It was observed that when all the motor loads of the DM were set to be directly connected, the best match is

achieved between the recorded and simulated currents in terms of harmonic contents. Figure 4.12 shows the comparison of the 5th harmonic of input current as the most dominant order. It is observed that simulation result matches the recording in steady-state (the mismatches which exist during the voltage sag will be explained in the following section). It should be noted that this comparison serves as another application of the measurements to find the percentage of drive-controlled motors. Second, the increase in the recorded currents during the voltage sag, see solid lines in Figure 4.14 at t =3 s, is due to directly connected motors. This is because when the voltage sag occurs, torque and speed of induction motors are dropped below the nominal values. As a result, the current increases gradually to compensate the speed loss so as to restore the electrical torque. The current increase during the fault for one type of motor, i.e., the compressor, is shown in Figure 4.13.

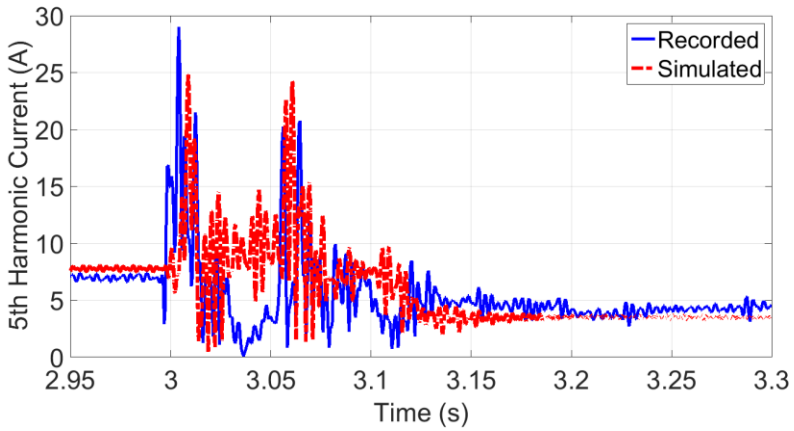

Figure 4.12 Simulated vs. recorded harmonic currents, Hospital-A case study

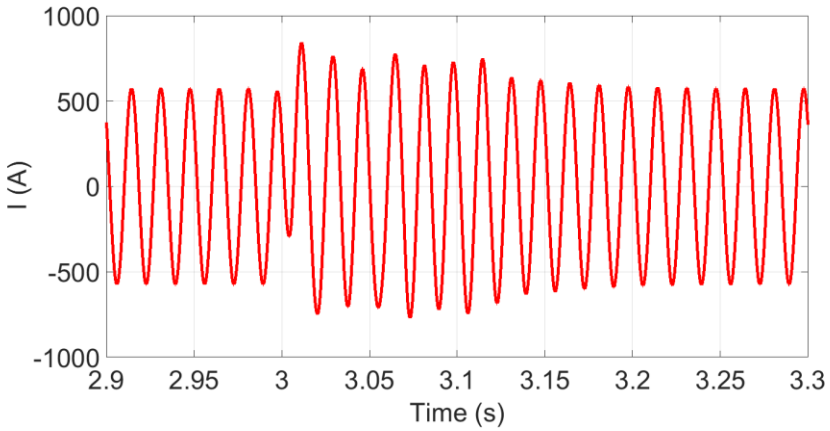

Figure 4.13 Current waveform of compressor motor, Hospital-A case study

- Another application of the measurements is to provide some information on load disconnection during voltage sag. Observing the recorded active power in Figure 4.15, it is noticed that the hospital lost 2 MW of its load after the fault. This load loss was captured in the DM within 42% drop of motor loads 6 cycles after the beginning of the voltage sag. This result can be verified with existing information on motor tripping patterns; contactors of motor loads drop out at voltage levels around 45-55% nominal voltage [11]. The normal time for contractors of motor loads to drop out is about 1-3 cycles which in this case implies an incorrect adjustment of motor protection system.

The adjusted voltage source which reproduced the actual instantaneous voltages was applied to the tuned DM of Hospital-A with the above input data. Simulation results are presented in Figure 4.14 for three-phase currents and Figure 4.15 for active and reactive powers. It can be observed that simulated currents match the recorded ones before and after the voltage sag. The mismatches which exist during the voltage sag can be explained by the fact that the considered hospital is equipped with automatic power factor controller. The controller in conjunction with a programable logic controller (PLC) is employed for switching multi-step capacitor banks to meet the desired power factor. The recorded currents imply the switching off in capacitor banks during the voltage sag (Figure 4.14, I_a at t=3 s) and switching on after the fault. The differences in the simulated and recorded reactive powers during the sag is also attributed to the same power factor correction strategy. In order to capture the effect of this power factor correction on the current and reactive power waveforms, some hypothetical capacitor banks switching scenarios were simulated. However, because the capacitor banks are designed to come on and off automatically in several steps based on desired power factor, more information is required for simulation, e.g., number and value of capacitor banks and their switching time. Due to lack of such information, the impact of power factor correction strategy could not be captured in simulation of current (specifically phase "a") and reactive power waveforms. Better matching is observed between the simulated result and measured data of the active power. It should be noted that in the real power system, there will always be variability and uncertainty in the load model data. It is not possible to have exact information about all the components at any given time. Therefore, an exact match between simulated and measured data can not be achieved and some discrepancy is to be expected. What is more important is that the model gives results that are in the same order of magnitude as the

measurements before the fault and after fault removal, and also can follow the trend of dynamics during the fault.

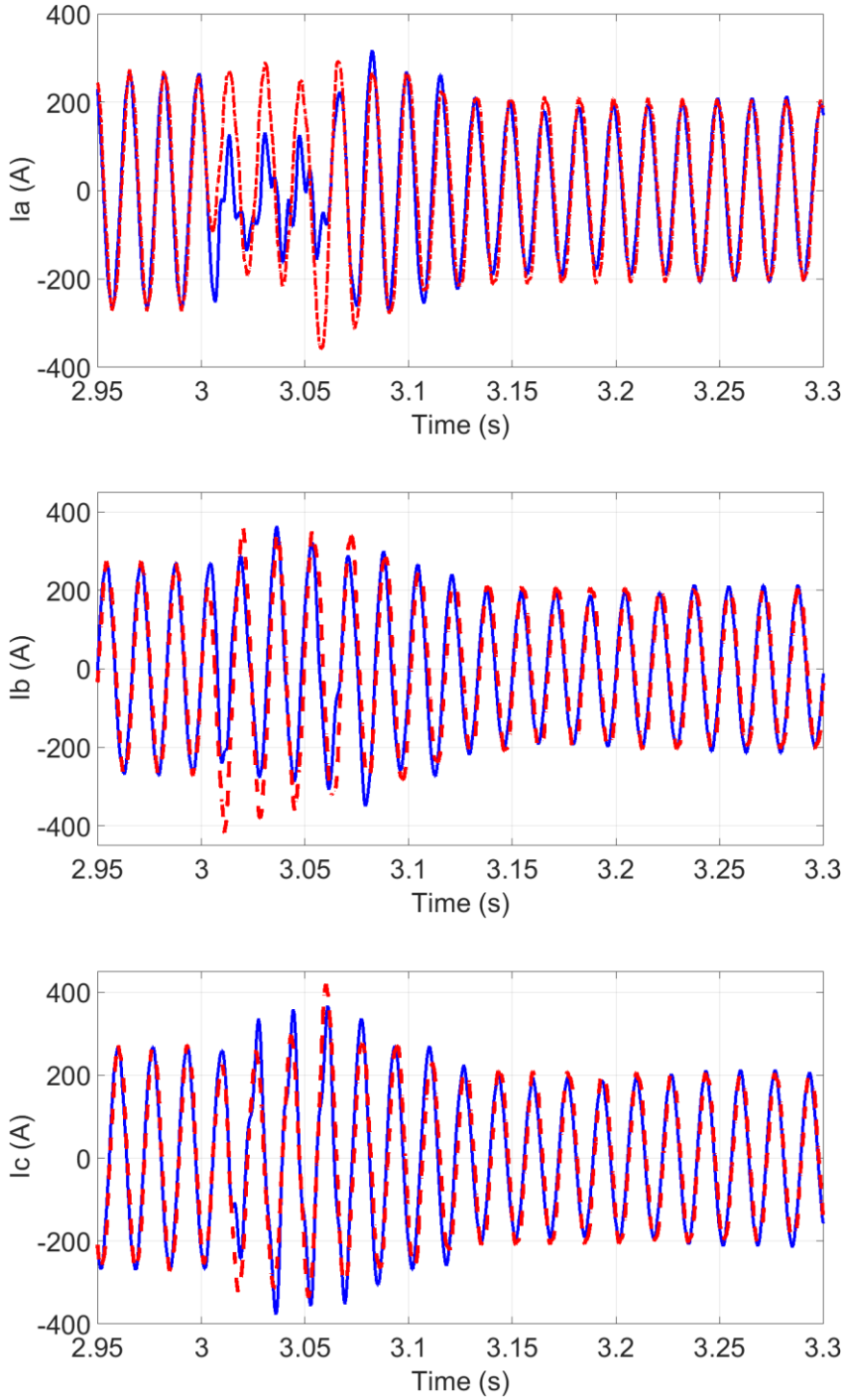

Figure 4.14 Three-phase currents, simulation (dotted) vs measurement (solid), Hospital-A case study

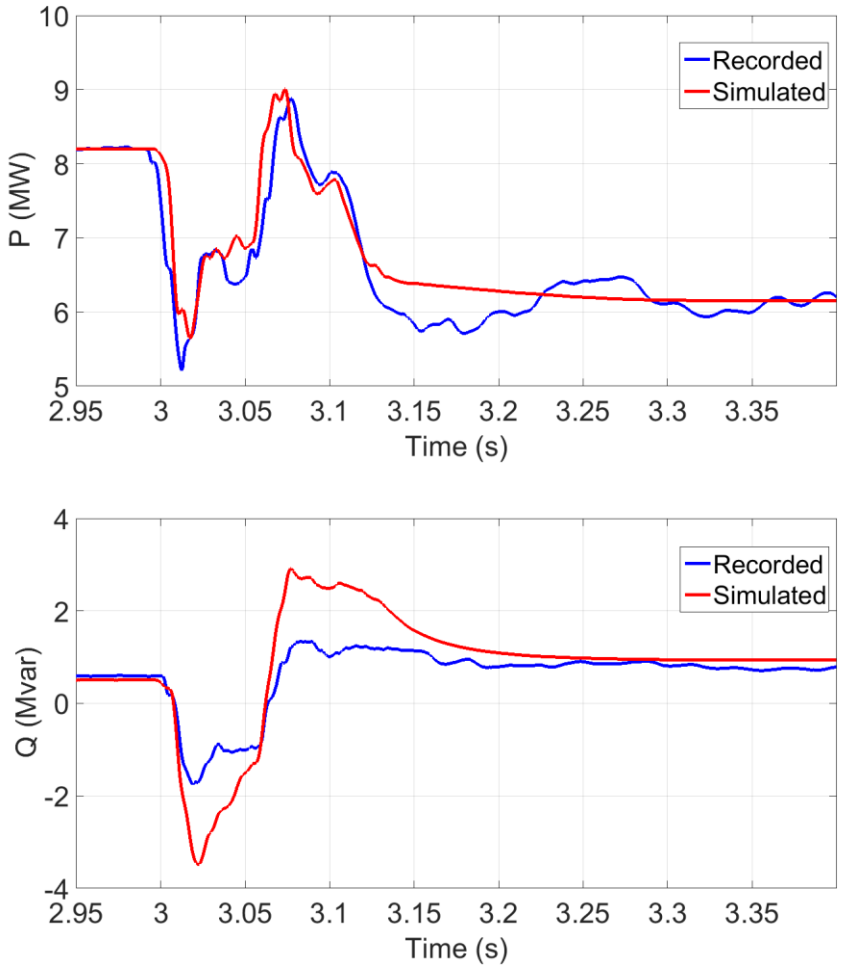

Figure 4.15 Simulated active and reactive powers vs. measurement, Hospital-A case study

4.5.1.1 **Sensitivity analysis**

Before proceeding to the second case study, this section presents the procedure which was followed to adjust the load composition in Hospital-A. The procedure is illustrated in the form of a sensitivity analysis which highlights the influence of each load component on the electrical characteristics of the total load. The results identify the set of general points so that the load model tuning process can specifically focus on refining those parameters when reproducing actual measured responses.

The adjustment was initiated by making an assumption on the percentage contribution of motor components i.e., three-phase and single-phase directly connected induction motors. For this purpose, the results presented in Table 4.4 for a typical commercial consumer in summer was used i.e., 50% contribution of three-phase IM. Information of the commercial consumer was applicable

to the hospital load due to similarity of electrical devices found in the end-use applications of the two. 50% contribution of three-phase IM was equally distributed between three types i.e., compressor, fan and pump. For the single-phase motors, 10% contribution was considered which was estimated to be twice as a commercial load due to more consumption of refrigeration. Next, small percentages of 3% and 2% were assumed for cooking and elevator consumptions, respectively. The remaining 35% was divided equally between lighting components and SMPS.

Contribution of three-phase IM: Figure 4.16 shows a comparison between the recorded power signals and simulation results using the described initial assumed load mix i.e., 50% three-phase IM, 10% single-phase IM, 3% cooking, 2% elevator and 35% divided equally between lighting and SMPS. It can be observed that even with this initial assumption, as long as it is sufficiently accurate based on the type of load, season and time of event, the simulated response remains fairly close to the measurement. For further adjustments, first the reactive power consumption in steady-state (before and after the fault) was considered which is slightly higher than recording in this case; this observation suggests a slight increase in the percentage of components with higher power factors. Three-phase motors in this case study have power factors close to unity since they are equipped with capacitors for reactive power compensation at their terminals. An increase from 50% to 58%, which implies 8% reduction in lighting and SMPS resulting in final percentage of 27% from 35%, provides the best match to the measured reactive power in steady-state before and after the fault. As previously stated, it is not possible to find the exact load composition at each given time because load model data will always have uncertainty. If there is a reasonable match between the measured and simulated responses, it indicates that the considered compositions are sufficiently accurate. This is an iterative process and engineering judgment needs to be applied.

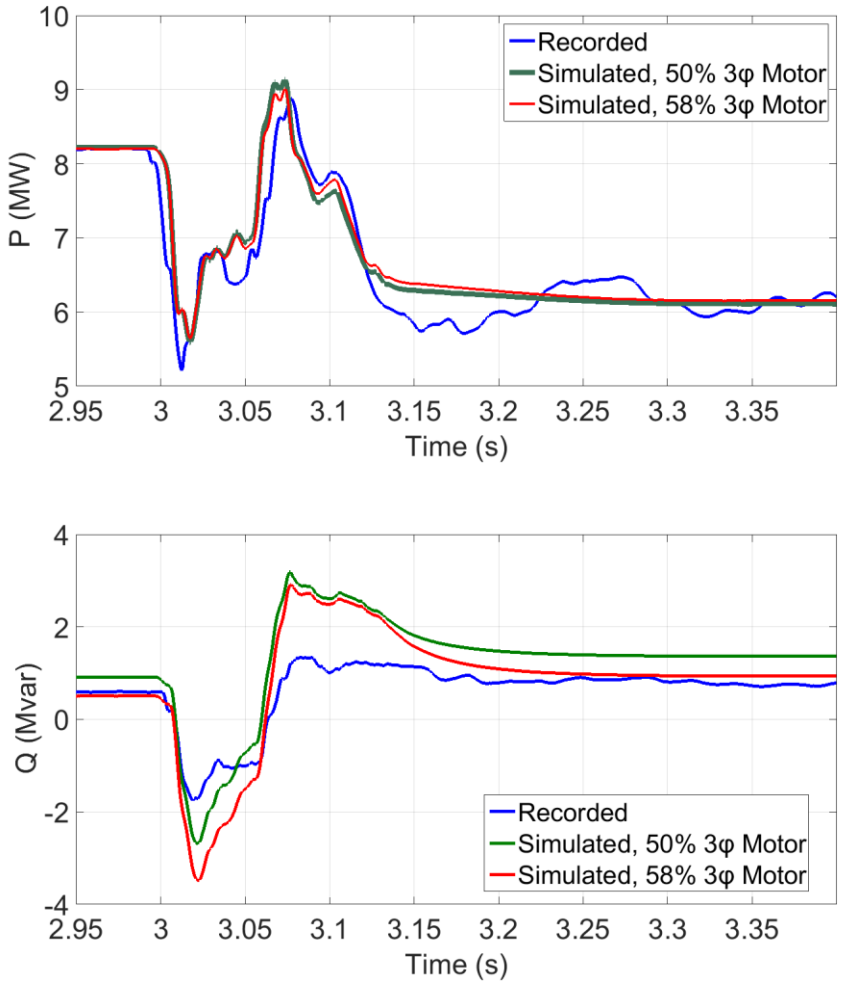

Figure 4.16 Simulated active and reactive powers vs. measurement, effect of percentage contribution of three-phase IM, Hospital-A case study

Lighting components and SMPS: As Figure 4.16 showed, the impact of lighting and SMPS categories on the load power demand waveforms is on the amount of reactive power consumption in the steady-state; the higher their contribution, the more is consumption of reactive power. Since components of these two groups have power factors close to each other (around 0.91), no significant impact can be expected from changing the composition within their groups (see reactive power in Figure 4.17 before and after the fault). Moreover, due to their static nature, the general shape of the transient response during the fault is not affected by these categories. However, increasing the percentage of SMPS will result in higher active power during the voltage sag, see active power in Figure 4.17. This is because of its approximately constant active power

characteristics as previously discussed in section 3.2.3, n_p is zero. A load mix of 20% lighting and 7% SMPS provides the best match to the measured signal.

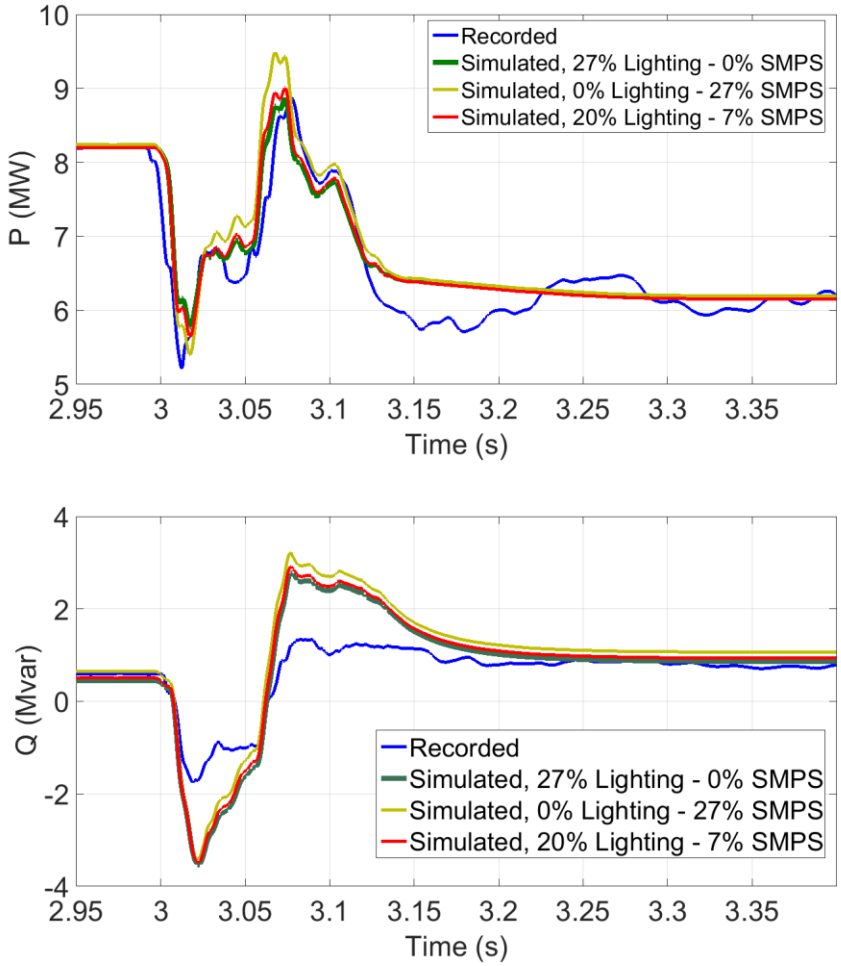

Figure 4.17 Simulated active and reactive powers vs. measurement, effect of percentage contribution of lighting and SMPS, Hospital-A case study

Different types of three-phase IM: The percentage contribution of different types of three-phase IM (i.e., compressor, fan and pump) is one of the key elements that defines the dynamic behavior during the fault. Different motor compositions can result in different model responses to the variation of system voltage. This is because the consequences of a voltage sag in the induction machine are the speed loss and the current and torque peaks that appear as the voltage drops and recovers. This transient response and the values of the peaks depend on different elements, such as the electrical parameters of the machine, the characteristics of the load and inertia. Figure 4.18 is

the simulation results of electric power of different motors in the hospital load measured at their terminals during the voltage sag . It should be noted that the pulsating torque with double frequency is the result of the unbalanced voltage sag (as shown in Figure 4.11) in this case study.

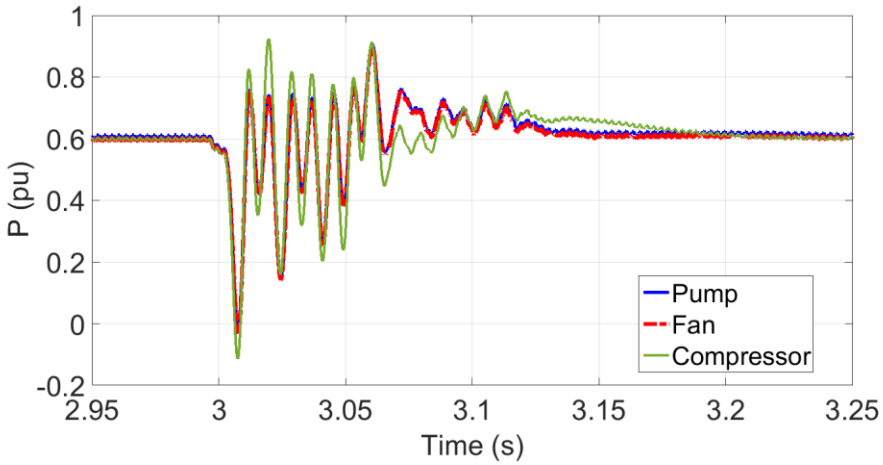

Figure 4.18 Three-phase IM electric power during voltage sag, Hospital-A case study

With a sufficiently accurate mix of motor loads, the dynamics can be matched with the actual response of the load during the voltage sag. In Figure 4.19, the green curve illustrates the simulated responses when all the motor consumption is attributed to the compressor. Although the result is acceptable, increasing the percentage of fan and pump (which is a more reasonable assumption of the actual load mix), makes the simulation result closer to the actual response.

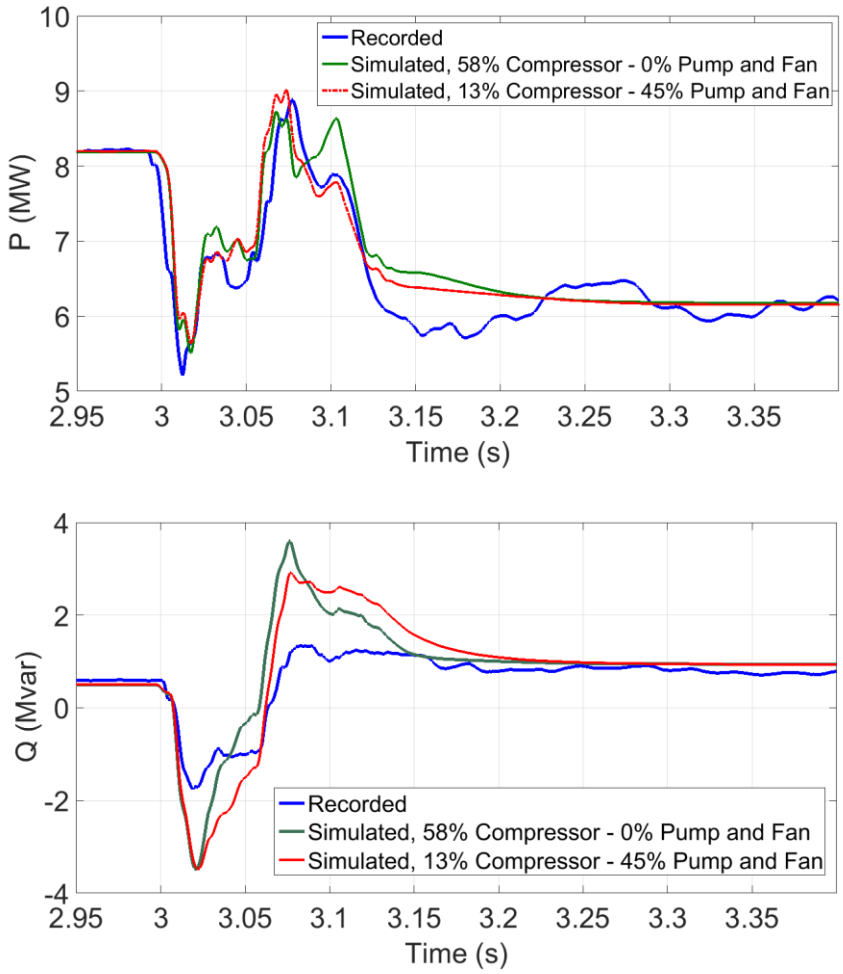

Figure 4.19 Simulated active and reactive powers vs. measurement, effect of percentage contribution of different types of three-phase IM, Hospital-A case study

Motor inertia: The other key point is the sensitivity of the dynamic response to three-phase IM inertia. In Figure 4.20, the difference between the two responses is because the low inertia motor drops its speed rapidly and subsequently restores the speed soon after voltage sag ends. In case of a higher inertia, the motor undergoes slower speed drop and speed recovery.

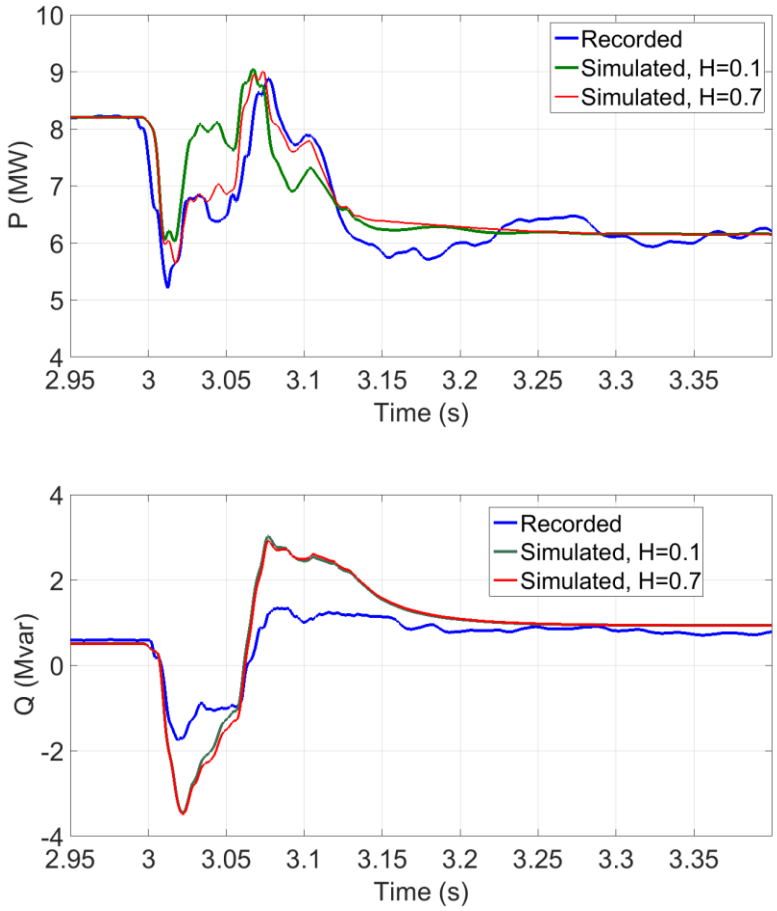

Figure 4.20 Simulated active and reactive powers vs. measurement, effect of motor inertia constant, Hospital-A case study

4.5.2 Event at Hospital-B

A recorded voltage sag on 13:23, September 14th , 2020, at the bus of another hospital was selected as the next case study. What differentiates this hospital from the former (Hospital-A) is that it is not equipped with automatic power factor controller whose insufficient information caused some uncertainty in the first case study. This event lasted for 0.126 seconds and caused 10.2% voltage drop on phase a, 94.3% voltage drop on phase b and 93.6% voltage drop on phase c of a 25 kV system (refer to *"Hospital_B recording"* file). In this case study, the recorded voltages were reproduced by connecting a 25 kV voltage source to the load bus, placing faults at the bus and adjusting the fault impedance so that the simulated instantaneous voltages match the measured ones

(refer to *"Hospital_B"* EMTP file). The recorded and simulated voltage waveforms are shown in Figure 4.21.

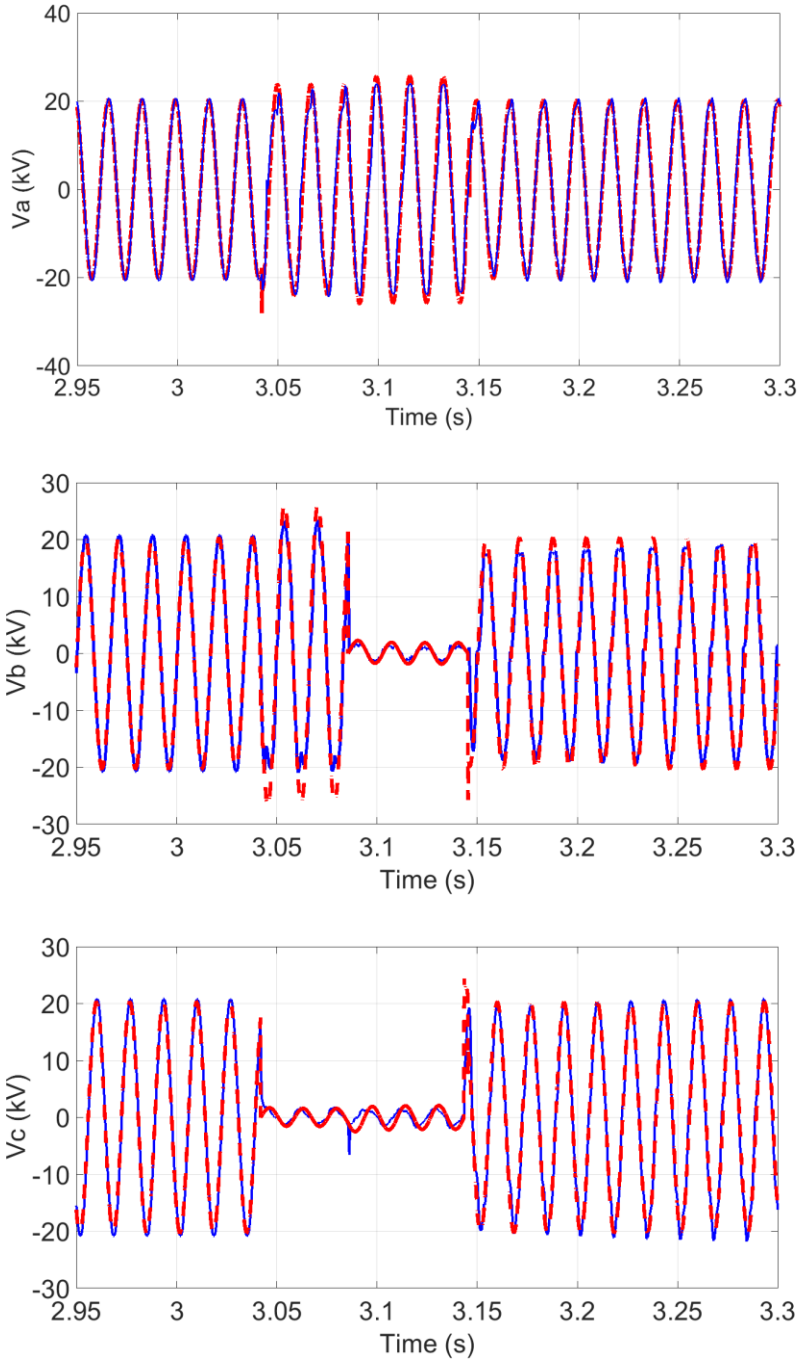

Figure 4.21 Three-phase voltages, simulation (red dotted) vs. measurement (blue solid), Hospital-B case study

The event was reproduced by applying the adjusted voltage sag to the DM of the hospital. The DM was formed using the following data:

- Voltage level at the load bus is 25 kV.
- Total active power: the recorded pre-fault power demand of the hospital is 5.6 MW.
- Load composition: the assumed load composition is listed in Table 4.6. Similar to the case of the first hospital, this assumption is based on the time of the event and was further adjusted to match the measured signals as closely as possible in a way explained in section 4.5.1.1.

Table 4.6 Load composition of Hospital-B

Load Component	**Composition**
Compressor	3%
Pump	20%
Fan	25%
Elevator	2%
CFL	0%
Incandescent	0%
LED	30%
SMPS	7%
Refrigerator	10%
Cooking	3%

- Percentage of drive-controlled motors: by performing harmonic analysis on the recorded current waveforms, it was observed that when 50% of motors are controlled by variable speed drives, the best agreement is achieved between the simulated and recorded currents in terms of harmonic contents. The comparison between the 5^{th} harmonic of the simulated and recorded currents is presented in Figure 4.22. It should be noted that the measured and simulated signals do not exactly match due to the fact that load composition will always have some uncertainty. The differences can also be observed in the current waveforms of Figure 4.23.

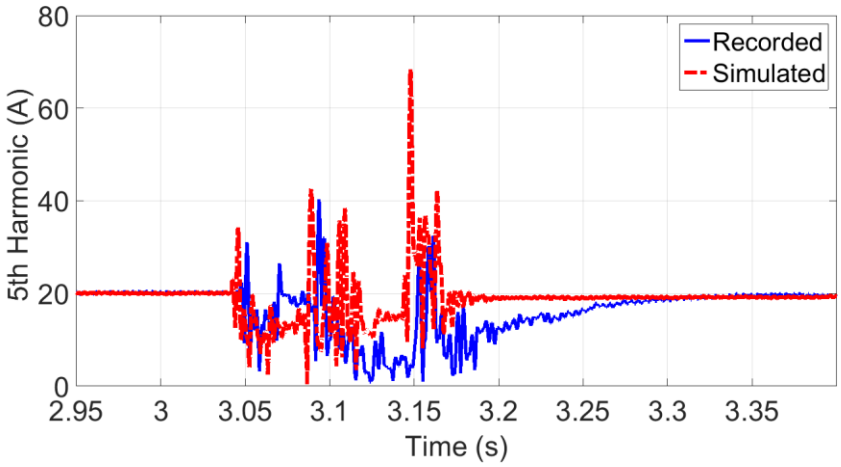

Figure 4.22 Simulated vs. recorded harmonic currents, Hospital-B case study

- Knowledge on the load loss, as additional data for DM tuning, can be derived from the available measurements. The active power waveform in Figure 4.24 (solid line) shows that this hospital lost 1 MW of its load during the fault which according to the discussion in section 4.5.1 is related to tripping of motor loads. Moreover, similar pre-fault and post-fault current harmonics, see Figure 4.22, is an indication of presence of drive-controlled motors after the fault. The load loss is hence attributed to the tripping of directly connected motors which is captured by 90% drop of motor loads during the simulation.

The adjusted voltage sag which reproduced the actual instantaneous voltages was applied to the tuned DM of Hospital-B with the above input data. Simulation results are presented in Figure 4.23 for three-phase currents and Figure 4.24 for active and reactive power. As observed, the simulated results in this case study, with no automatic power factor controller, are in better agreement with corresponding measurements as compared to the first hospital which suffered the lack of data on the behavior of the power factor controller.

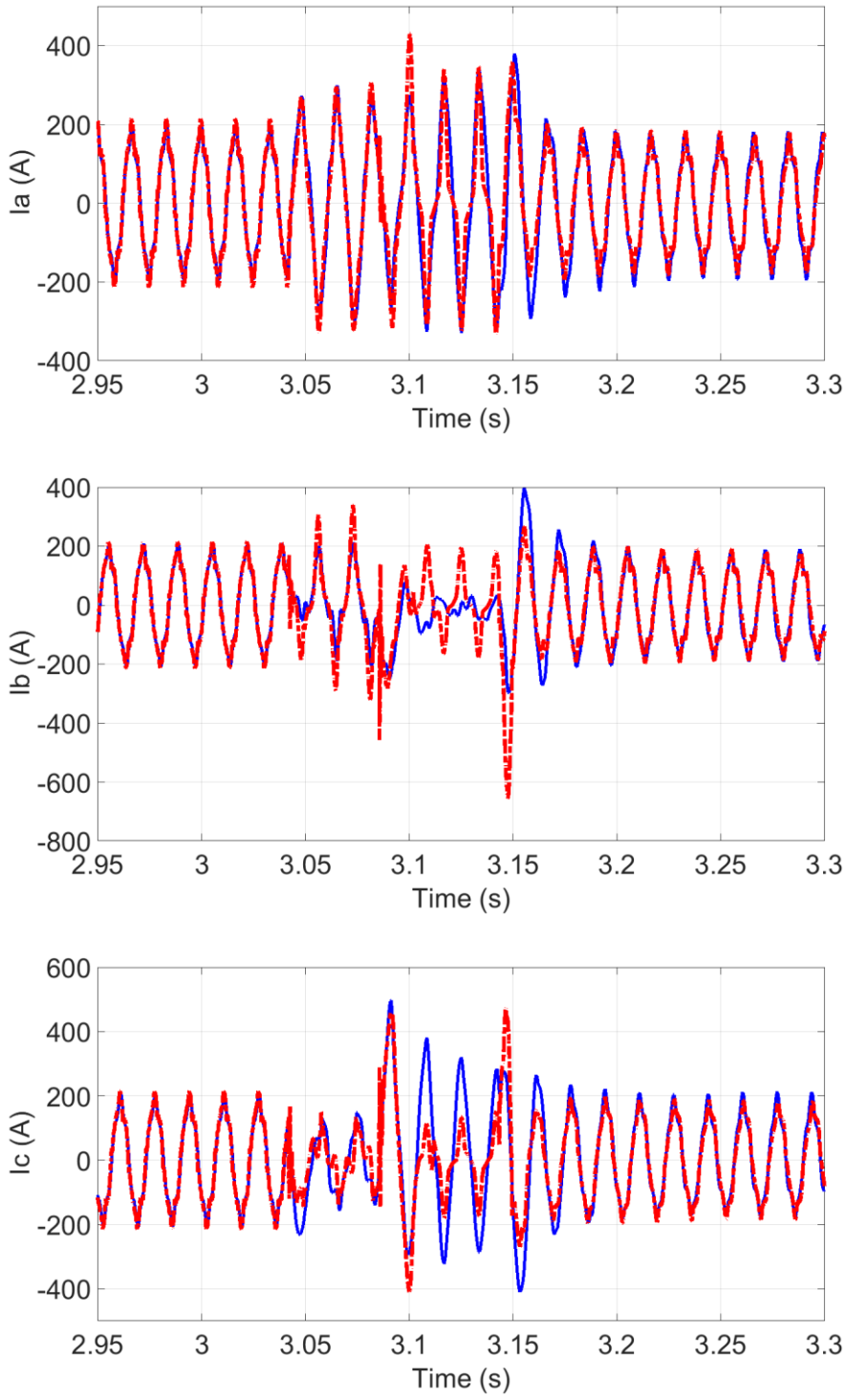

Figure 4.23 Three-phase currents, simulation (dotted) vs. measurement (solid), Hospital-B case study

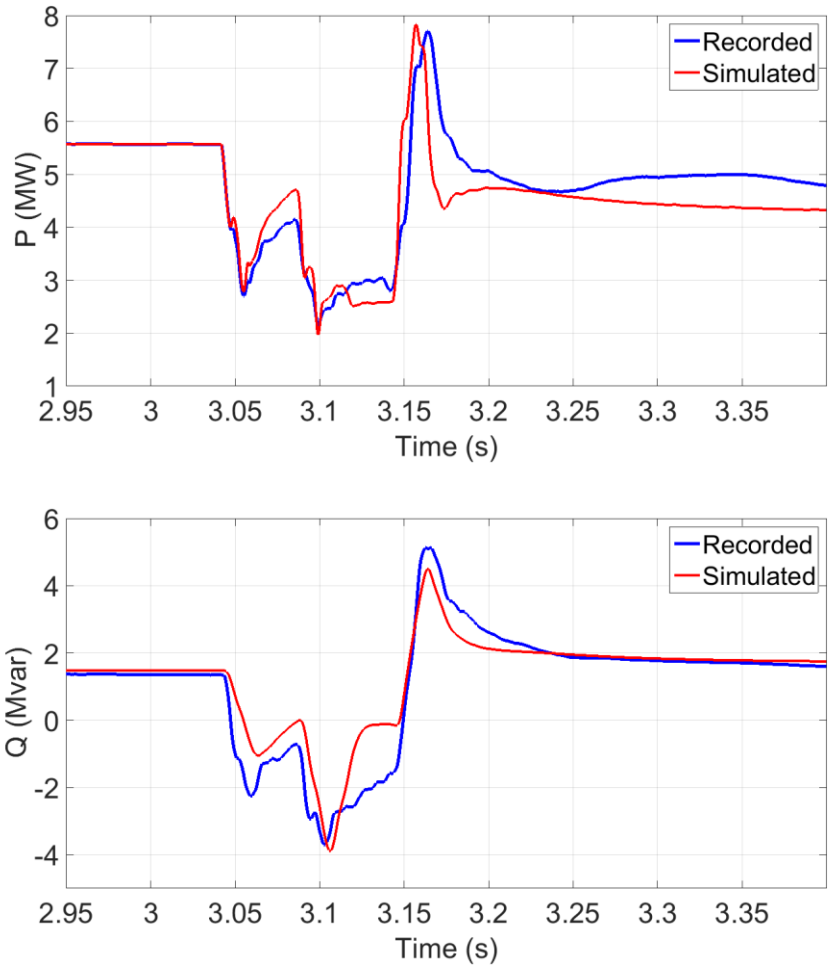

Figure 4.24 Simulated active and reactive powers vs. measurement, Hospital-B case study

4.5.3 Event at a commercial center

This case study is related to a recorded voltage sag event at a commercial center (shopping mall) in Montreal which occurred at 11:46 September 29th , 2020. The recorded voltage waveforms designate a disturbance that lasted for 0.296 seconds, with following voltage drops that appeared on the three phases: 67.9% voltage drop on phase a, 64% voltage drop on phase b and 62.8% voltage drop on phase c of a 12.47 kV system (refer to *"Commercial recording"* file). Similar to the previous case study, the recorded voltages were reproduced by connecting a 12.47 kV voltage source to the load bus, placing faults at the bus and adjusting the fault impedance so that the simulated instantaneous voltages match the measured ones (refer to *"Commercial_center"* EMTP file). The recorded and simulated voltage waveforms are shown in Figure 4.25.

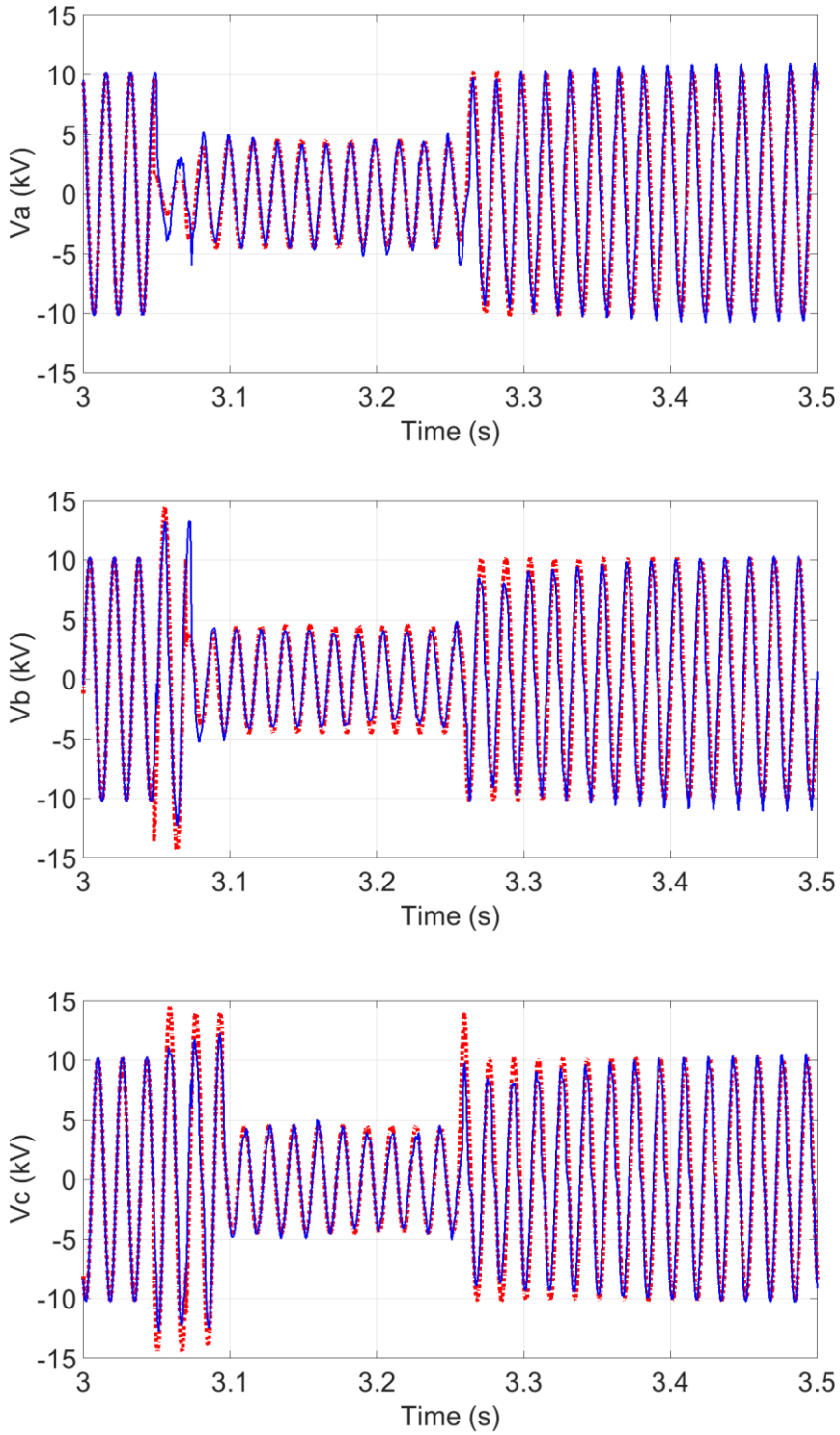

Figure 4.25 Three-phase voltages, simulation (dotted) vs. measurement (solid), commercial center case study

The adjusted voltage source was applied to the DM of the shopping mall, formed by the following input data:

- Voltage level at the load bus is 12.47 kV.
- Total active power: the recorded pre-fault power demand of the commercial center is 1.52 MW.
- Load composition: the assumed load composition is listed in Table 4.7. Similar to the previous case studies, this assumption is based on the typical usage of a commercial center at the time of the event and was iteratively adjusted to match the measured signals as closely as possible.

Table 4.7 Load composition of the commercial center

Load Component	**Composition**
Compressor	22%
Pump	8%
Fan	8%
Elevator	0%
CFL	20%
Incandescent	0%
LED	20%
SMPS	15%
Refrigerator	5%
Cooking	2%

- Percentage of drive-controlled motors: when all the motors were made to be directly connected in the DM, the best agreement was achieved between the simulated and recorded currents in terms of harmonic contents. The 5^{th} harmonic contents of the measured and simulated currents are compared in Figure 4.26.

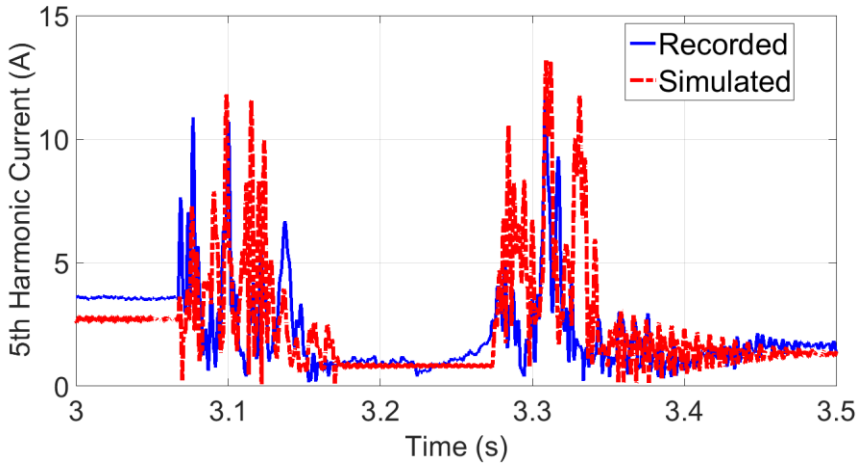

Figure 4.26 Simulated vs. recorded harmonic currents, the commercial center case study

- Information on the load loss can be deducted from measurements. The low recorded currents during the fault (see Figure 4.27, solid lines at t=3.1 s) is an indication of motor tripping. However, load loss is not observed after the fault is removed; so, it can be concluded that the motors reconnect after voltage recovery. The observed inrush current at the time of voltage recovery (see Figure 4.27, solid lines at t=3.3 s) supports this notion of motor reconnection. This can also be verified with existing information on motor reconnection; when voltage recovers to about 65% of the nominal value, motor contactor will reclose within 6 cycles [11]. In this case, dropping all motors during simulation of the voltage sag and reconnection of 70% of motors after voltage recovery provided the best match to the recorded currents. It should be noted that dropping of motors during voltage sag and their reconnection after voltage recovery cannot be generalized and depends on the controls and protection parameters associated to each motor load.

Simulation results by applying the adjusted voltage sag to the tuned DM of the commercial center with the above input data is presented in Figure 4.27 for three-phase currents and Figure 4.28 for active and reactive powers. It is observed that the simulated responses are in close agreement with the measurements. As previously mentioned, because load component data always has some uncertainty, it is not possible to capture the exact measured response.

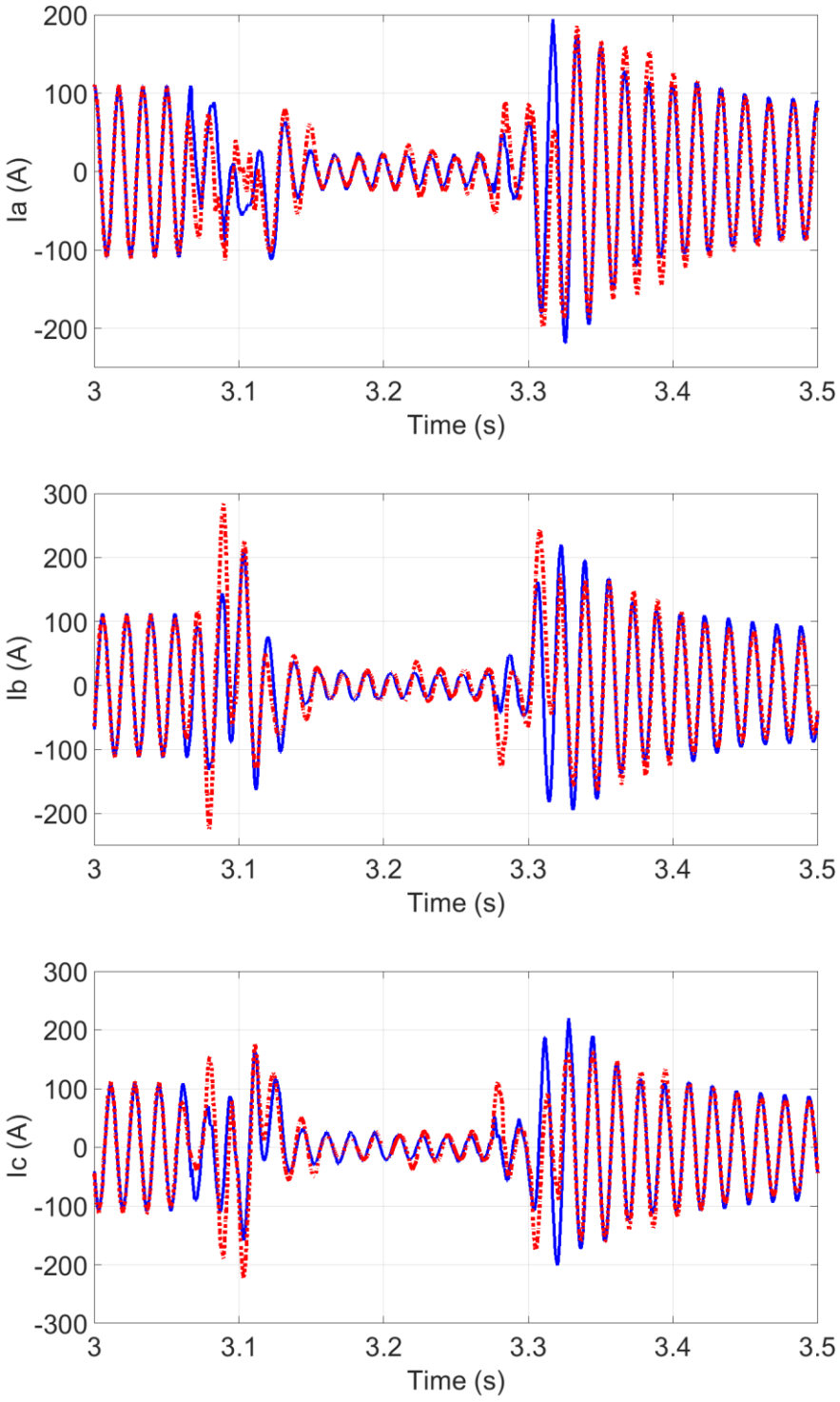

Figure 4.27 Three-phase currents, simulation (dotted) vs. measurement (solid), commercial center case study

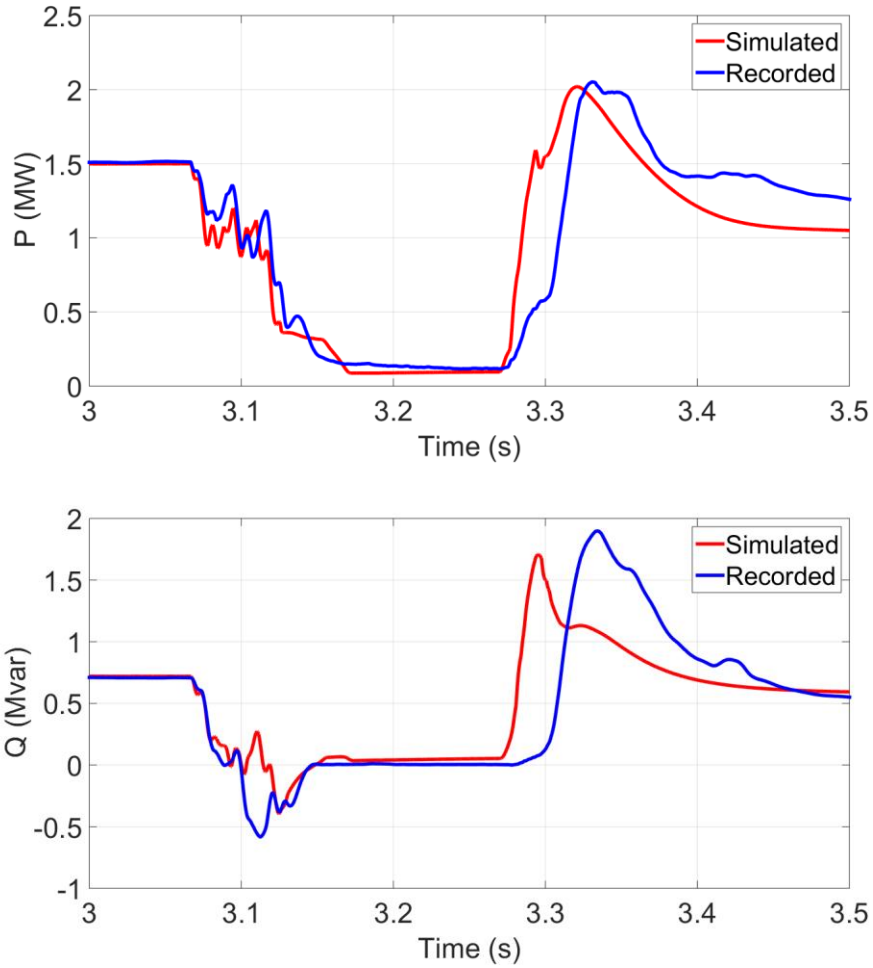

Figure 4.28 Simulated active and reactive powers vs. measurement, commercial center case study

4.5.4 Event at a residential area

The behavior of DM in the residential sector is demonstrated by reproducing two available voltage sag recordings related to a specific residential area in Montreal. Google Earth application [95] was used in order to locate this area and identify the type and number of consumers; about 600 houses and one small industry. In this case study, the single-line diagram of the network under study was provided by Hydro-Quebec as shown in Figure 4.29. The load is supplied from a 230/25 kV substation through 250 km lines. In this case study, the voltages were reproduced by modeling the real network and simulating faults at the distribution bus.

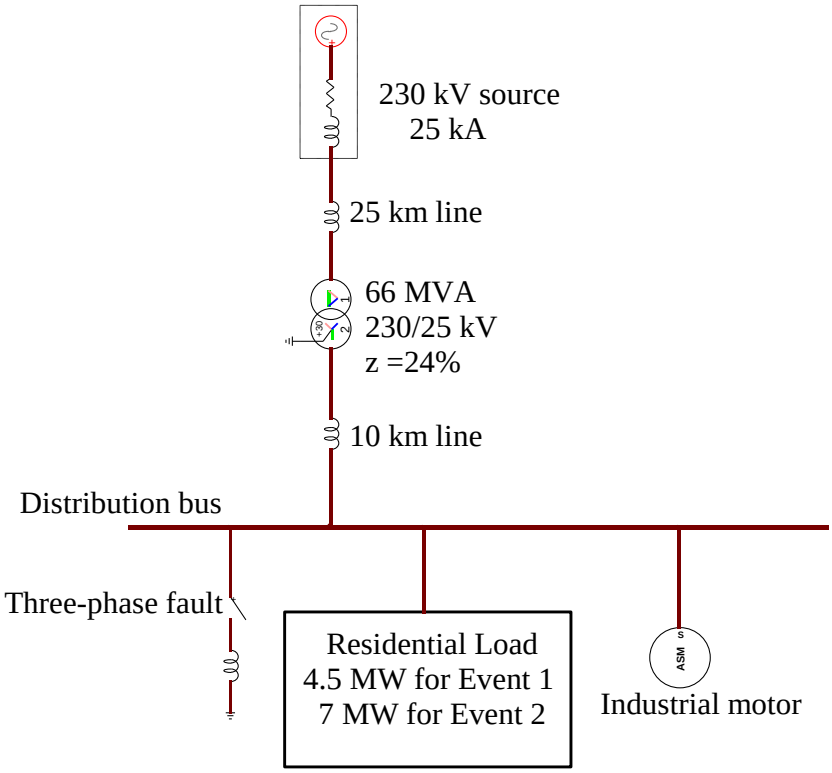

Figure 4.29 Single-line diagram of the residential case study

4.5.4.1 **Event 1**

The first event is a voltage sag with 66.8% voltage drop on phase a, 66.6% voltage drop on phase b, and 65.7% voltage drop on phase c, which lasted for 0.8 seconds, see Figure 4.30 (solid lines) (refer to *"Residential recording"* file). This event was recorded on 8:50 August 21st, 2020. The network of Figure 4.29 was built in EMTP, and a fault was imposed at the distribution bus. The fault impedance was adjusted to give an accurate representation of the event so that the simulated instantaneous voltages at the distribution bus match the measured ones (refer to *"Residential"* EMTP file). Figure 4.30 presents the recorded and simulated voltage waveforms.

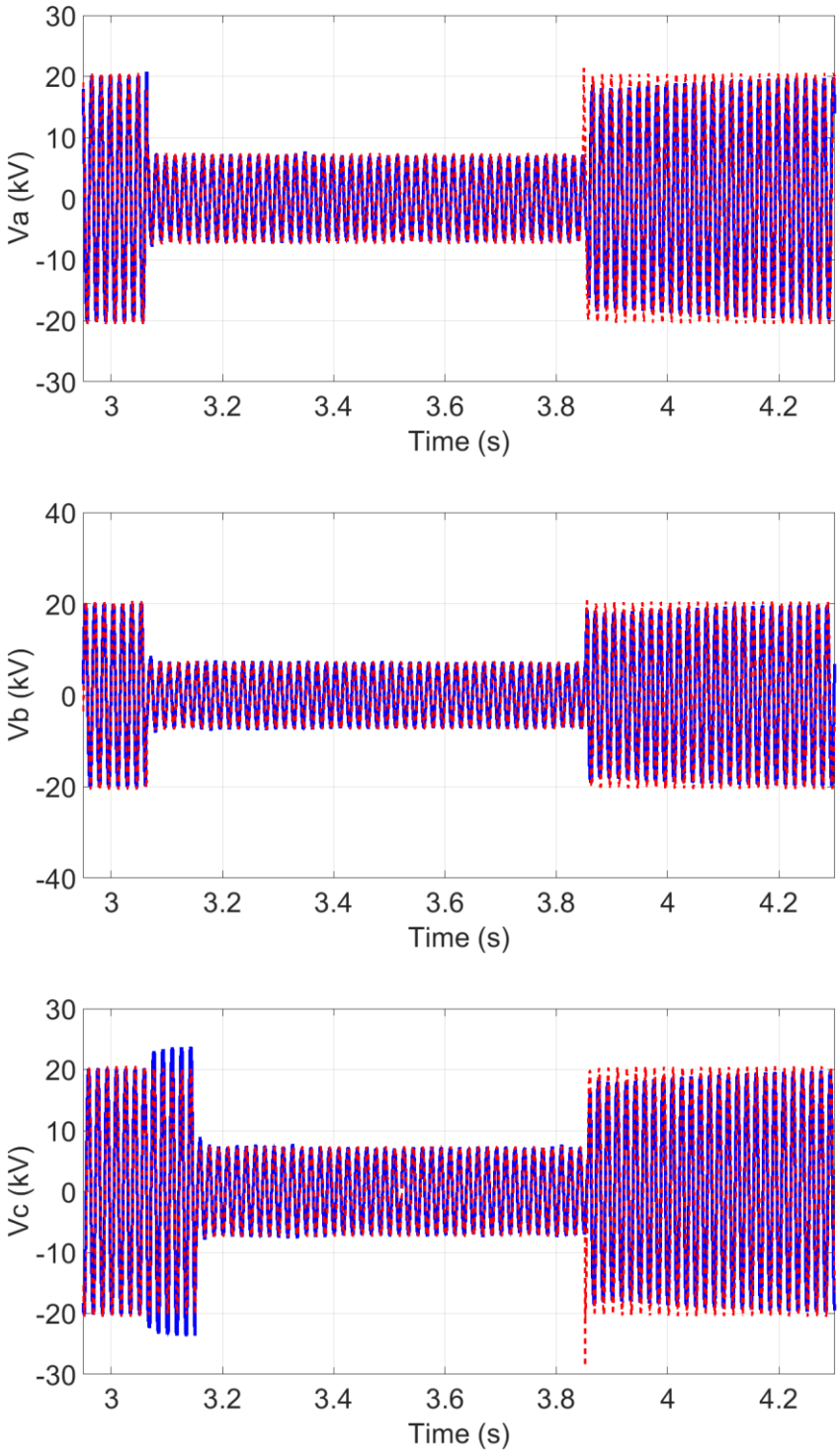

Figure 4.30 Three-phase voltages; simulation (dotted) vs. measurement (solid), residential load case study, event 1

The DM in this case study was formed with the following input data:

- Voltage level at the load bus is 25 kV.
- Total active power: the recorded pre-fault power demand of the load is 4.5 MW.
- Load composition: at the time of this event (i.e., 8:50), no major activities are expected from the industrial consumer, so the whole consumption was attributed to the residential sector. The assumed load composition is listed in Table 4.8 based on the information provided in [46] for typical residential consumption at the time of this event. Some minor adjustments were made to match the measured signals more closely.

Table 4.8 Load composition of the residential load, event 1

Load Component	**Composition**
Incandescent	3%
CFL	7%
TV+PC	32%
Refrigerator	16%
Dish Washer	5%
Cloth Washer	2%
Dryer	10%
Cooking	10%
Water Heater	15%

- Percentage of drive-controlled motors: residential load mix does not include any directly connected or drive-controlled three-phase IM.
- Unlike the previous case studies in which some information on the load loss was deducted from measurements, no loss of load is observed in this case. However, the measurements retain some information on the load torque characteristics of single-phase IM. Since the dynamic behavior of a residential load is governed by single-phase IM, a significant point in the simulation of this case is the selection of realistic parameters for modeling those motor loads. Motor parameters related to different end-use applications were previously presented in Table 3.4. Although some references have addressed the load torque characteristics attributed to different types of single-phase motors, some disagreement exist between the available information. While [53] has presented refrigerator motors as CT

mechanical load type, [54] has referred to them as QT. While washers, dish washers and dryers are considered as QT in [53], the same motors are considered as CT in [54]. Several simulations were performed using different types of mechanical loading for each single-phase motor and the results showed that QT mechanical load types reproduce the measured behavior more realistically. Figure 4.31 compares active and reactive power demands when mechanical loads are adjusted to CT and QT. The difference between the two responses at new steady-state i.e., after t=3.8 s, is due to the stall of certain motors. This can be explained by different behavior of decelerating torque during the voltage sag which act on the rotors of motors coupled with distinct mechanical loads. The torque of motors coupled with QT drop with square of speed reduction which imply lower deceleration torque leading to the minimum speed loss during the fault. On the other hand, the CT mechanical load remains unchanged during the fault. Therefore, higher decelerating torque and higher speed loss is expected in such motors. This means motors coupled with CT mechanical load are more prone to stall where the load torque cannot be overcome by the electrical torque provided to the motor. In this situation, motors draw extremely high amounts of current during reacceleration when the voltage recovers to normal operating level. This high current leads to excessive reactive power demand as observed in the reactive power demand in Figure 4.31. In Figure 4.32 slip of CT motors illustrates the electrical behavior of stalling.

Simulation results of the network presented in Figure 4.29 using the tuned DM for the residential load are presented in Figure 4.33 for three-phase currents and Figure 4.34 for active and reactive power. It is observed that the measured and simulated responses are in good agreement.

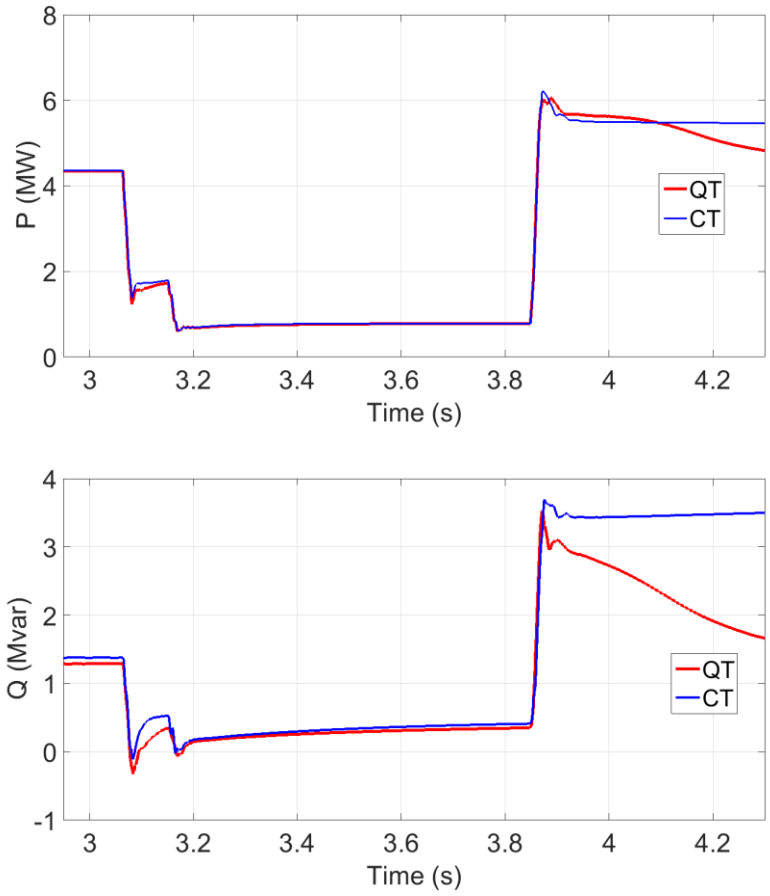

Figure 4.31 Comparison of simulated active and reactive powers, single-phase IM adjusted to QT and CT mechanical load types, residential load case study, event 1

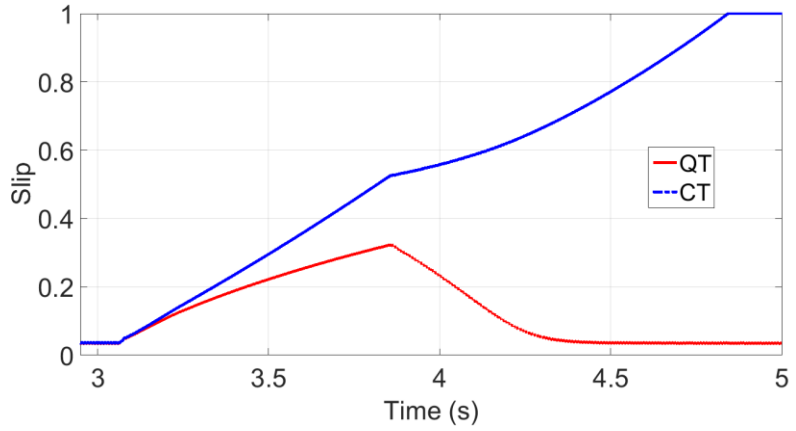

Figure 4.32 Single-phase IM slip comparison, QT and CT mechanical load types, residential load case study, event 1

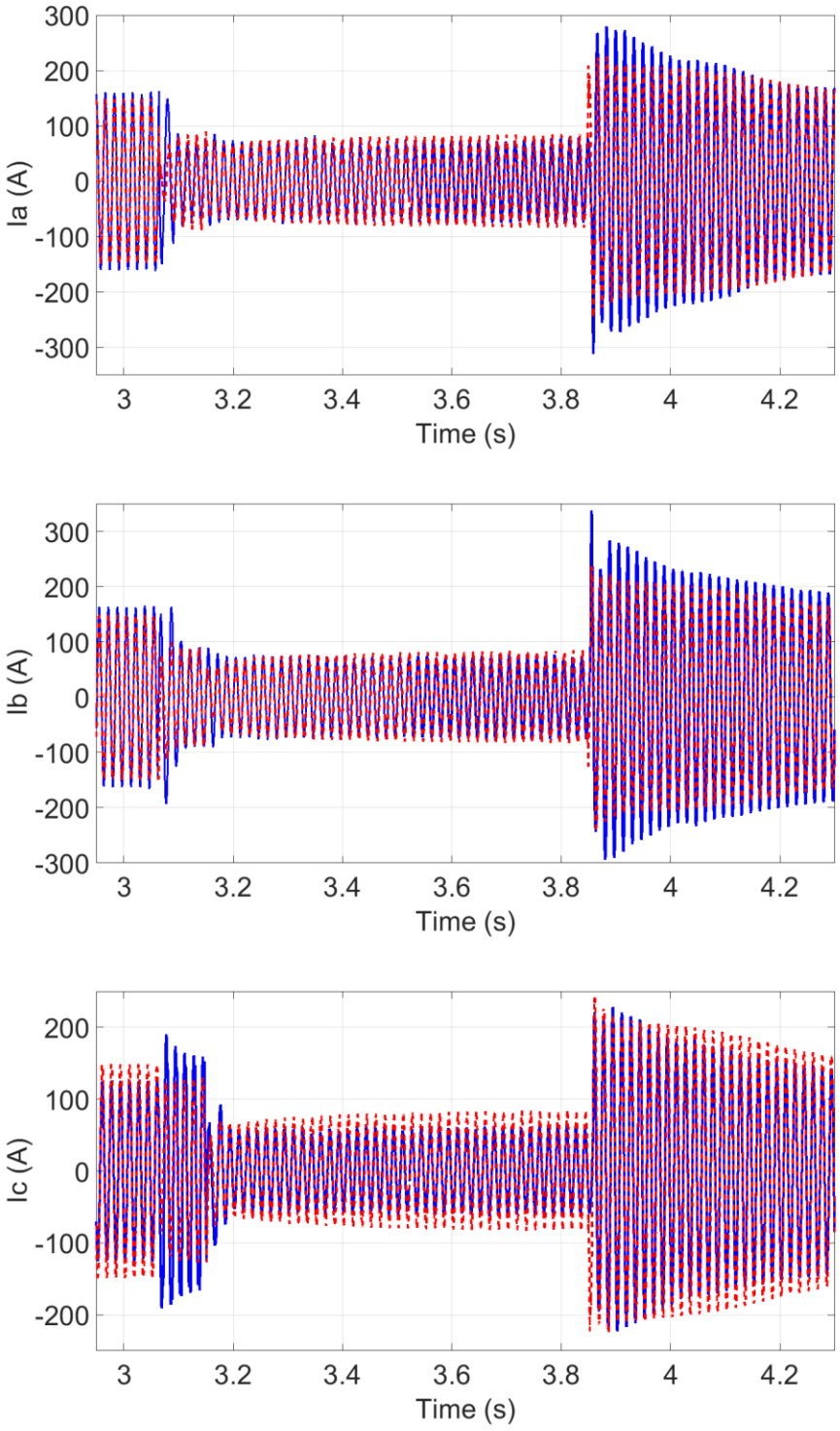

Figure 4.33 Three-phase currents; simulation (dotted) vs. measurement (solid), residential load case study, event 1

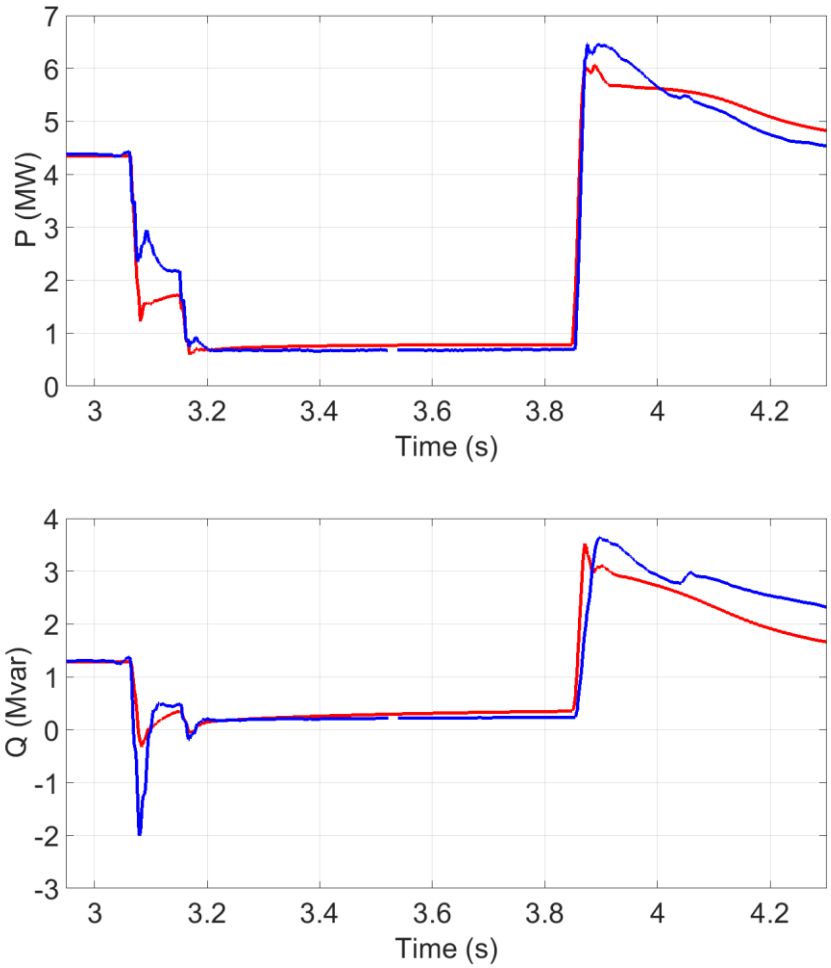

Figure 4.34 Simulated active and reactive powers (red) vs. measurement (blue), residential load case study, event 1

4.5.4.2 **Event 2**

The second voltage sag event is also related to the network of Figure 4.29 but at a different time, 16:17 April 4th , 2020. This fault lasted for 0.7 seconds and caused the following voltage drops: 52.8% voltage drop on phase a, 53.5% voltage drop on phase b, and 54.7% voltage drop on phase c. In the same way as Event 1, the actual measured voltages were reproduced by simulating Figure 4.29 and imposing faults on the distribution bus. In this case study, the fault on phase "a" has started 12 cycles after the two other phases. Figure 4.35 presents the recorded and simulated voltage waveforms.

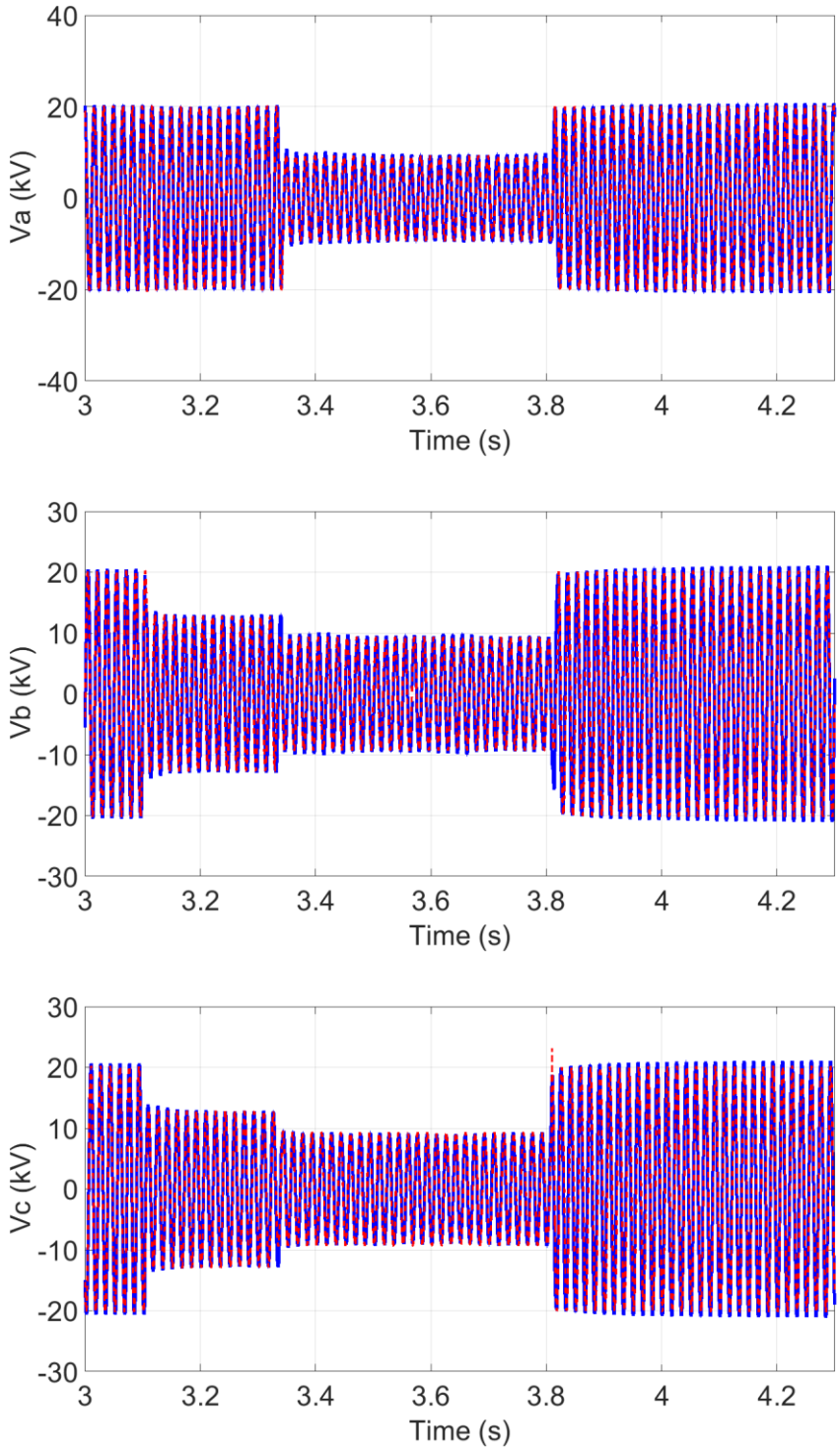

Figure 4.35 Three-phase voltages; simulation (dotted) vs. measurement (solid), residential load case study, event 2

The DM has the following input data:

- Voltage level at the load bus is 25 kV.
- Total active power: the recorded pre-fault power demand of the load is 7 MW.
- Load composition: at the time of this event (i.e.,16:17), unlike Event 1, some contribution should be expected from the industrial load. Since no detail was available on the power consumption of the industrial consumer, measured signals were used to derive this information. The recorded active powers in Figure 4.36 i.e., post-fault power of 5.5 MW versus 7 MW pre-fault power, show 1.5 MW load loss as the result of the voltage sag. This observation is an indication of the presence of 1.5 MW industrial motors which have been tripped during the fault. Therefore, the load mix is taken as being made up of 21% industrial motors and 79% residential loads. The residential load composition is assumed as Table 4.9 based on the information provided in [46] with some minor adjustments made to match the measured signals as closely as possible.

Table 4.9 Load composition of the residential load, event 2

Load Component	**Composition**
Incandescent	1.5%
CFL	3.5%
TV+PC	30%
Refrigerator	15%
Dish Washer	5%
Cloth Washer	5%
Dryer	10%
Cooking	20%
Water Heater	10%

- Percentage of drive-controlled motors: residential load composition does not include any directly connected or drive-controlled three-phase motors.
- Parameters of the industrial motors are taken from [7] and listed in Table 4.10. To account for the 1.5 MW load loss, these motors were tripped 3 cycles after the beginning of the voltage sag.

Table 4.10 Small industrial motor parameters

R_s (pu)	X_s (pu)	X_m (pu)	R_r (pu)	X_r (pu)	H	Load factor
0.078	0.065	2.67	0.044	0.049	0.5	0.6

Simulation results of the network presented in Figure 4.29 using the tuned DM for the residential load are presented in Figure 4.37 for three-phase currents and Figure 4.36 for active and reactive power. It is observed that the measured and simulated responses match with sufficient accuracy.

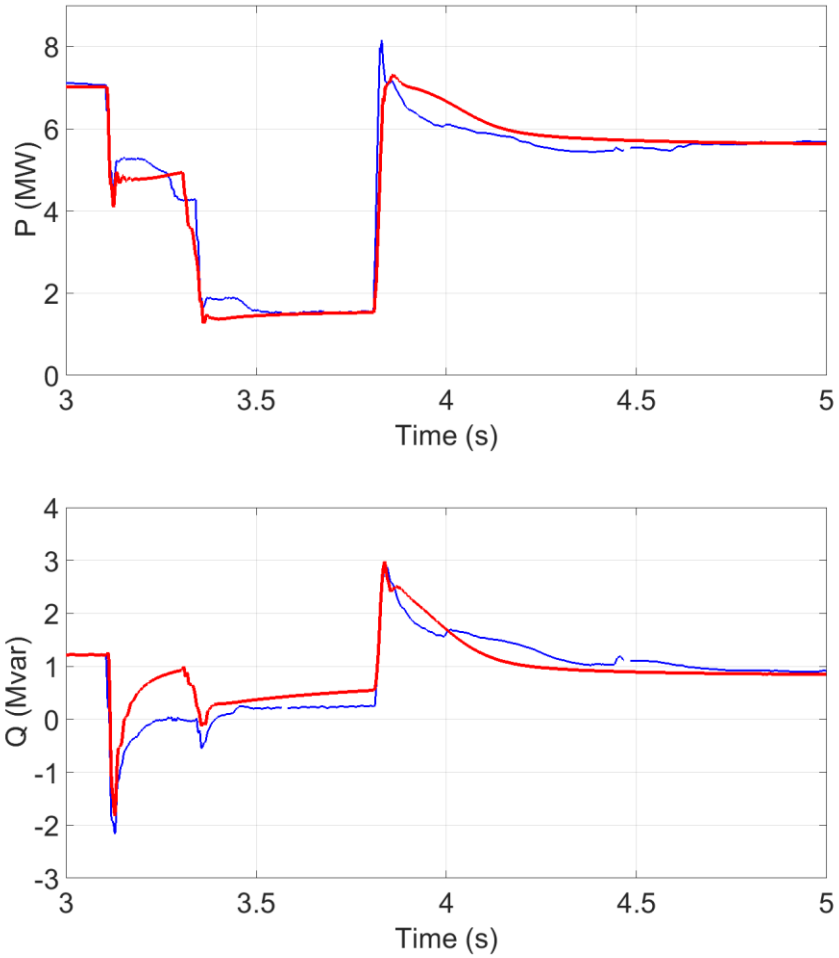

Figure 4.36 Simulated active and reactive powers (red) vs. measurement (blue), residential load case study, event 2

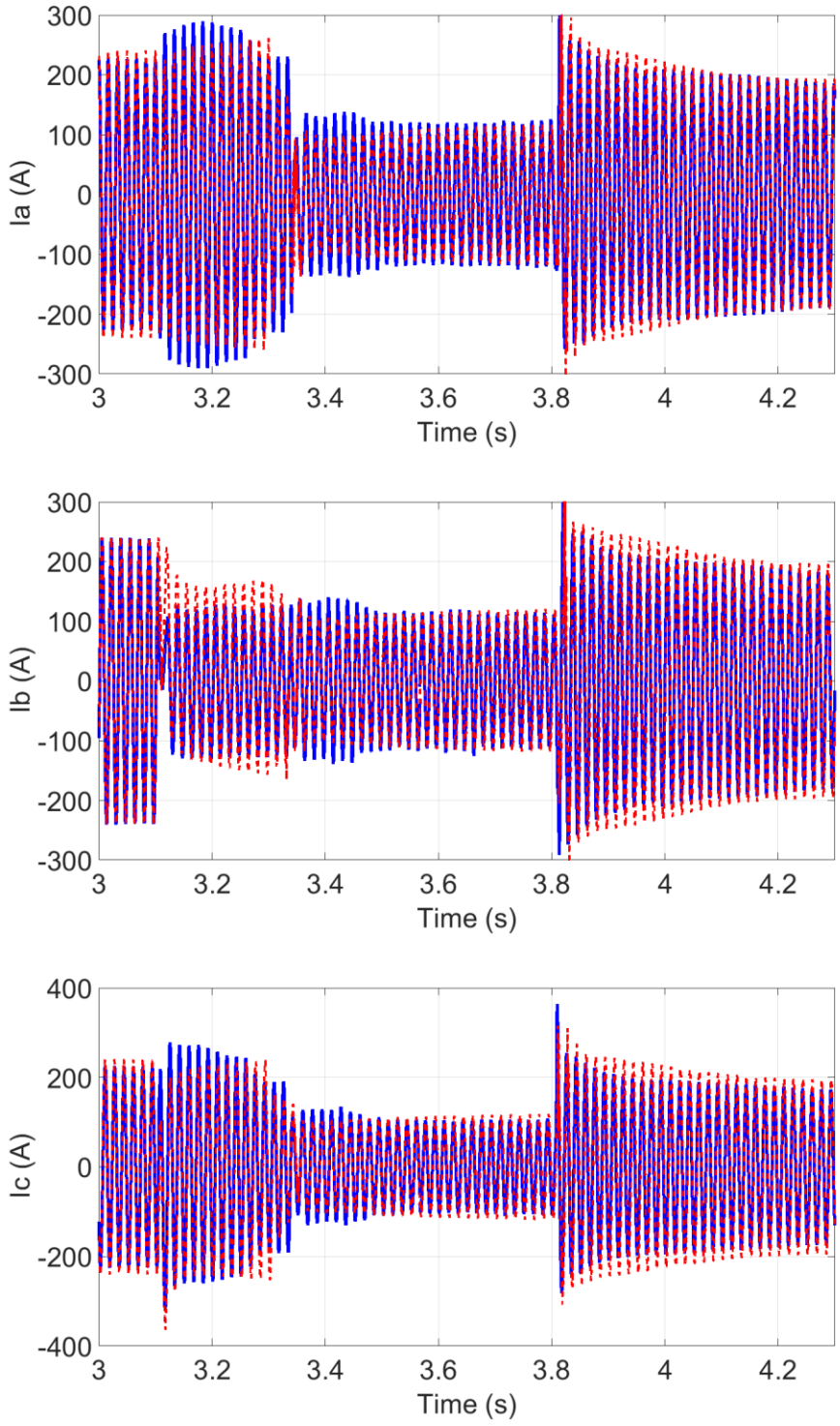

Figure 4.37 Three-phase currents, simulation (dotted) vs. measurement (solid), residential load case study, event 2

4.6 Summary

This chapter presents the new aggregated EMT-type detailed load model (DM) developed using the component-based approach. This model is capable of accounting for nonlinear devices (i.e., power electronics), single-phase loads (e.g., single-phase motors) and unbalanced conditions (e.g., asymmetrical faults). It offers higher accuracy and can provide a more realistic description of load behavior compared to the existing models.

The static characteristic of the DM is validated and its significance in dynamic studies for capturing load behaviour compared to traditional static modeling is highlighted. Moreover, the dynamic performance of the DM is assessed by simulating load behaviour in voltage sag events in different load sectors and comparing the results with recorded data. Model validation studies have shown that the load model can be tuned to reproduce almost accurately the shape of the recorded waveforms. This observation verifies that the model can be utilized for predicting the behaviors of similar loads even in cases with large voltage variations or unbalanced faults.

When using the DM in power system simulation, information about the load mix is required. If knowledge on the real composition of the modeled load is available, the model can predict load behaviour more accurately. Nevertheless, when there is lack of such information, load composition maybe extracted from existing literature or statistics and in some cases, estimations can be made. Simulation results illustrated that even sufficiently accurate compositions can predict the actual measured responses of loads with no significant error. All circumstantial data (i.e., geographical location, time, temperature, etc.) should be taken into account to come up with the best estimate of the load composition. Nevertheless, load component data will always have some uncertainty no matter how hard one tries to obtain this information.

Furthermore, the application of the measurement-based approach to the component-based model demonstrated the benefits of using both methodologies. When measured field data are available, the load model can be refined by adjusting the compositions or finding additional features of load components such as motor tripping patterns during a voltage sag. Adding these features to the DM not only provides a more realistic representation of load, but also offers some insight into general considerations when modeling similar types of loads in power system studies. Recently, number

of various measurement devices in power systems have substantially increased. This opens a possibility for the capture of data required for load modelling.

It is worth mentioning that the proposed load model, the identified load compositions of different load sectors, as well as the characteristics of different components were obtained and validated through real case studies. Therefore, they can be referred to in studies involving similar types of loads.

CHAPTER 5 LOAD MODELING IN HARMONIC STUDIES

Frequency domain modeling of the load is an important element for accurate evaluation of the harmonic impedance of a network. Loads have a considerable influence on the harmonic impedance in terms of location of resonances and level of damping, Therefore, their appropriate modelling is an important consideration and is becoming even more important due to the increasing number of HVDC interconnectors, wind power plants, PV-based generation and large-scale integration of power electronic based distributed generation.

Various common load models for the purpose of harmonic studies were presented in section 2.4. The selected load model has a great impact on the simulation results. Influence of the type of the load model on simulation results of frequency and damping of system resonance has been reported in [34]. In a similar case study on the CIGRE 14-Bus system model, the distinct characteristics of various harmonic load models have been illustrated and compared [35]. Nevertheless, the adequacy of existing models to realistically capture the impact of loads in harmonic studies is not fully covered in the literature. More detailed load models are required to identify whether extra modeling efforts are required, and under which circumstances such efforts are justified.

In this chapter, the detailed model of one feeder of an existing underground distribution network is developed. The harmonic impedance of this network is derived from time-domain computations using EMTP. Simulations are performed to investigate the effect of detailed load modeling on the harmonic impedance and to introduce errors caused by conventional models. The remainder of this chapter focuses on the impact of cables and different values of reactive power compensation on the harmonic impedance, which in turn provides some new guidelines for modeling underground distribution systems in harmonic studies.

5.1 Description of the test network

The developed detailed model (DM) as shown in Figure 4.1, was validated in Chapter 4 and is now used to study the frequency response of loads in an existing distribution network. Dorchester is a 120/12.47 kV substation which supplies residential and commercial consumers in an underground distribution network in downtown Montreal. One outgoing feeder of this substation, as shown in Figure 5.1, is selected to be modeled in detail for the purpose of frequency analysis. In this

schematic, the low voltage part of the feeder includes cables and residential/commercial consumers as elaborated in Figure 5.2. In this figure, the red boxes are commercial consumers, blue boxes are residential consumers and small white boxes are cable. Contents of each box is further described in section 5.2.

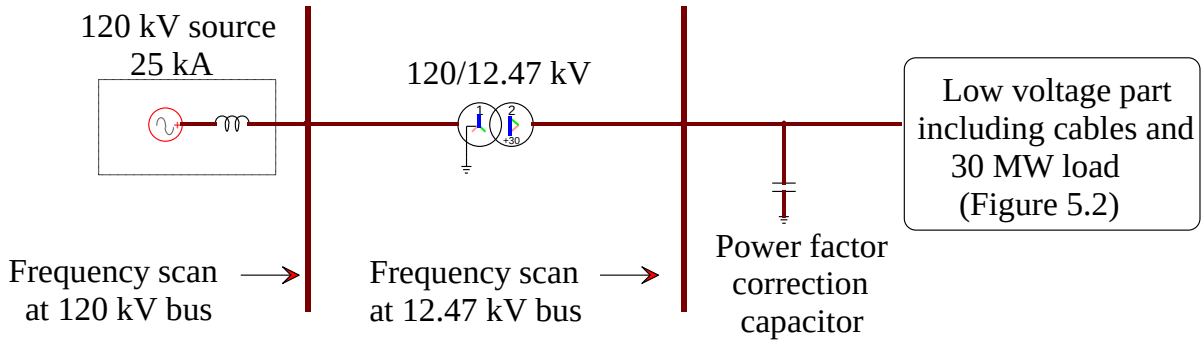

Figure 5.1 Schematic of the test network, one feeder of Dorchester distribution network

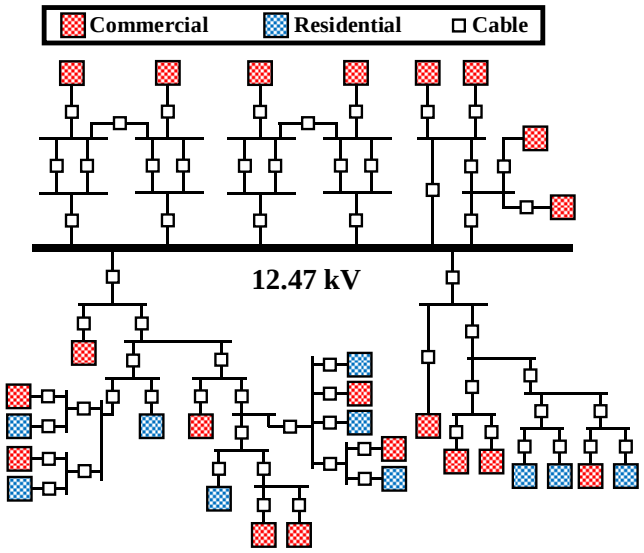

Figure 5.2 Low voltage part of the test network of Figure 5.1, modeled in detail

The previous circuit is patterned from the network model currently developed in CYMDIST [96], see Figure 5.3, a software used by Hydro-Quebec distribution division. From this model it is possible to extract information on the schematic of feeders, arrangement of cables, and location of load, as well as the following details:

- type of each load (residential or commercial)

- load power demand
- load power factor
- length of each cable section
- positive/zero sequence impedance of each cable section

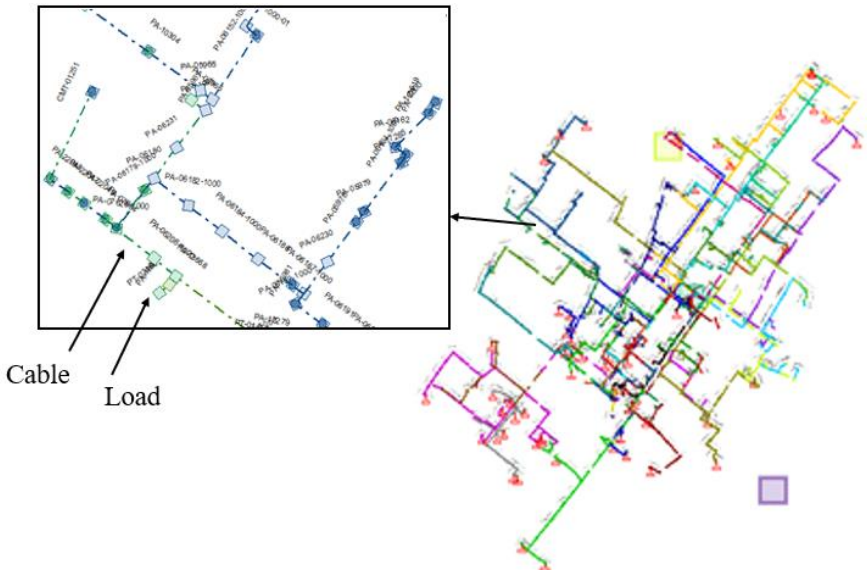

Figure 5.3 Test network model in CYMDIST

5.2 EMTP model of the test network

Figure 5.1 was implemented in EMTP (refer to *"Dorchester"* EMTP file) , considering the following points for the low voltage part as shown in Figure 5.2:

- Loads: each commercial/residential load is represented by its designated DM. It means that each red and blue box in Figure 5.2 is a tuned DM subcircuit as depicted in Figure 4.1. Although CYMDIST model provides power demand of loads as one of the required input parameters for DM (Table 4.2), no information is available on the load compositions. For this purpose, the compositions listed in Table 4.3 and Table 4.4 were used. With those compositions, the deducted power factors of residential/commercial loads are close to the presented values in CYMDIST (in the range 0.96-0.97). This is an indication that the considered load compositions in the two tables are sufficiently accurate

- Cables: the main concerns about modeling cables are the frequency-dependency of the per-unit length series impedance, and the distributed-parameter nature [90], [97]. In our case study, 2 km is the maximum length of 12.47 kV cable sections. Figure 5.7 illustrates a comparison between the frequency response of a 2 km cable modeled by a frequency dependent model (Wideband [98]) and a PI equivalent. It can be observed that for the considered length and in the frequency range of our interest (up to 3 kHz), there is no significant difference between a Wideband and a PI equivalent in terms of harmonic impedance. Therefore, in this thesis, cables are represented by PI equivalents. Information required for each model was extracted from the CYMDIST model and are shown in Figure 5.4 and Figure 5.6. Cross section of the utilized cable for Wideband model is depicted in Figure 5.5.

Geometrical and electrical data

Cable data

Cable type: Single core — Number of cables: 3

Cross-bond the Sheaths ☐

	Cable Number	Number of conductors	Vertical Distance (m)	Horizontal Distance (m)	Outer Insulation Radius (m)
1	1	2	1.1	0.0	0.019779
2	2	2	1.1	0.25	0.019779
3	3	2	1.1	0.5	0.019779

Conductor/Insulator data

	Cable Number	Conductor Number	Inside Radius Rin [m]	Outside Radius Rout [m]	Resistivity Rho [Ohm-m]	Relative Permeability MUE	Insulator Relative Permeability MUE-IN	Insulator Relative Permittivity EPS-IN	Insulator Loss Factor LFCT-IN	Phase Number KPH
1	1	1	0	0.006731	0.17e-7	1	1	3.88	0.001	1
2	1	2	0.011779	0.012795	0.21e-6	1	1	2.0	0.001	2
3	2	1	0	0.006731	0.17e-7	1	1	3.88	0.001	3
4	2	2	0.011779	0.012795	0.21e-6	1	1	2.0	0.001	4
5	3	1	0	0.006731	0.17e-7	1	1	3.88	0.001	5
6	3	2	0.011779	0.012795	0.21e-6	1	1	2.0	0.001	6

Figure 5.4 Cable parameters for Wideband model

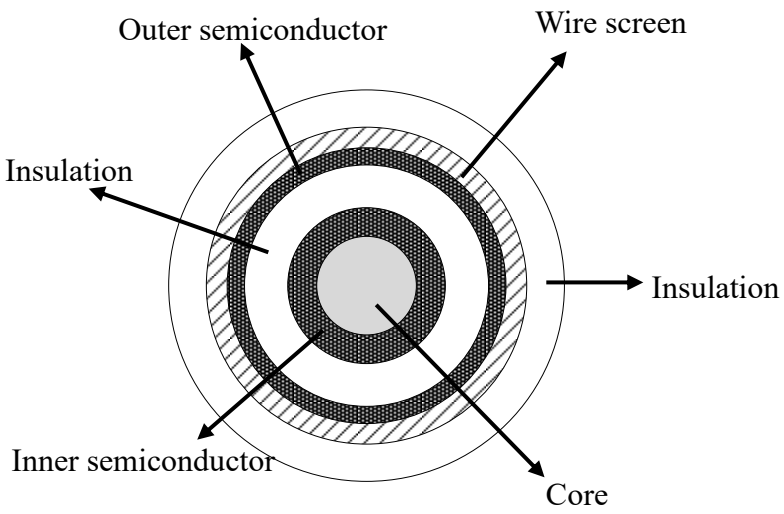

Figure 5.5 Cross section of a single core cable for Wideband model

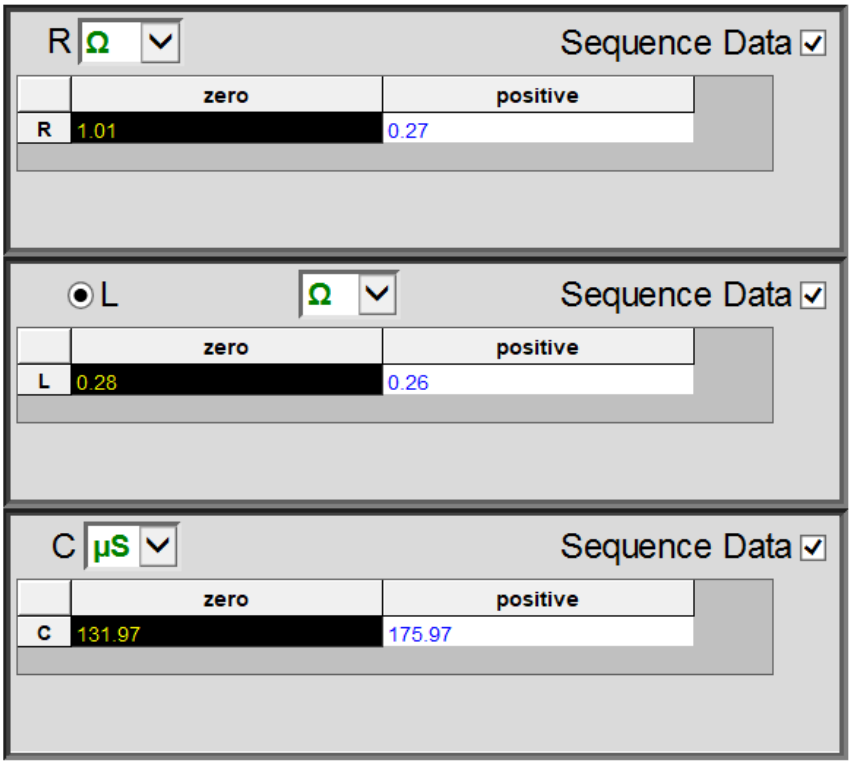

Figure 5.6 Cable parameters for PI model

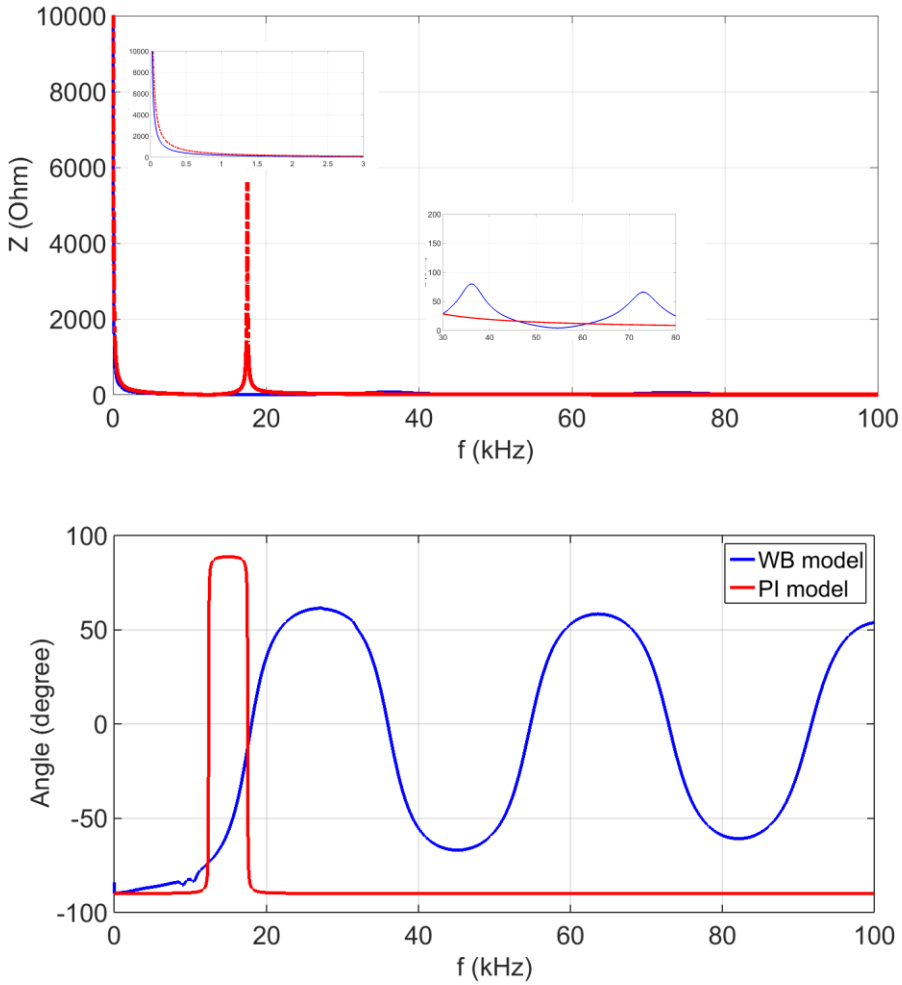

Figure 5.7 Comparison of magnitude and phase angle of the harmonic impedance of Wideband and PI model

5.3 Frequency response

A detailed frequency analysis was conducted on the test network (Figure 5.1) to investigate two different points. First, the impact of the type of load model (DM or simplified RL) on the harmonic impedance seen from different voltage levels and different values of reactive power compensation considered for the network. Second, the impact of cables on the harmonic impedance at different voltage levels and different values of reactive power compensation. The former aims to identify the cases where detailed or simplified load models are each applicable to the load. The latter will

provide some generic information on modeling underground distribution systems in harmonic studies.

The frequency scan is performed in time-domain due to the presence of nonlinearities (power electronics, controls…). The scanning method is available in EMTP and uses a perturbation approach [21] by injecting a current for each frequency on the bus of interest and extracting the corresponding harmonic voltage for calculating harmonic impedance. The studied range of frequencies is from 50 Hz to 3 kHz with a step of 1 Hz.

5.3.1 Frequency scan from 12.47 kV bus

The harmonic impedance as seen from the 12.47 kV bus (load bus) is shown in Figure 5.8, for three different values of reactive power compensation, i.e., different values attributed to the capacitor bank placed at the 12.47 kV bus: no reactive power compensation, 15% reactive power compensation and 30% reactive power compensation (refer to ”*Dorchester_LowVoltageScan”* EMTP file). It is observed that in the compensated cases and for frequencies higher than 500 Hz, the impedance seen from 12.47 kV bus eventually becomes the impedance of the capacitor bank. This implies that the load is bypassed by the capacitor bank for frequencies higher than 500 Hz. So, to obtain the harmonic impedance of a compensated underground distribution systems seen from the load bus, an equivalent RL combination can be an acceptable representation of load at frequencies higher than 500 Hz. For lower frequencies, the DM is suggested. For further verification, the DM was replaced by an equivalent series RL model representing the same active and reactive powers. The results are compared in Figure 5.9 for the case of 30% reactive power compensation. The differences are noticeable at frequencies below 500 Hz.

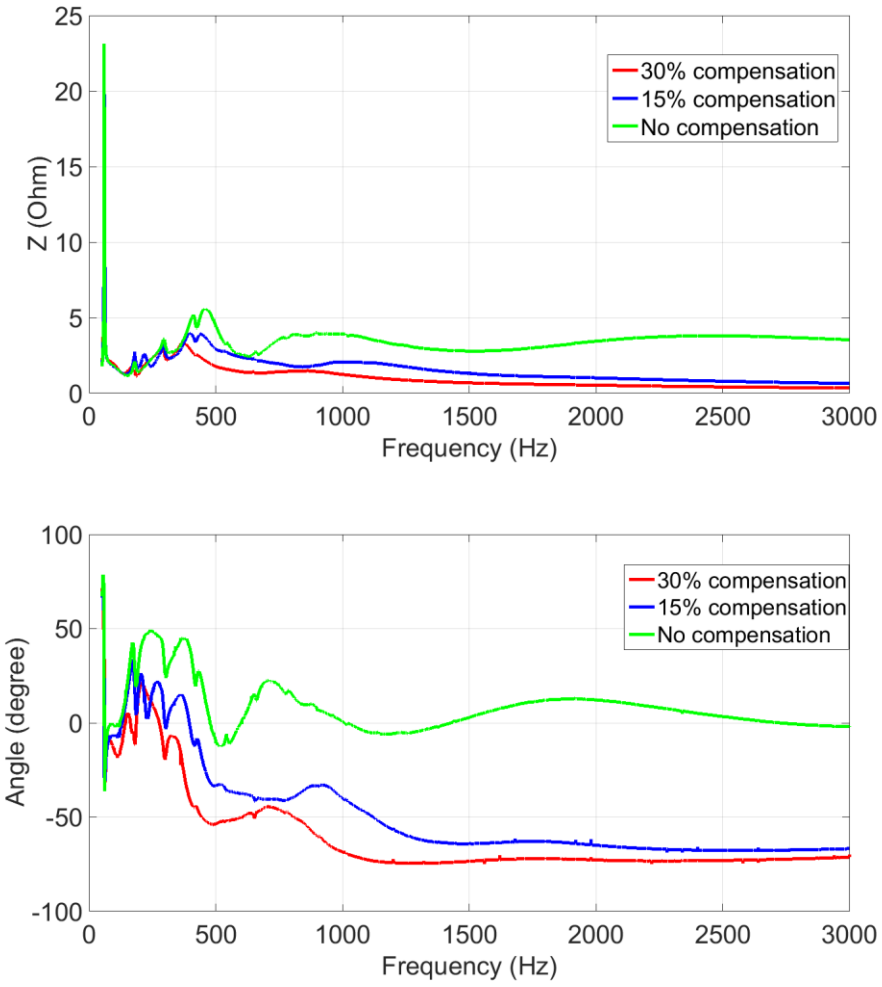

Figure 5.8 Magnitude and phase angle of harmonic impedance seen from the 12.47 kV bus

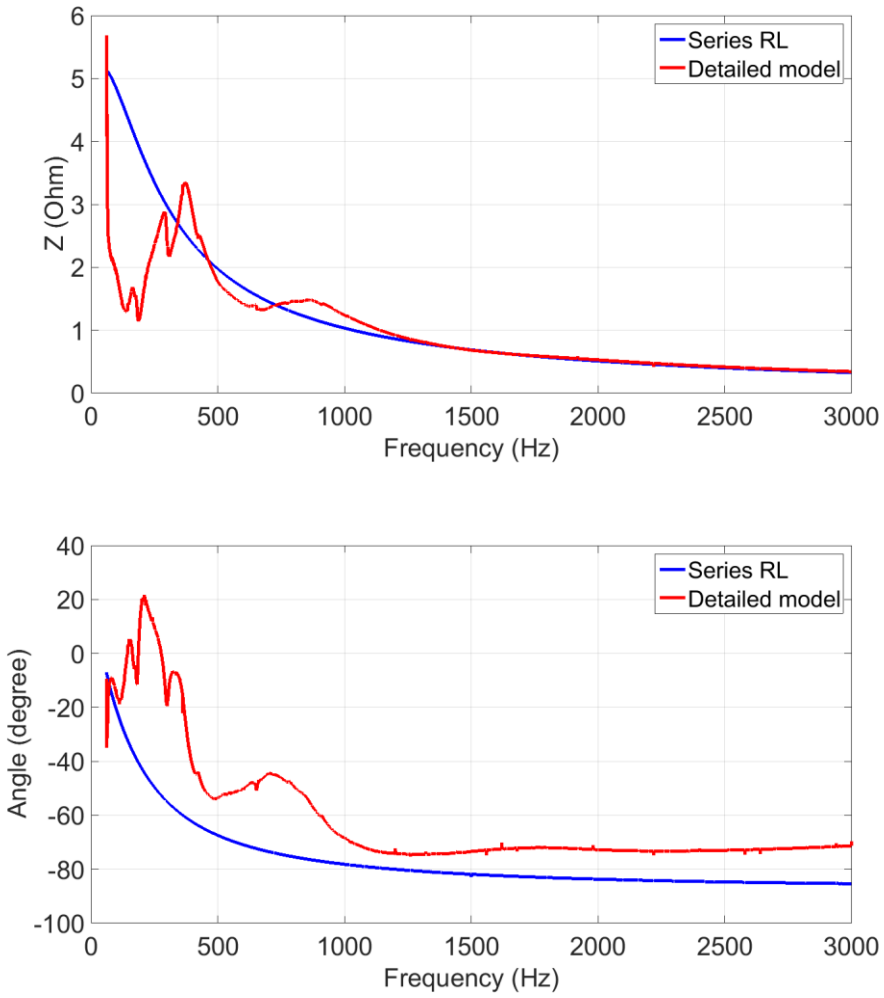

Figure 5.9 Magnitude and phase angle of harmonic impedance seen from the 12.47 kV bus, load model comparison

5.3.2 Frequency Scan from 120 kV bus

The harmonic impedance seen from the 120 kV bus (high voltage bus) is displayed in Figure 5.10, again for three reactive power compensation scenarios, no reactive power compensation, 15% reactive power compensation and 30% reactive power compensation (refer to ”*Dorchester_HighVoltageScan”* EMTP file). In this case, for frequencies higher than 500 Hz, the harmonic impedance is dominated by the leakage impedance of the transformer plus the impedance of the capacitor bank for the compensated cases. So, to obtain the harmonic impedance of an underground distribution systems seen from the high voltage bus, an equivalent RL combination

can be an acceptable representation of load at frequencies higher than 500 Hz. For lower frequencies, the DM is suggested. In the same way as the previous section, the comparison between the DM and the equivalent RL model for 30% reactive power compensation is shown in Figure 5.11. The results verify that an equivalent RL combination is an acceptable representation of the load for frequencies higher than 500 Hz.

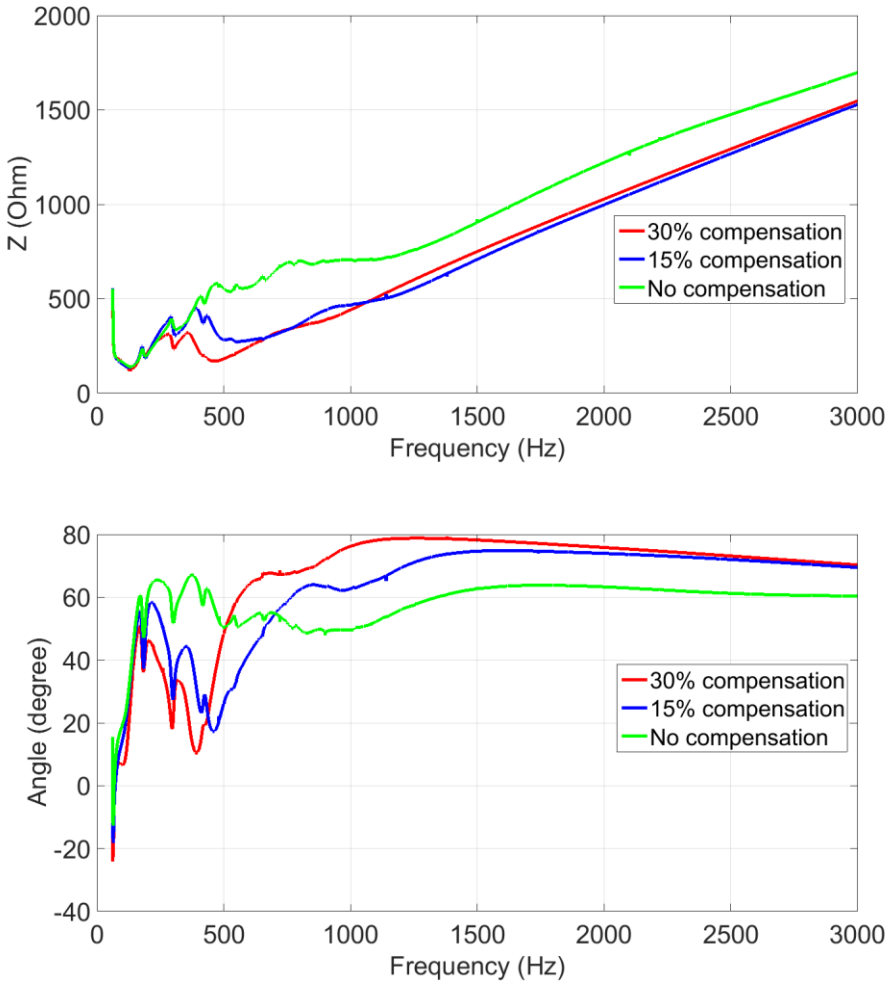

Figure 5.10 Magnitude and phase angle of harmonic impedance seen from the 120 kV bus

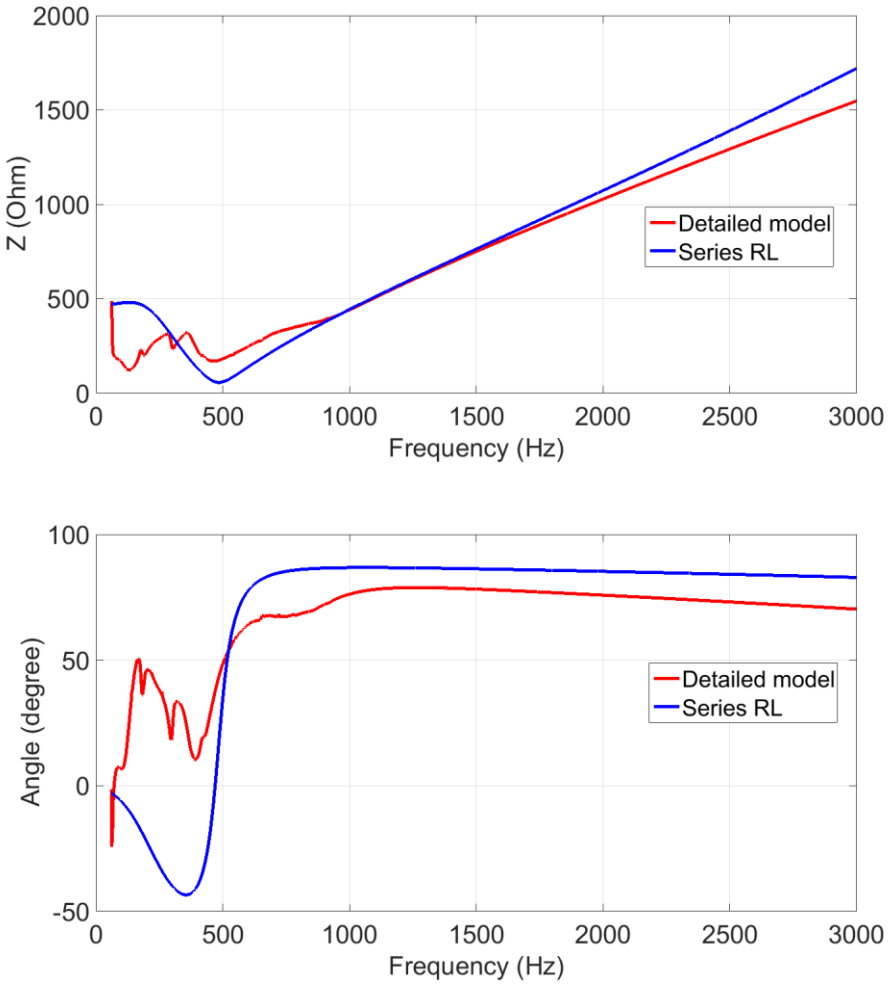

Figure 5.11 Magnitude and phase angle of harmonic impedance seen from the 120 kV bus, load model comparison

5.4 Effect of cables on the frequency response

In this section, the impact of the presence of cables on the frequency response at different voltage levels, with and without reactive power compensation is presented. For this purpose, all cables as shown in Figure 5.2 were removed, and loads were directly connected to the low voltage bus (refer to ”*Dorchester_LowVoltageScan_NoCable”* EMTP file). The resulted harmonic impedance was compared to the original network with cables. Figure 5.12 and Figure 5.13 present the comparative harmonic impedances as seen from 12.47 kV bus, in two cases of no reactive power compensation and 30% reactive power compensation, respectively. It is observed that presence of cables has a

significant impact on the frequency response of the uncompensated case. This highlights the importance of including cables when simulating the harmonic impedance of an uncompensated underground distribution systems seen from the low voltage bus.

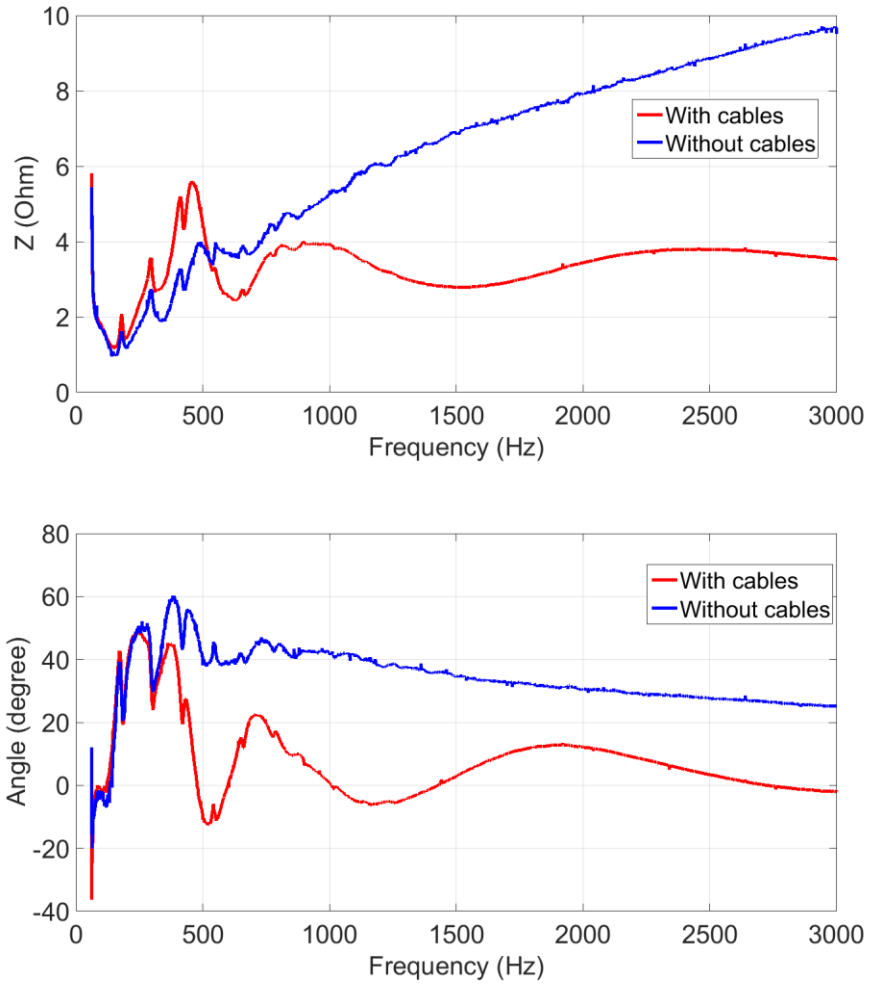

Figure 5.12 Effect of cables on magnitude and phase angle of harmonic impedance seen from the 12.47 kV bus, no compensation

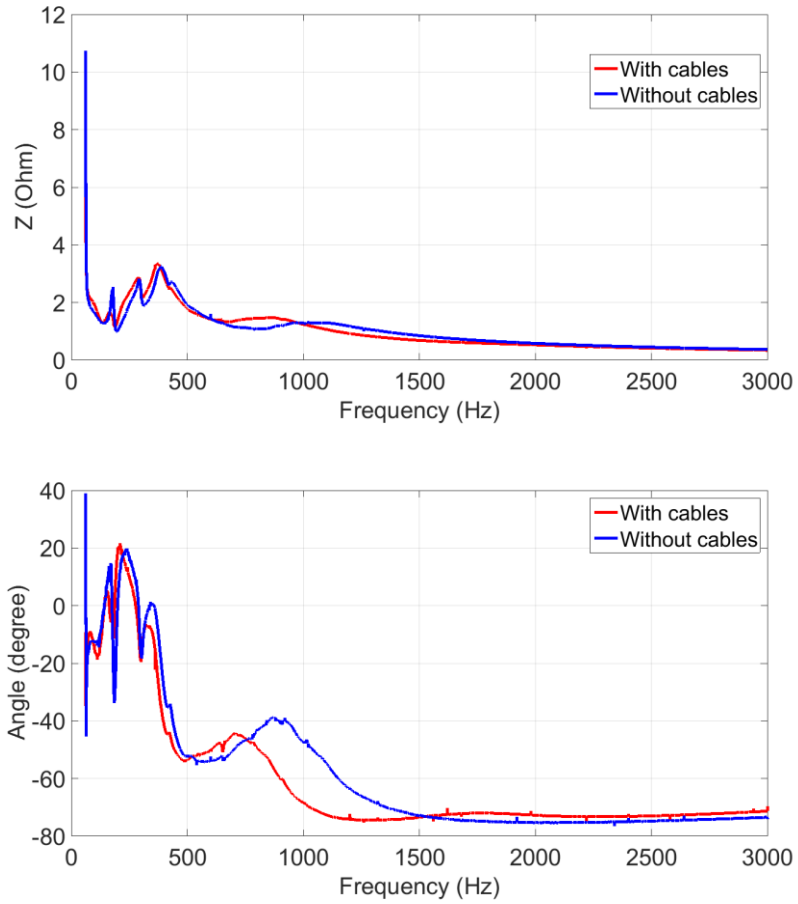

Figure 5.13 Effect of cables on magnitude and phase angle of harmonic impedance seen from the 12.47 kV bus, 30% compensation

The harmonic impedance seen from the 120 kV bus was obtained following a similar procedure and by adopting only the uncompensated case whose impedance as seen from the low voltage bus showed more sensitivity to the presence of cables (refer to "*Dorchester_HighVoltageScan_NoCable"* EMTP file). In Figure 5.14, the noticeable difference occurred by eliminating the cables (red curve vs blue curve) emphasizes on the importance of including cables when simulating the harmonic impedance of an uncompensated underground distribution systems seen from the high voltage bus.

The known layout of cables and their parameters made it possible to model them in detail in the presented case studies. However, this is not the case for majority of networks. So, it would be beneficial if instead of including all the cables, an equivalent capacitance representing them can be estimated and allocated at the considered bus. To this aim, the frequency response of the unloaded

feeder was obtained from the 12.47 kV bus. The capacitive part of this impedance represents the equivalent capacitance of all the cables. Considering that the capacitive part of this impedance dominates at low frequencies, the equivalent capacitance was found from the amplitude of this impedance at 60 Hz. In the green curve of Figure 5.14, all cables were removed and replaced by an equivalent 27 µF capacitance calculated as explained. The closeness of results to the case of actual cables (red curve), suggests that the considered capacitance can properly represent the cables. 27 µF capacitance per 30 MW of load in this case study can be interpreted as approximately 1 µF capacitance per 1 MW of load. This value, which corresponds to 3.5 Mvar per 60 MW of load, is close to the typical value presented by Scottish Power, i.e., 2.8 Mvar per 60 MW [35]. This comparison further verifies that the assumed capacitance is an appropriate representation of cables for modeling underground distribution systems.

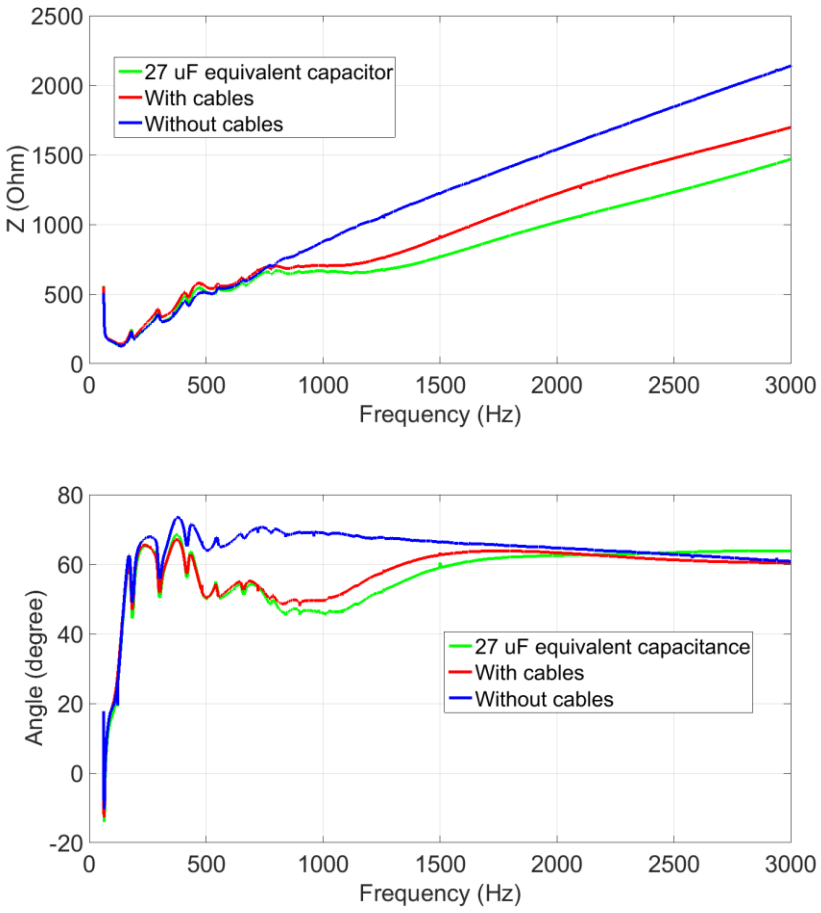

Figure 5.14 Effect of cables on magnitude and phase angle of harmonic impedance seen from the 120 kV bus

5.5 Summary

In this chapter the application of the developed detailed model to study the frequency response of the load is discussed. An existing underground distribution system was used as the test network and the harmonic impedance was derived in different scenarios. Simulation results identified the conditions of the network in which detailed or simplified load models are applicable to loads in harmonic studies. Furthermore, available data on the existing network provided the opportunity to introduce some general rules for modeling cables in underground distribution systems for the purpose of harmonic studies.

CHAPTER 6 CONCLUSION

6.1 Summary of thesis

The main objective of this thesis was to develop a new load model which reproduces the real load behavior both in dynamic and harmonic simulations. A detailed component-based EMT-type load model is developed to provide an accurate representation of the reality of aggregated loads. Individual EMT-type models of load components from various load categories are first developed and next aggregated to a top level to form an aggregated detailed load model. The developed model is the first EMT-type aggregated load model presented in the literature and is a generic and flexible load representation which can be tuned to represent different types of loads and reproduce their behaviour in dynamic and harmonic power system simulations. The important remarks of this thesis are summarized in the following categories:

- On the need for new load models in dynamic simulations

Static models are current practice in most dynamic studies. However, based on the investigations presented in this thesis, static models are not sufficient to reproduce the load behavior in dynamic simulations. Detailed composite load modeling is not usually preferred mainly due to excessive data requirements, modeling efforts, and computational burden. However, the obtained results in this thesis justify investing time and effort into such detailed modelling. Majority of existing composite load models are simple models including limited load components which can not be a representative of the actual aggregated loads. The most detailed existing composite load model as well, can not realistically capture the load behaviour. This is because it is a positive sequence model and therefore, models of single-phase loads such as single-phase motors can not be accurately incorporated. A static algebraic approximation is included for modeling those motors. Based on the results presented in this thesis, dynamics of single-phase motors during and following a fault have a considerable effect on the load response especially in residential load sector where this type of motor is dominant. So, it is important to have a precise model for single-phase motors. Another disadvantage of a positive sequence model is that it can not accurately deal with unbalanced faults in the network. The calculations are only based on positive sequence components without taking into account the zero sequence and negative sequence. As the result, the response of the load during

unbalanced faults can not be captured correctly. Another drawback of existing composite load models is that generally they do not incorporate power electronics; even in the more sophisticated model, approximate equivalents are used to represent this load category. Power electronics are increasingly becoming popular at all levels of the end-use load spectrum, from motor drives to small consumer electronics. Therefore, modifications must be made to improve their modeling to satisfy the requirements for analysis of modern power systems.

- Development of a new detailed EMT-type component-based load model

To overcome the existing limitations, this thesis presents a new EMT-type component-based load model. The EMT-type model is based on the representation of the actual electrical circuit equivalent of the load components. It is implemented in EMTP where network equation formulation is accomplished using nodal analysis, and numerical integration technique is applied to solve them. Therefore, this model is capable of accounting for nonlinearities (i.e., power electronics), single-phase loads (e.g., single-phase motors) and unbalanced conditions (i.e., asymmetrical faults). It fills the gap in the literature and provides a more realistic simulation of load behaviour. Another advantage of this model is that since the EMT-type model is able to represent the actual circuit of loads, it is more general than traditional models. Most of the existing load model forms are able to represent load characteristics for only one type of power system analysis. For example, static models in steady-state analysis only represent information on the active and reactive power demands and do not contain any information on the harmonic emissions of power system loads. The presented model on the other hand, can be used in different studies and also allows the electrical characteristics of the modelled load to be extracted and converted into a required load model form. This is because the circuit-based model offers the possibility of reproducing the instantaneous input current waveform and hence the active and reactive power waveforms. By analyzing the waveforms, any required information on load characteristic can be extracted. For example, in a case study of this thesis, the developed model is converted to a static model (exponential model) which makes it suitable for steady-state analysis. In several other case studies, harmonic characteristics of the load in different load sectors is extracted.

- Application and validation of the developed model

The developed model is used to simulate load behavior in case studies related to voltage sag events in different load sectors and is validated against field data during those events. Validation of the performance of the model in real cases is an important stage of load model development which is required to ensure the efficacy of the proposed model in reproducing the measured dynamic behavior of loads during and following a disturbance. Hydro-Quebec has recorded a number of disturbances and events at representative feeders on the network which provides useful information for validating the proposed model. Model validation studies have shown that the proposed load model can reproduce almost accurately the shape of the recorded waveforms in different events and load sectors. This observation further implies that the presented model can overcome the limitations of existing models in three ways. First, the model includes the dynamic model of single-phase motors, so the load response is correctly captured especially in residential load sector in which these types of motors are dominant. Second, the model includes detailed model of power electronic load components, so the harmonic contents of the load can be predicted adequately. Finally, the model can account for unbalanced network conditions, so it produces the dynamic behaviors of loads in cases with unbalanced faults. Generally, the detailed EMT nature of the model yields a load representation which is close to the reality of the aggregated loads.

- Information about the load composition

When using the proposed component-based model in power system studies, information about the load composition is required. If knowledge on the real composition of the modeled load is available, the model can predict load behaviour more accurately. Nevertheless, when there is lack of such information, load composition maybe extracted from existing literature or statistics or even in some cases, estimations can be made. Simulation results illustrates that even sufficiently accurate compositions can predict the actual measured responses of loads with no significant error. All circumstantial data (i.e., geographical location, time, temperature, etc.) should be taken into account to come up with the best estimate of the load composition. Nevertheless, load component data will always have some uncertainty.

- Combination of measurement-based and component-base approaches

The combination of measurement-based and component-based load modeling approaches is another important point of this work that brings together the individual strengths of the two approaches. The measured data provided by Hydro-Quebec not only is used for model validation, but also to derive additional characteristics of the modelled loads, e.g., percentage contribution of drive-controlled motors in the load mix, connection or reconnection pattern of motor loads during and following voltage sags and load torque characteristics of single-phase motors. Those characteristics are added to the developed model to complement it. Not only a more realistic representation of the load is obtained, but also some insight into general considerations for modeling similar types of loads is provided.

- On the need for new load models in harmonic simulations and new guidelines for modeling underground distribution systems in harmonic studies

In harmonic studies, loads are often represented by simplified linear equivalents. The adequacy of those models and the importance of the detailed load model in capturing real load behavior in harmonic simulations is investigated. The proposed model is used to produce the detailed model of one feeder of an existing underground distribution network. Results of several frequency analyses on the test network shows that depending on the voltage level, frequency range of interest, and level of reactive power compensation in the network, different models (detailed or simplified) are applicable for loads.

Simulating an existing network has also provided an opportunity to introduce some new guidelines on modeling typical underground distribution systems for the purpose of harmonic studies. It is illustrated that the importance of considering cables for accurate representation of the network in harmonic studies depends on the presence of the reactive power compensation; cables have major influence on networks with no reactive power compensation and so should be considered when modeling such networks.

6.2 List of publications

M. Torabi Milani, B. Khodabakhchian, J. Mahseredjian, and K. Sheshyekani. "Development and validation of a new detailed EMT-type component-based load model," Electric Power Systems Research, Volume 197 (2021).

M. Torabi Milani, B. Khodabakhchian and J. Mahseredjian. "Detailed EMT-type load modeling for power system dynamic and harmonic studies, " submitted to IEEE Transactions on Power Delivery.

6.3 Future works

This section summaries some of the key areas that were identified as potential extensions of the work presented in this thesis:

- Load types should be extended to include more possible variations within the load categories. Examples are SMPS with no PFC (monitors, laptops, and DVD/CD/video loads), microwaves and different types of single-phase IM (split-phase, capacitor start, and capacitor start-capacitor run).
- Load sectors are likely to undergo changes in load types participating in the load mix in the future. Electric vehicle battery chargers are likely to become a more common load within the network. Another example is drive-controlled single-phase IMs which may not be currently widespread, but their use is expected to increase in the future. Furthermore, large scale integration of small generation units and Distributed Generation (DG) may impact load behavior in future power networks. These scenarios call for the development of appropriate load models for correct representation of future load mix and extension of the aggregation methodology to include the effect of DG in aggregate load model.
- Although system loads are typically classified in one of the three general load sectors (residential, commercial and industrial), they should be further divided into sub-sectors. For instance, highly urban (high rise buildings) and urban (few story buildings) for residential sector and office/retail/education sub-sectors for commercial sector. This provides a more accurate description of the diversity in load structure, load composition and load profiles within each load sector. This is particularly true for large industrial load sector, as the industrial processes and activities performed at different sites are usually not comparable across the whole industrial load sector. Large industrial loads include paper mills, steel mills, petro-chemical plants, aluminum smelters.

- Artificial intelligence techniques can be exploited for efficient load model development. Examples are deep learning methods for parameter identification of load models, or the determination of load compositions as presented in [99], [100].

REFERENCES

[1] D. N. Kosterev, C. W. Taylor and W. A. Mittelstadt, "Model validation for the August 10, 1996 WSCC system outage," IEEE Transactions on Power Systems, vol. 14, no. 3, p. 967–979, 1999.

[2] W.-S. Kao, "The effect of load models on unstable low-frequency oscillation damping in Taipower system experience w/wo power system stabilizers," IEEE Transactions on Power Systems, vol. 16, no. 3, pp. 463-472, 2001.

[3] D. Han, J. Ma, R. He and Z.-Y. Dong, "A real application of measurement-based load modeling in large-scale power grids and its validation," IEEE Transactions on Power Systems, vol. 24, no. 4, pp. 1756-1764, 2009.

[4] J. Arrillaga, B. C. Smith, N. R. Watson and A. R. Wood, Power System Harmonic Analysis, New York: Wiley, 1997.

[5] E. Acha and M. Madrigal, Power system harmonics: computer modelling and analysis, Hoboken, NJ: Wiley, 2001.

[6] A. Medina., J. Segundo-Ramirez, P. Ribeiro, W. Xu, K. Lian., G. Chang., V. Dinavah. and N. Watson, "Harmonic analysis in frequency and time domain," IEEE Transactions on Power Delivery, vol. 28, no. 4, 2013.

[7] Working group C4.605, "Modelling and aggregation of loads in flexible power networks," Cigre, 2014.

[8] X. Qu, X. Li, J. Song and C. He, "An extended composite load model taking account of distribution network," IEEE Transactions on Power Systems, vol. 33, no. 6, pp. 7317-7320, 2018.

[9] B. Khodabakhchian and G.-T. Vuong, "Modeling a mixed residential-commercial load for simulations involving large disturbances," IEEE Transactions on Power Systems, vol. 12, pp. 791-796, 1997.

[10] IEEE task force on load representation, "Load representation for dynamic performance analysis (of power systems)," IEEE Transactions on Power Systems, vol. 8, no. 2, pp. 472-82, May 1993.

[11] NERC load modeling task force, "Technical reference document dynamic load modeling," 2016.

[12] X. Xie, Y. Sun, Q. Wang, Y. Li, Y. Zhang and L. Zhang, "A piecewise probabilistic harmonic model of aggregate residential loads," IEEE Transactions on Power Delivery, vol. 36, no. 2, pp. 841-852, 2021.

[13] P. Rodríguez-Pajarón, H. Mendonça and A. Hernàndez, "Nonlinear load modelling for harmonic analysis of aggregated residential loads with OpenDSS," 2020 19th International Conference on Harmonics and Quality of Power (ICHQP), pp. 1-6, 2020.

[14] G. Ye, M. Nijhuis, V. Cuk and J. F. G. Cobben, "Appliance-based residential harmonic load modelling," 2017 IEEE Manchester PowerTech, pp. 1-6, 2017.

[15] CIGRE JTF 36.05.02/14.03.03, "AC system modelling for AC filter design – an overview of impedance modelling," Electra 164, pp. 133-151, 1996.

[16] CIGRE WG 36-05, "Harmonics, characteristic parameters, methods of study, estimates of existing values in the network," Electra 77, July 1981.

[17] IEEE power engineering society task force, "Tutorial on harmonics modelling and simulation," TP-125-0, 1998.

[18] CIGRE WG CC-02 (CIGRE 36.05/CIRED 2), "Guide for assessing the network harmonic impedance," Electra No. 167, pp. 97-131, 1996.

[19] IEEE task force on harmonic modeling, "Impact of Aggregate Linear Load Modeling on Harmonic analysis: a comparison of common practice and analytical methods," IEEE Transactions on Power Delivery, vol. 18, no. 2, April 2003.

[20] J. Mahseredjian, S. Dennetière, L. Dubé, B. Khodabakhchian and L. Gérin-Lajoie, "On a new approach for the simulation of transients in power systems," Electric Power Systems Research, vol. 77, pp. 1514-1520, 2007.

[21] U. Karaagac, J. Mahseredjian, S. Jensen, R. Gagnon, M. Fecteau and I. Kocar, "Safe operation of DFIG-based wind parks in series-compensated systems," IEEE Transactions on Power Delivery, vol. 33, pp. 709-718, 2017.

[22] Y. Zhu, Power System Loads and Power System Stability, Springer Nature, 2020.

[23] J. R. Ribeiro and F. J. Lange, "A new aggregation method for determining composite load characteristics," IEEE Transactions on Power Apparatus and Systems, Vols. PAS-101, no. 8, August 1982.

[24] R. Shankar and P. Kundur, Power system stability and control II, New York: McGraw-Hill Books, 1994.

[25] D. J. Hill, "Nonlinear dynamic load models with recovery for voltage stability studies," IEEE Transactions on Power Systems, vol. 8, no. 1, February 1993.

[26] D. Karlsson and D. J. Hill, "Modelling and identification of nonlinear dynamic loads in power systems," IEEE Transactions on Power Systems, vol. 9, no. 1, pp. 157-166, 199.

[27] R. Balanathan, N. C. Pahalawaththa and U. D. Annakkage, "(1999). Undervoltage load shedding for induction motor dominant loads considering P, Q coupling," IEE Proceedings-Generation, Transmission and Distribution, pp. 146(4), 337-342, 1999.

[28] P. C. Krause, O. Wasynczuk, S. D. Sudhoff and S. D. Pekarek, Analysis of electric machinery and drive systems, John Wiley & Sons., 2013.

[29] L. Pereira, D. Kosterev, P. Mackin, D. Davies, J. Undrill and W. Zhu, "An interim dynamic induction motor model for stability studies in the WSCC," IEEE Transactions on Power Systems, vol. 17, no. 4, pp.1108-1115, 2002.

[30] H.-D. Chiang, J.-C. Wang, C.-T. Huang, Y.-T. Chen and C.-H. Huang, "Development of a dynamic ZIP-motor load model from on-line field measurements," International Journal of Electrical Power & Energy Systems, vol. 19, no. 7, pp. 459-468, 1997.

[31] H. Renmu, M. Jin and D. J. Hill, "Composite load modeling via measurement approach," IEEE Transactions on Power Systems, vol. 21, no. 2, pp. 663-672, May 2006.

[32] WECC, "Composite load model for dynamic simulations," WECC, [Online]. Available: https://www.wecc.org/Reliability/WECC%20MVWG%20Load%20Model%20Report%20ver%201%200.pdf.

[33] D. Kosterev, A. Meklin, J. Undrill, B. Lesieutre, W. Price, D. Chassin, R. Bravo and S. Yang, "Load modeling in power system studies: WECC progress update," in 2008 IEEE Power and Energy Society General Meeting - Conversion and Delivery of Electrical Energy in the 21st Century, pp. 1-8, 2008.

[34] R. Burch, G.-k. Chang, C. Hatziadoniu, M. Grady, Y. Liu and Marz. M et al, "Impact of aggregate linear load modeling on harmonic analysis: a comparison of common practice and analytical models," IEEE Transactions on Power Delivery, vol. 18, pp. 625-630, 2003.

[35] WG C4/B4.38, "Network modeling for harmonic studies," Cigre, 2017.

[36] IEEE PES harmonic working group, "Characteristics and modeling of harmonic sources power electronic devices," IEEE Transactions on Power Delivery, vol. 16, no. 4, October 2001.

[37] A. C. Henao-Muñoz and A. J. Saavedra-Montes, "Comparison of two mathematical models for nonlinear residential loads," In 2016 17th International Conference on Harmonics and Quality of Power (ICHQP), IEEE, pp. 1-6, October 2016.

[38] C. F. M. Almeida and N. Kagan, "Harmonic coupled Norton equivalent model for modeling harmonic-producing loads," In Proceedings of 14th International Conference on Harmonics and Quality of Power-ICHQP, IEEE, vol. September 2010, pp. 1-9.

[39] M. Bradt et al, "Harmonics and resonance issues in wind power plants," 2011 IEEE Power and Energy Society General Meeting, pp. 1-8, 2011.

[40] IEC, T. 61400-21-3, "Wind energy generation systems–Part 21-3: Measurement and assessment of electrical characteristics–Wind turbine harmonic model and its application," International Electrotechnical Commission, TC 88,ICS 28.180.

[41] W. W. Price, K. A. Wirgau, A. Murdoch, J. V. Mitsch, E. V. and a. M. El-Kady, "Load modeling for power flow and transient stability computer studies," IEEE Transactions on Power Systems, vol. 3, no. 1, pp. 180-187, 1988.

[42] EPRI, "Power quality monitoring data mining for power system load modeling," EPRI, [Online]. Available: https://www.epri.com/research/products/000000000001002185.

[43] S. Z. Zhu, Z. Y. Dong, K. P. Wong and Z. H. Wang, "Power system dynamic load identification and stability," PowerCon 2000. 2000 International Conference on Power System Technology, vol. 1, pp. 13-18.

[44] EPRI, "Measurement-based load modeling," EPRI, [Online]. Available: https://www.epri.com/research/products/1014402.

[45] B.-K. Choi, H.-D. Chiang, Y. Li and H. Li, "Measurement-based dynamic load models: Derivation, comparison, and validation," IEEE Transactions on Power Systems, vol. 21, no. 3, pp. 1276-1283, 2006.

[46] A. J. Collin, G. Tsagarakis and A. E. Kiprakis, "Development of low-voltage load models for the residential load sector," IEEE Transactions on Power Systems, vol. 29, no. 5, pp. 2180-2188, 2014.

[47] X. Liang, "A new composite load model structure for industrial facilities," IEEE Transactions on Industry Applications , vol. 52, no. 6, pp. 4601-4609, 2016.

[48] Siemens, "Siemens grid software products," Siemens, [Online]. Available: https://pss-store.siemens.com.

[49] GE Energy Consulting, "GE PSLF," GE Energy Consulting, [Online]. Available: https://www.geenergyconsulting.com/practice-area/software-products/pslf.

[50] L. M. Hajagos and B. Danai, "Laboratory measurements and models of modern loads and their effect on voltage stability studies," IEEE Transactions on Power Systems, vol. 13, pp. 584-592, 1998.

[51] C. Concordia and S. Ihara, "Load representation in power system stability studies," IEEE Transactions on Power Apparatus and Systems, no. 4, pp. 969-977, 1982.

[52] EPRI, "Advanced load modeling," EPRI, [Online]. Available: https://www.epri.com/research/products/000000000001007318.

[53] C. Cresswell, "Steady state load models for power system analysis," Ph.D dissertation, Dept. Elect. Eng, Univ. of Edinburg, Edindurg, 2009.

[54] A. J. Collin, "Advanced load modelling for power system studies," Ph.D dissertation, Dept. Elect. Eng. , Univ. of Edinburg, Edinburg, 2013.

[55] A. Mansoor, W. Grady, A. Chowdhury and M. Samotyi, "An investigation of harmonics attenuation and diversity among distributed single-phase power electronic loads," Proc of the 1994 Power Engineering Society Transmission and Distribution Conference, pp. 10–116, 1994.

[56] A. Mansoor, W. Grady, P. Staats, R. Thallam, M. Doyle and M. Samotyj, "Predicting the net harmonic currents produced by large numbers of distributed single-phase computer loads," IEEE Transactions on Power Delivery, vol. 10, no. 4, pp. 2001-2006, 1995.

[57] N. Lu, Y. Xie, Z. Huang, F. Puyleart and S. Yang, "Load component database of household appliances and small office equipment," IEEE Power and Energy Society General Meeting - Conversion and Delivery of Electrical Energy in the 21st Century, pp. 1-5, 2008.

[58] W. Carson, N. Taylor, N. Balu and D. Maratukulam, Power system voltage stability, McGraw-Hill, 1994.

[59] IEEE task force on load representation for dynamic, "Standard load models for power flow and dynamic performance simulation," IEEE Transactions on Power Systems, vol. 10, no. 3, pp. 1302-1313, 1995.

[60] U. Mader and P. Horn, " A dynamic model for the electrical characteristics of fluorescent lamps," Conference Record of the 1992 IEEE Industry Applications Society Annual Meeting, vol. 2, pp. 1928-1934, 1992.

[61] T. -.. Wu, J. -.. Hung and T. -.. Yu, "A PSpice model for fluorescent lamps operated at high frequencies," Proceedings of IECON '95 - 21st Annual Conference on IEEE Industrial Electronics, vol. 1, pp. 359-364, 1995.

[62] M. Sun and B. L. Hesterman, "PSpice high-frequency dynamic fluorescent lamp model," IEEE Transactions on Power Electronics, vol. 13, no. 2, pp. 261-272, 1998.

[63] N. Onishi, T. Shiomi, A. Okude and T. Yamauchi, "A fluorescent lamp model for high frequency wide range dimming electronic ballast simulation," APEC '99. Fourteenth Annual Applied Power Electronics Conference and Exposition, vol. 2, pp. 1001-1005, 1999.

[64] Y. Sun, "PSpice modeling of electronically ballasted compact fluorescent lamp systems," IEEE Industry Applications Conference Twenty-eighth IAS Annual Meeting, vol. 3, pp. 2311-2316, 1993.

[65] M. A. Shafi, R. A. McMahon and S. Weier, "Investigation of losses in commercially available self-resonant ballasts for compact fluorescent lamps," IEEE Power Electronics Specialists Conference, pp. 3100-3105, 2007.

[66] E. L. Corominas, J. M. Alonso, M. Rico-Secades, A. J. Calleja, J. Ribas and J. Cardesin, "Estimation of electrical characteristics of low power fluorescent lamps for optimized ballast design minimizing the number of lamp tests," IEEE Industry Applications Conference, vol. 5, pp. 3353-3360, 2000.

[67] M. Chen and Z. Qian, "A fluorescent lamp model based on its physical characteristics," The Fifth International Conference on Power Electronics and Drive Systems, vol. 2, pp. 1132-1136, 2003.

[68] S. Ben-Yaakov, M. Shvartsas and S. Glozman, "Statics and dynamics of fluorescent lamps operating at high frequency: modeling and simulation," Fourteenth Annual Applied Power Electronics Conference and Exposition, vol. 1, pp. 467-472, 1999.

[69] Onsemi, "Electronic lamp ballast design," Onsemi, [Online]. Available: http://www.onsemi.com/pub_link/Collateral/AN1543-D.pdf.

[70] "Electromagnetic compatibility (EMC) part 61000 3-2: Limits for harmonic current emissions (equipment input current less than 16 a per phase)," BS EN 61000-3-2, 2007.

[71] D. Gacio, J. Alonso, A. Calleja, J. Garcia and M. Rico-Secades, "Universal-input single-stage high power factor power supply for HB-LEDs based on integrated buck-flyback converter," IEEE Transactions on Industrial Electronics, vol. 58, no. 2, pp. 589-598, 2011.

[72] V. Roy, "Minimizing light flicker in LED lighting applications," Richtek Application Note, 2014.

[73] R.-L. Lin, C.-C. Lee and Y.-C. Chang, "Optimal design of LED array for single-loop CCM buck-boost LED driver," IEEE Industry Applications Society Annual Meeting, pp. 1-5, 2011.

[74] J. Zhang, H. Zeng and T. Jiang, "A primary-side control scheme for high-power-factor LED driver with TRIAC dimming capability," IEEE Transactions on Power Electronics, vol. 27, no. 11, pp. 4619-4629, vol. 27, no. 11, pp. 4619-4629, 2012.

[75] M. Arias, A. Vázquez and J. Sebastián, "An overview of the AC-DC and DC-DC converters for LED lighting applications," automatika, vol. 53, pp. 156-172, 2012.

[76] Lumileds, "DS061 LUXEON Rebel ES Product Datasheet," 2016.

[77] Schneider Electric, "Adjustable frequency controllers," SC100 R5/95, 1995.

[78] J. Pedra, L. Sainz and F. Corcoles, "Study of aggregate models for squirrel-cage induction motors," IEEE Transactions on Power Systems, vol. 20, no. 3, pp. 1519-1527, 2005.

[79] G. S. Buja and M. P. Kazmierkowski, "Direct torque control of PWM inverter-fed AC motors - a survey," IEEE Transactions on Industrial Electronics, vol. 51, no. 4, pp. 744-757, 2004.

[80] A. Trzynadlowski, The field orientation principle in control of induction motors, Boston: Kluwer academic publishers, 1994.

[81] P. Vas, Sensorless vector and direct torque control, Oxford University Press, 1998.

[82] MathWorks, "Simulink," MathWorks, [Online]. Available: http://www.mathworks.com.

[83] A. Bokhari et al, "Experimental determination of the ZIP coefficients for modern residential commercial, and industrial loads," IEEE Transactions on Power Delivery, vol. 29, no. 3, pp. 1372-1381, 2014.

[84] V. Knyazkin, C. A. Canizares and L. H. Soder, "On the parameter estimation and modeling of aggregate power system loads," IEEE Transactions on Power Systems, vol. 19, no. 2, pp. 1023-1031, May 2004.

[85] A. Capasso, W. Grattieri, R. Lamedica and A. Prudenzi, "A bottom-up approach to residential load modeling," IEEE Transactions on Power Systems, vol. 9, no. 2, pp. 957-964, 1994.

[86] L. Chuan and A. Ukil, "Modeling and validation of electrical load profiling in residential buildings in Singapore," IEEE Transactions on Power Systems, vol. 30, no. 5, pp. 2800-2809, 2015.

[87] F. Tremblay, "Modelisation de la charge, calcul du Np en temps reel," Hydro-Quebec, 2003.

[88] J. A. Fuentes, A. Gabaldón, A. Molina and E. Gómez, "Development and assessment of a load decomposition method applied at the distribution level," IEE Proceedings-Generation, Transmission and Distribution, vol. 150, no. 2, pp. 245-251, 2003.

[89] IEEE Std. 399, "IEEE recommended practice for industrial and commercial power systems analysis," 1997.

[90] A. Bonner, T. Grebe, E. Gunther, L. Hopkins, M. Marz, J. Mahseredjian and e. al., "Modeling and simulation of the propagation of harmonics in electric power networks. 1. Concepts, models, and simulation techniques," IEEE Transactions on Power Delivery, vol. 11, pp. 452-465, 1996.

[91] EPRI, "Load shape library," EPRI, [Online]. Available: https://loadshape.epri.com.

[92] NERC TPL-001-4, "Transmission system planning performance requirements," NERC, [Online]. Availbale: https://www.nerc.com/files/TPL-001-4.pdf.

[93] K. Yamashita, S. M. Villanueva and J. V. Milanović, "Initial results of international survey on industrial practice on power system load modelling conducted by CIGRE WG C4. 605," CIGRE 2011 Bologna symposium-The Electric Power System of the Future: Integrating Supergrids and Microgrids, 2011.

[94] R. Dugan, Electrical power systems quality, New York: McGraw-Hill, 1996.

[95] Google, "Google Earth," Google, [Online]. Available: https://www.google.com/earth.

[96] CYME, "CYMDIST," CYME, [Online]. Available: http://www.cyme.com/software.

[97] S. Ranade and W. Xu, "An overview of harmonics modeling and simulation," in Tutorial on Harmonics Modeling and Simulation, IEEE Power Eng. Soc., 1998, pp. 1-7.

[98] I. Kocar and J. Mahseredjian, "Accurate frequency dependent cable model for electromagnetic transients," IEEE Transactions on Power Delivery, 2015.

[99] F. Bu, Z. Ma, Y. Yuan and Z. Wang, "WECC composite load model parameter identification using evolutionary deep reinforcement learning," IEEE Transactions on Smart Grid, vol. 11, no. 6, pp. 5407-5417, 2020.

[100] X. Wang, Y. Wang, D. Shi, J. Wang and Z. Wang, "Two-Stage WECC composite load modeling: a double deep Q-learning networks approach," IEEE Transactions on Smart Grid, vol. 11, no. 5, pp. 4331-4344, 2020.